Politecnico di Torino

ScuDo
Scuola di Dottorato ~ Doctoral School
WHAT YOU ARE, TAKES YOU FAR

Doctoral Dissertation
Doctoral Program in Energy Engineering (35^{th}cycle)

Modelling and characterisation of microrings for semiconductor lasers integrated in the Silicon Photonics platform

By

Marco Novarese

******

Supervisor(s):
Prof. Mariangela Gioannini

Doctoral Examination Committee:
Dr. Carlos Alonso-Ramos, Université Paris Saclay
Dr. Cosimo Lacava, Università di Pavia
Prof. Francesco Morichetti, Politecnico di Milano
Prof. Giovanni Ghione, Politecnico di Torino
Prof. Marc Sorel, TeCIP Institute, Scuola Sant'Anna di Pisa

Politecnico di Torino
2023

Declaration

I hereby declare that, the contents and organization of this dissertation constitute my own original work and does not compromise in any way the rights of third parties, including those relating to the security of personal data.

Marco Novarese
2023

* This dissertation is presented in partial fulfillment of the requirements for **Ph.D. degree** in the Graduate School of Politecnico di Torino (ScuDo).

I would like to dedicate this thesis to all those who supported me with special care
for my loving parents and Francesca.

Acknowledgements

I am extremely thankful to my supervisor Prof. Mariangela Gioannini for giving me the possibility of working on this project and her invaluable patience and feedback.

Additionally, this work would not have been possible without the strong collaboration with CISCO Systems (San Jose, CA) and CISCO Optical (Nuremberg, Germany) that made possible to obtain some of the results presented in this thesis. In particular, I thank CISCO researchers Dr. Jock Bovington, Dr. Sebastian Romero Garcia, Dr. Don Adams and Dr. Fabrizio Forghieri, for the fruitful discussions and collaboration we had during this PhD work.

I am also grateful to my colleagues Dr. Giannuzzi Giuseppe, Stefania Cucco and Dr. Cristina Rimoldi for their help and feedback sessions.

Thanks should also go to the people working in LINKS at PhotoNext, namely Dr. Antonino Nespola, Dr.Stefano Straullu, Francesco Aquilino and Dr. Massimo Olivero who helped me in developing the experimental bench.

Similarly I thank Prof. Hui Rongqing (University of Kansas) who helped me in the setup for Pump and Probe experiment and Prof. Paolo Bardella (Politecnico di Torino) who designed some of the Silicon Photonics chips characterised in the laboratory.

Lastly I would like to thank my defence committee, who generously provided knowledge and expertise that made it possible to improve this thesis.

Abstract

The aim of this PhD thesis is to develop tools for understanding and describing the behaviour of silicon in the context of hybrid tunable lasers developed in the Silicon Photonics platform. These lasers incorporate a III-V Reflective Semiconductor Optical Amplifier (RSOA) as an active component coupled with a passive mirror made of ring resonators, which act as filters and determine the laser's output frequency.
However, when propagating in the silicon ring waveguide, the optical field experiences significant absorption due to non-linear (NL) effects such as Two Photon Absorption (TPA) and Free Carrier Absorption (FCA). These effects result in the accumulation of free carriers within the silicon core waveguide, which can adversely affect the performance of the ring resonators, even with input powers of just a few milliwatts. This thesis has two primary objectives: first to develop a compact model that describes the impact of NL effects on the performance of ring resonators; second to establish an experimental setup designed for the characterization of microrings resonators in steady-state regime (as in the case of the hybrid tunable laser) or in switching applications where a good knowledge on the ring response in time is crucial.
Within this framework, I have numerically solved the non-linear problem associated with the variation of silicon refractive index and optical losses coupled with the Shockley-Read-Hall recombination (SRH) theory for trap-assisted recombination processes of free carriers.
Furthermore, the developed theory has been effectively generalised to incorporate more complex waveguide cross sections, such as rib waveguides. This extension allows for a comprehensive description of the diffusion of free carriers in silicon, resulting in an non-uniform distribution within the ring core cross section. In contrast, strip waveguides maintain a uniform distribution of free carriers throughout the silicon core.
To validate our approach, I have developed a flexible experimental setup that supports

the characterization of various types of ring resonators using continuous input power and pump-probe experiments.
In the pump-probe experiment, high power pulsed input light is introduced into the ring to analyse the impact of free carriers on the ring's response and extract the free carrier lifetimes in ring resonators. The experimental results are found to be in good agreement with the developed theory.
Finally, I conclude this work by introducing the theoretical formalism that extend our model beyond the simple ring resonator to incorporate the description of the hybrid tunable laser composed of the RSOA and the passive mirror with non-linear silicon microrings.

Publications

Papers in peer-reviewed journals

- Marco Novarese, Sebastian Romero Garcia, Stefania Cucco, Don Adams, Jock Bovington, and Mariangela Gioannini, "Study of nonlinear effects and self-heating in a silicon microring resonator including a Shockley-Read-Hall model for carrier recombination," *Opt. Express* 30, 14341-14357 (2022).
- Marco Novarese, Sebastian Romero Garcia, Jock Bovington and Mariangela Gioannini, "Dynamics of Free Carrier Absorption and Refractive Index Dispersion in Si and Si/PolySi Microrings," in *IEEE Photonics Technology Letters*, vol. 35, no. 8, pp. 450-453, 15 April 15, 2023.

Conference proceedings

- Mariangela Gioannini, Lorenzo Columbo, Antonino Bologna, Marco Novarese, Sebastian Romero Garcia, Dominic Siriani, Jock Bovington, "Design of hybrid lasers for silicon photonics: efficiency, optical feedback tolerance and laser dynamics" *European Conference on Integrated Optics ECIO*, Paris, France, 22 June, 2020.
- Marco Novarese, Sebastian Romero Garcia, Don Adams, Jock Bovington, Mariangela Gioannini, "Study of nonlinear effects and self-heating in silicon microring resonator including SRH model for carrier recombination," *Proc. SPIE* 12006, Silicon Photonics XVII, 120060G (5 March 2022).
- Marco Novarese, Stefania Cucco, Sebastian Romero Garcia, Jock Bovington, Rongqing Hui, Mariangela Gioannini, "Static and Dynamic Nonlinear Effects in Silicon Micro-Rings: Impact of Trap Assisted Shockley Read Hall Carrier Recombination", *European conference on integrated optics 23rd* Milan, 4-6 May 2022.
- Marco Novarese, Sebastian Romero Garcia, Jock Bovington, Mariangela Gioannini, "Measurements and modelling of free carrier lifetimes in Si and Si/poly-Si microrings", *IEEE Silicon Photonics Conference (SiPhotonics)* Arlington VA, 4-7 April 2023.

Contents

Chapter 1

Introduction

1.1 Silicon photonics: a key enabling technology for optical interconnects

Silicon photonics capabilities

Silicon photonics (SiPh)is an emerging technology that combines the advantages of photonics and electronics on a silicon substrate. The field is rapidly growing and enabling the development of highly integrated and scalable photonic integrated circuits (PICs) for optical communication, sensing, and computation [1–3]. One of the primary advantages of SiPh is the possibility of integrating in a compact chip transmitters and receivers, making it ideal for high-speed data transfer applications as in data centers and high-performance computing [4]. Compared to traditional copper wiring, this technology can also reduce power consumption while transmitting data over long distances [5]; it guarantees immunity to electronic interference thanks to the use of optical signals [6, 7], which is an important consideration for energy-efficient computing and data transmission. Integrated silicon photonics circuits can also combine multiple optical functions on a single chip, allowing for more compact devices with increased functionality. On top of that, SiPh based technologies are scalable and can be manufactured using existing semiconductor fabrication processes, making it a cost-effective solution for high-speed data transmission.
One essential building block for silicon photonic systems is the standard multi-project wafer (MPW) flow in the Silicon-on insulator (SOI) platform, which allows

for the simultaneous implementation of multiple functions on a single wafer. Figure 1.1 shows a cross-sectional view of a standard MPW components such as optical waveguides, phase shifters, photodetectors, grating couplers, and modulators. These components are fundamental in enabling the efficient and reliable transfer and manipulation of optical signals [3].

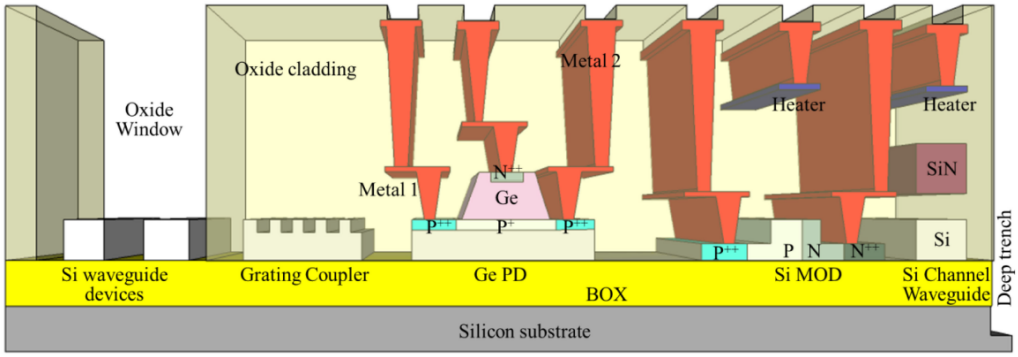

Fig. 1.1 Fundamental building blocks for silicon photonic devices: cross-sectional view of a standard MPW flow displaying common components including phase shifters, photodetectors, grating couplers, and modulators. Image reproduced from [3].

These advantages make silicon photonic PICs ideal for high-speed and high-bandwidth applications, such as in data centers, telecommunications, and high-performance computing. In addition to these applications, silicon photonic PICs can also be used for sensing purposes, such as environmental monitoring and biomedical sensing. For instance, silicon photonic-based sensors have shown high sensitivity and selectivity in detecting biomolecules [8]. In this introduction we first give an overview on silicon photonics application; then we will introduce the main SiPh components. We will conclude by discussing tunable lasers integrated in SiPh platform and optical micro-rings that are the focus of this thesis.

Silicon photonics for optical interconnects

A key property of silicon photonics technology is that it enables data transmission over different distances, namely long-distance, short-distance, and inter-chip communication [3].
Long-distance communication is typically facilitated by optical fibers, which transmit data over hundreds of kilometers between different locations, such as between

buildings, data centers, or across countries. Here optical transceivers serve the critical function of converting electrical signals to optical signals and vice versa, enabling the transmission of data over optical fibers. This technology is vital to the efficient communication in data centers, where high-speed communication is essential for processing and transmitting vast amounts of data [9]. This significantly reduces the cost and space requirements in data center facilities while improving their overall efficiency and performance. Conventional optical transceivers usually consist of separate modules that house optoelectronic components (e.g. lasers, photodetectors, and photodetectors), and electronic components (e.g. drivers and amplifiers). In response to the growing demand for smaller and more power-efficient solutions, co-packaged optical transceivers have emerged as a new technology [10], integrating both the optoelectronic and electronic components into a single module. Co-packaged optical transceivers are also potentially lower-cost than traditional transceivers, as the integration of the components can reduce the number of interconnects and interfaces required. They also present higher bandwidth and lower latency [11], which can be beneficial in applications such as data center interconnects.

Dense Wavelength Division Multiplexing (DWDM) and Coarse Wavelength Division Multiplexing (CWDM) [2] networks represent the two most important methods to transmit data in long and short reach application based on silicon photonics. These technologies are used in optical communication networks to increase the capacity of fiber-optic cables by combining multiple optical signals of different wavelengths (colors) onto a single fiber-optic cable, allowing for more data to be transmitted simultaneously [12]. DWDM is mostly used for C and L band applications and is able to reach a minimum spacing between wavelengths of $0.8\,nm$. Whereas CWDM can span from the O to the L band with a minimum spacing of $20\,nm$. This property can be achieved by converting multiple channels of data streams through thermal tuning of microring modulator that modulates an external laser source into optical signals at specific wavelengths through electro-optic modulation. The modulated optical signals are then sent across optical fibers to a receiver side position, where photodiodes at the drop port of microring filters extract the optical signals at specific wavelengths converting the optical signals back to the electrical data streams [13]. The choice of one technology with respect to the other depends on the field of application: for example in the optical transceiver $DWDM-100G-Q28-120$ by Edgeoptic uses DWDM and microring to filters to modulate the light generated by a distributed feedback laser (DFB) making it possible to convert $425.78\,Gb/s$

electrical signals to a single $100\,Gb/s$ optical signal over a maximum distance of $120\,km$. Similarly the $SPTSHP3PMCDF$ optical transceiver by Intel can reach a total of $400\,Gb/s$ with DWDM techonology and photodetectors (PD) integrated on the same SiPh chip.

In contrast to long-haul or metro applications, the requirements for silicon photonics modules in short distance data center communications (e.g. in intra data centers or rack-to-rack) focus more on cost-effectiveness, high-volume production, energy efficiency, and frequency upgradability [3, 14]. Small Form-factor Pluggable (SFP) transceivers are optical transceivers that can utilize both CWDM and DWDM technology and are extensively employed for short-reach optical communication applications due to their much cheaper cost when compared to long-haul counterparts since the coherence of the laser beam must be ensured for distances lower than $1\,km$. The table in figure 1.2 shows some of the commercially available optical transceivers for long and short reach.

Type	Device	Data rate, Gb/s	Distance	Power, W	Price, $	Vendor	SiPh function
Long	SPTSHP3PMCDF	8x50	2 km	12	2100	Intel	DWDM,PD
	DWDM-100G-Q28-120	4x25	120 km	<5.5	2800	Edgeoptic	DWDM,PD
	100GCWDM4 QSFP28	10	80 km	<1.5	389	Cisco	CWDM,PD
Short	100G-QSFP28-2.1	4x25	500 m	<3.5	133	Edgeoptic	CWDM,PD
	QBP13P50E0PF	8x50	500 m	<10	585	Fiber mail	CWDM,PD

Fig. 1.2 Performances comparison of long and short reach silicon photonics based optical transceivers.

These devices are compared not only in terms of data rate, but also considering the overall distance and power consumption. High data rata for a long communication distance always results in higher costs needed for a error-free information propagation, which also explains the low price of the $100GCWDM4QSFP28$ that can reach up to $80\,km$ of maximum distance but with a lower data rate using CWDM technology. Therefore in short reach communication optical transceivers present lower costs when compared to similar data-rate long haul device even with the same technology.
Optical communications in data centres and rack-to-rack are performed through single mode (SM) or multimode optical fibers. We remark that single-mode fibers are the preferred choice for optical communication in both intra-data center and long-haul silicon photonics due to their superior performance when compared to

multi-mode fibers. This is attributed to their smaller core diameter, which enables better control over light propagation, resulting in lower loss, reduced modal dispersion, and higher bandwidth. Moreover, single-mode fibers are more compatible with silicon photonic devices that have small waveguide dimensions that match the mode size of single-mode fibers via the usage of spot size converter (SSC) (SSC).

Finally, communication between electrical components can be established using

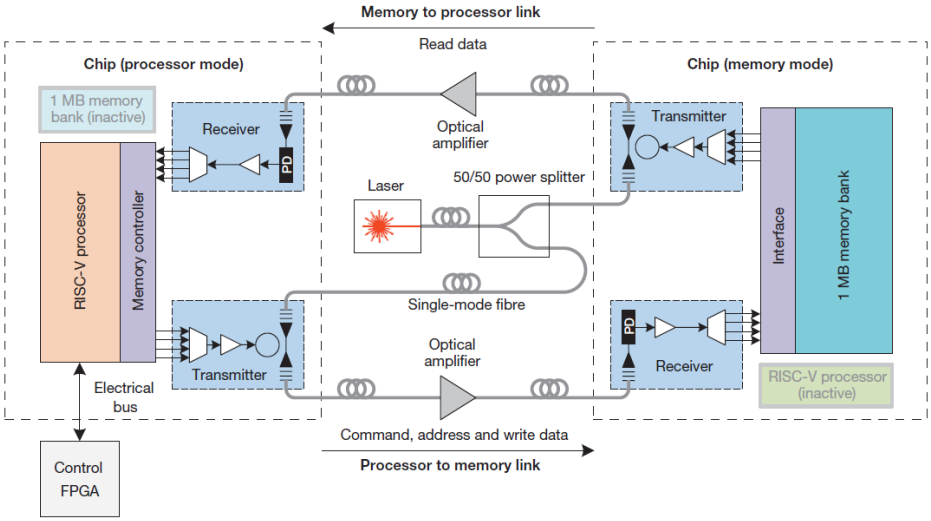

Fig. 1.3 Block diagram of communication between different chips through optical interconnects. The system uses one chip acting as the processor and the other acting as memory, connected by an optical link. Each chip is an electro-optic system integrating electronics and optical components such as waveguides, photodetector and microring resonators which have the role of transmitting and receiving data from one chip to another. Image reproduced from [15].

integrated optical circuits, which merge photonic devices with electronic circuits also enabling data transmission between chips [15–17]. This approach is particularly beneficial in high-performance computing, where rapid and efficient communication between different components is essential for optimal performance. As shown in figure 1.3, optical interconnects (single-mode fibers) can be employed to transmit data between two different chips for memory applications [15]. Light is coupled into the two chips by vertical grating couplers and converted back to electrical signal by photodetectors, whereas the sender data is encoded by microring modulators all integrated on the same chip. An off-chip solid-state laser acts as the light source to the chips.

Optics links drastically reduce the power consumption associated to metal wires for

data transfer [18], while maintaining a good compatibility with CMOS processes [19] thanks to the silicon based technology.

Other silicon photonics applications

SiPh find applications in a wide range of areas. For example SiPh based Light detection and ranging (LIDAR) [20] is based on the concept of measuring distance and reconstruct objects in 3D space. To this aim two main methods are usually pursued: the time of flight (ToF) and frequency-modulated continuous-wave (FMCW) techniques. In the first case a short laser pulse is sent towards a target and the time lapse between the outgoing light pulse and the detection of the reflected (back-scattered) is recorded; whereas in FMCW a laser source transmits a frequency-modulated optical wave, which is reflected by a target surface. The beat frequency on the receiver pin SiPh Photodetector encodes the distance to the target. Integrated optical phased arrays (OPA) are one of the most important component in LIDAR application since they can provide high coherence output power with a reasonable low cost [21]. OPA consist of several coherent waveguides thermally controlled so that, by aligning the phase of the propagating field in each of them, the emitted light interferes constructively in the far field at certain angles as shown in figure 1.4. Light can be

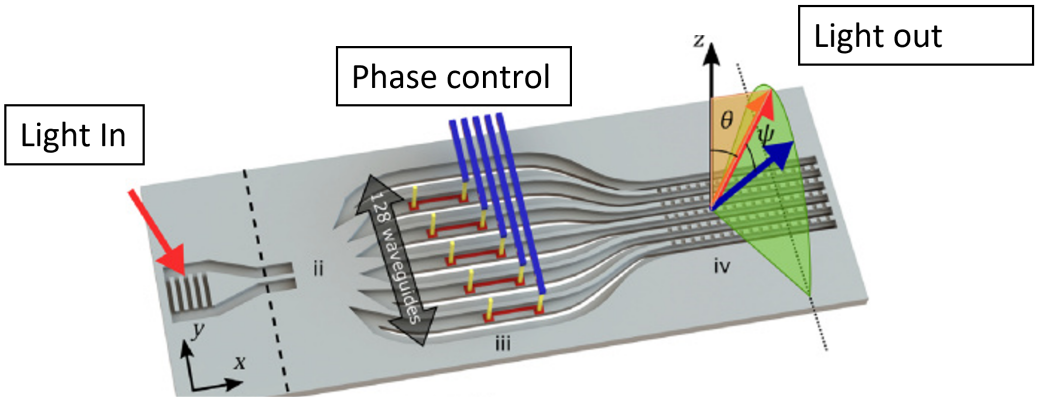

Fig. 1.4 Schematic of a silicon photonics chip for LIDAR applications based on the concept of phase control of optical waveguides for generation of high coherence optical light. Image reproduced from [22].

generated externally and coupled into the system with grating couplers or through edge coupling. To this scope widely tunable hybrid laser integrated on the same chip have been demonstrated as an alternative to large and expensive external light

sources [23]. For example in [24], a low power high speed sensor has been reported for autonomous driving applications. Here the authors propose an heterogeneously III-V semiconductor optical amplifier (SOA) integrated in a SiPh chip for Lidar with a very small device footprint of only $4.5\,mm^2$.
Neuromorphic photonics represents another emerging field that could bring improvements in both speed and energy efficiency over common digital electronics thanks to the high connectivity and linear operation provided by tunable waveguide elements and WDM technology [25]. In fact metal wire connections pose huge limitations in non-trivial distributed information processing in Neural networks, since large distances are usually required leading to non-neglibile optical losses and heat generation. Optical interconnections do not suffer from frequency distortion effects related to skin effect (higher carrier density closer to the surface of the wire) caused by AC current. For the same reasons programmable photonic circuits [26] have seen the light recently as a promising field made possible by SiPh.

1.2 Building blocks of silicon photonics ICs

Integrated photonics circuits consist of a variety of optical components incorporated on a single chip, with either monolithic (grown directly on silicon) or heterogeneous integration (molecular or ahdesive bonding of epitaxial layers of unpatterned III-V dies or wafers to a pre-processed silicon on insulator wafer), dependent on the materials selection. In this section we give a general list of frequently implemented building blocks in PIC and a brief overview of their possible applications.

- **Waveguides**: silicon waveguides can have a simple rectangular geometry (strip) or more complex structures such as in the rib waveguide, mostly used in modulators where it is possible to insert doping regions outside the guiding core. The optimisation of silicon waveguide geometry is fundamental to reduce as much as possible nonlinear (NL) effects; for examples the implantation of defects in rib waveguides has been shown to drastically reduce the free carrier lifetimes [27] that can cause high free carrier absorption in silicon. The propagation loss α_0 in a waveguide determines the amount of losses in dB/cm that the confined mode undergoes during propagation; while it is usually negligible in Si_3N_4, for silicon it depends on the fabrication method

with values as small as $0.1\,dB/cm$ [28] to $1-3\,dB/cm$ that we measured for the devices tested in this thesis.

- **Grating/Edge couplers**:Surface grating couplers (SGCs) [29, 30] and Edge couplers [31] represent the two main approaches to couple light to or from integrated PICs [32]. SGCs are formed by a periodic diffraction grating often connected to a waveguide which brings the light in the SiPh chip. This type of coupling is said to be vertical since light is sent to the grating couplers by a tilted optical fiber positioned above the device. On the contrary edge coupling is performed on the same plane of the PIC.

- **Mach Zehnder Interferometers**: Mach-Zehnder Interferometer (MZI) are the most important component in optical modulators [33–35]. The input beam is divided into two arms respectively. The phase difference between the two beams produces constructive or destructive interference in the output port associated with an intensity and phase modulation [36]. This phase difference is achieved by optical phase shifters that are based on plasma dispersion or thermal effect. In the first case an electrical signal applied to electrodes causes changes in refractive index and absorption of the material [37] (plasma dispersion effect associated with the electro-refraction and absortpion relations [38]) [39, 38], whereas in thermo-optic phase shifters the material refractive index is changed by thermal tuning [40]. The latter is particular efficient in silicon due to its high thermo-optic coefficient $\frac{dn_{Si}}{dT} = 1.86 \cdot 10^{-4}\,K^{-1}$ [41, 42]. However, due to thermal dissipation limiting the performance of the device, thermally controlled MZI are very slow compared to plasma dispersion devices.

- **Microring resonators** A microring resonator (MRR) is a resonant cavity which is the result of a looped waveguide where light can circulate either clockwise or counterclockwise. They find applications in several SiPh PICs where they can be used in the design of hybrid tunable lasers [43, 44]. In MRR, the optical power is generated through constructive interference at certain wavelengths called resonant wavelengths which makes it possible to have hundred of mW of circulating power for just some mW of input power. By stacking several MRRs it is therefore possible to build reliable and compact tunable filters [45].
  Thanks to their versatility, MRRs can also be used as modulators (micro-ring

modulator MRM) where, by modulating the effective refractive index of the ring, the transmission can be tuned towards or away from resonance. Silicon microrings with lateral pn junctions waveguides have been demonstrated as high speed modulators compatible with PAM4 modulation [46, 47]. Further modulation speed can be reached by using vertical junctions, such as the silicon-insulator-silicon capacitor platform (SISCAP) junctions [48], with the concept of having a larger depletion region at the cost of higher fabrication complexity [3].

- **Photodetectors** Photodetectors are semiconductor devices that convert optical signals into electrical signals. This conversion is achieved by the absorption of photons with energy equal or greater than the material bandgap resulting in the formation of an electron-hole pair. The pin structure made of an intrinsic region in between of p-type and n-type type regions is the most common structure, figure 1.5. Here the transit time of photogenerated carriers is kept low

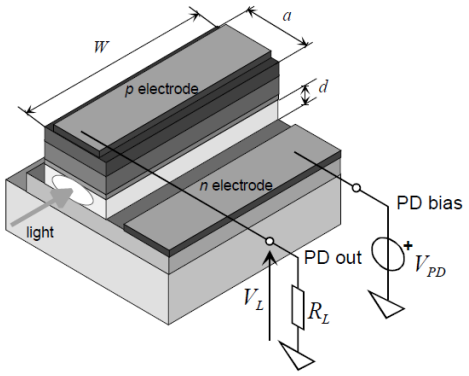

Fig. 1.5 Schematic of a waveguide pin photodiode.

thanks to the small waveguide thickness d. By applying an external reverse bias, a depleted area is created resulting in an high electric field that makes it possible to collect the photogenerated carriers quantifying the amount of optical power entering the device.
Germaniun is often used as the intrinsic material due to its high absorption in the near infra-red and compatibility with CMOS deposition processes [49, 50]. These devices are characterised in terms of responsivity R_{Pd}, dark current I_{dark}, and detection bandwidth BW. R_{Pd} is the ratio between the generated photocurrent and the incident optical power, while the dark current is the total current collected when the junction is reverse bias and with no illumination. Long

waveguides (parameter W) makes it possible to have a better responsivity but at the cost of a larger capacitance and therefore lower bandwidth of the photodiode.
Very small dark current around $2\,nA$ with $R_{Pd} \approx 0.65\,A/W$ have been demonstrated in [51] with a bandwidth as large as $40\,GHZ$. Higher values of responsivity $R_{Pd} > 1\,A/W$ with $I_{dark} \approx 8\,ns$ have been reached in [52] which results in a lower bandwith, namely $BW = 27\,GHz$.

The previously introduced fundamental blocks are used for the realisation of complex devices such as optical transceivers and hybrid tunable lasers. The silicon nitride-on-insulator (SiN) platform [53] is an alternative to classic SOI-based devices due to the very low propagation losses in Si_3N_4 when compared to silicon. Silicon nitride is CMOS-compatible, and typically deposited by Low Pressure Chemical Vapour Deposition (LPCVD) or by Plasma Enhanced Chemical Vapour Deposition (PECVD). Since the refractive index contrast between the Si_3N_4 core and the cladding is approximately equivalent to 0.55, scattering losses are reduced when compared to Silicon [54], at the cost of a lower field confinement inside the core which ultimately leads to a larger footprint of SiN based devices. The latter is crucial for silicon nitride MRRs where the bend radius must be maintained above $95\,\mu m$ to avoid too large bend losses caused by the aforementioned poor field confinement in the core. However Si_3N_4 thermo-optic coefficient is one order of magnitude lower than in silicon, resulting in a worst thermal control of the material. Table 1.1 summarizes the differences between the SiN and SOI performances. The main drawback of

Table 1.1 Comparison between SiN and SOI platforms.

	Platform		
Parameter	SiN	SOI	Unit
Refractive index contrast (C-band)	≈ 0.55	2.06	–
Typical α_0	< 0.01	$1-3$	dB/cm
Thermo-optic coefficient	$2.51 \cdot 10^{-5}$	$1.87 \cdot 10^{-4}$	$1/K$
Minimum bend radius	≈ 95	≈ 5	μm

using silicon as optical medium is that extra losses are introduced due to power dependent non-linear effects [41, 55–58]. This is especially relevant in MRRs where the circulating power in the ring can reach hundred of milliwatts for input power as small as $4\,mW$ [58], causing a wavelength shift and distortion of the ring spectral response.

TPA and FCA are the main mechanism responsible for such behaviour [59, 60], leading to free carriers generation that affects the effective refractive index of the material through free-carrier dispersion (FCD) and self-heating.
since silicon nitride has a wide band gap, SiN-waveguides and MRRs do not suffer from TPA and FCA, making it possible to have high Q-MRRs employed in high power narrow linewidth hybrid tunable laser [61, 62]. It is clear that the choice of one platform in relation to another depends largely on the application. Since the goal of this thesis is to model and characterise silicon MRRs to be used in compact and small hybrid tunable laser, the SOI platform is the most appropriate choice for this purpose.

1.3 Hybrid tunable lasers

An hybrid tunable laser is one of the most important component in an optical transceiver, since its role is to generate a stable and narrow linewidth optical CW signal that can be modulated by external modulator. Moreover wide-range wavelength tuning and narrow linewidth tunable lasers are the main components of digital coherence technologies and WDM where high coherence in the bit transmission must be ensured [63] while providing good tunability and compact size impossible to reach with common laser sources [64].
Silicon-only laser sources do not currently exist since silicon in an indirect band gap material, as a result several technological solutions for efficient light source integration on silicon photonic platforms have been adopted [65]; these include hybrid integration [43, 61, 66–68], heterogeneous bonding [69, 70], and epitaxial growth of III-V material on silicon substrate [35]. Hybrid or heterogeneous integration are widely employed for tunable lasers; hybrid tunable lasers have reached the same performances of commercially available lasers [17, 43, 44]. Moreover hybrid tunable lasers can also exhibit high tolerances to external feedback when compared to common semiconductor laser emitting at the same power and with the same wall-plug efficiency (WPE) [66] (WPE is the conversion efficiency of electric power into optical power). Table 1.2 collects different SiPh tunable laser as reported in the literature, these are compared in terms of tuning range, maximum output power from the laser, laser linewidth, and side-mode-suppression-ratio (SMSR) as

defined in Appendix B. The type of integration method of the active part with the passive mirror is also reported.

Table 1.2 Comparison of tunable semiconductor lasers on different platform and integrations methods.

Mirror Comp.	Integration Method	Tuning range, nm	$P_{max,out}, mW$	Linewidth, kHz	SMSR, dB	Ref.
Double Si MRRs+loop reflector	Hybrid	65	100*	< 15	> 45	[71]
Double Si MRRs+loop reflector	Hybrid	65	150*	40	50	[72]
Double Si MRRs+ a-MZI	Hybrid	99	35	–	–	[73]
Double Si_3N_4 MRRs+Sagnac loop	Hybrid	172	26.7	0.75	> 40	[23]
Triple Si MRRs	Heterogeneus	118	< 15	< 0.095	> 50	[74]
Four Si MRRs	Heterogeneus	120	2	0.14	> 16	[75]
Double Si MRRs	Monolitch	16	2.7	–	> 45	[76]

*An integrated booster SOA is used to amplify the output power outside the laser cavity.

We report also of a case of monolitich integration [76] where the active medium, a tunable quantum dot layer, has been grown directly on the silicon substrate. Although in this case the laser properties are not as good as those of hybrid and heterogeneous integration, monolithic integration has the great advantage of bringing low-cost and mass production capabilities thanks to single-step epitaxy process for material deposition on silicon.
We also highlight that the Si_3N_4 platform can reach very large tuning range and output power without the need of any external booster as in [71] and [73] thanks to the absence of NL effects litiming silicon based MRRs. However Si_3N_4 MRRs present large ring radii of approximately $117\,\mu m$ leading to a much larger footprint area than for example in [73].
This thesis inserts in a project focused on the modeling and design of widely tunable lasers that will be fabricated by a company. The laser is realised via the edge coupling of a commercial reflective semiconductor optical amplifier (RSOA) representing the III-V gain material and a SiPh passive mirror made of silicon or SiN waveguides as shown in figure 1.6.

In this project it has been proposed a first design in [66] where the SiN platform was used, whereas I contributed in [77] to the set-up of some preliminary considerations for the implementation of Si MRRs. The basic working principle is the same in both cases: the light, generated by the RSOA, is focused into the passive photonic mirror after the anti-reflection coating (AR) (AR). The mirror is composed of a spot size converter, phase control section (PS), a splitter, and two add-drop ring resonators. The SSC role is to optimize the coupling of light from the RSOA to the input waveguide of the passive mirror; the phase control section is needed in order to tune the laser longitudinal modes to the maximum of the effective reflectivity

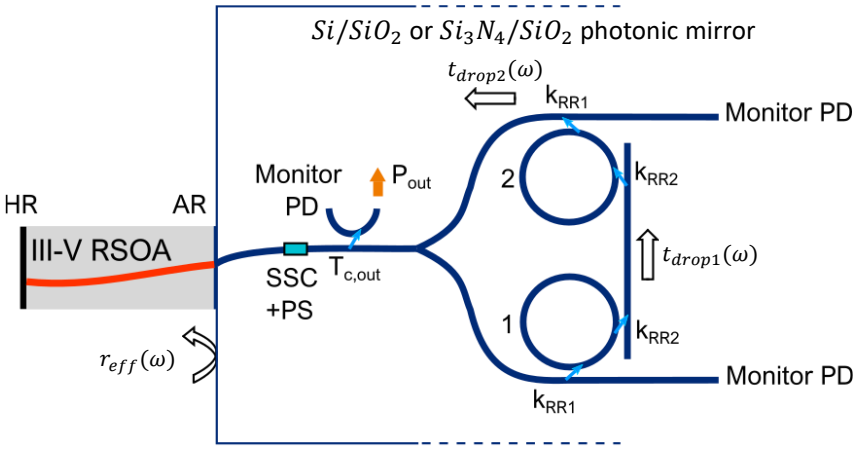

Fig. 1.6 Schematic of the hybrid tunable laser analysed in [66, 77]. The III-V reflective SOA (RSOA) provides the light that is focused on the photonic mirror by a spot size converter ; here the the output power is collected at the output of the coupler. The tunable laser output wavelength is selected by means of the Vernier effect thanks to the thermal tuning of two similar ring resonators.

.

of the photonic mirror indicated with $r_{eff}(\omega)$. The laser tunability is achieved by the dual-ring Vernier filter [43, 78], i.e., the alignment of the resonant frequencies of two similar ring resonators obtained in our case by thermal tuning. Lastly, the tunable laser output is taken at the output coupler instead of the right end of the passive mirror [70] allowing light to travel within the entire structure only once, thereby reducing the total round-trip loss [43, 61, 66]. Monitor photodetectors are included for calibration. In my thesis I focused on the characterisation of silicon MRRs in linear and nonlinear regime with the aim of developing a model and a general understanding of the rings characteristics to be employed in mirrors for tunable lasers.

1.4 Silicon microring resonators

It is evident that ring resonators play a fundamental role in hybrid tunable lasers [66, 79] and SiPh modulators. SOI MRRs have a small footprint of less than a hundred microns [17, 80]. In addition, due to the storage properties of optical resonators and possibility to reach large quality factors ($Q > 10^6$ [6]), MMRs are also considered as efficient filters [81] and high resolution sensors [82, 83].
Today, MMRs are mainly realised on the SOI and SiN platforms due to their low

cost integration with CMOS processes [17, 18, 65]. Compared to silicon nitride, the use of silicon device layers for the manufacture of components such as optical waveguides and ring resonators ensures a stronger field confinement in the silicon core, and a superior miniaturization associated with a reduction of bend losses that results in very small ring resonators [84]. In fact, crystalline silicon c-Si ring radius can be as low as $r \approx 5\mu m$ with negligible bend loss.

In addition, the larger thermo-optic coefficient in silicon with respect to silicon nitride [85, 86] makes silicon MRRs the preferred choice when a wide thermal tuning of the ring resonant wavelength is required [67, 43, 69, 81]. Silicon non-linearities are detrimental in applications where rings are utilized as narrow band mirrors, as for example in high power hybrid tunable lasers [43, 44, 87]. For these applications, the ring spectral response must be as close as possible to the linear regime; as a result NL effects pose a limit to the maximum power that the tunable laser can generate. An important figure of merit (FOM) regulating the impact of NL effects is the free carrier lifetime: a smaller lifetime implies faster recombination of free carriers, whose reduction is then associated with a lower propagation loss within the cavity. At the same time self-heating is regulated by the ability of the ring to dissipated heat, i.e., the thermal impedance Z_T. A small thermal impedance means rapid thermal dissipation which is required to limit the red wavelength shift of the resonance when self-heating becomes dominant [58, 88].
Table 1.3 collects several examples of MRRs and related applications available in the literature. We note how Si_3N_4 ring for tunable lasers such as in [23] can reach very high quality factors since they are not affected by TPA and FCA at the cost of a very large ring length as explained before.

Table 1.3 Comparison of different MRRs with silicon,Si_3N_4, amorphous silicon (a-si), and polysilicon.

Ring structure	Application	Length, μm	Quality factor	FSR, nm	Ref.
Add-Drop Si MRR	Tunable laser	73	5166	7	[73]
Add-Drop Si MRR	Tunable laser	3800	537630	0.18	[74]
All pass Si MRR	Wavelength conversion	62	23000	8	[89]
All pass Si MRR	Polarization Analyzer	31.4	3000	20	[90]
Add-Drop Si MRR	Optical memory cell	803	1000	–	[91]
All pass Si MRR	100Gb/s PAM4 modulation	75	3550	5.7	[92]
Add-Drop Si_3N_4 MRR	Tunable laser	4553	$6.6 \cdot 10^4$	1.5	[23]
Add-Drop a-Si MRR	25 ps Optical switch $\alpha_0 > 50 dB/cm$	31.4	1300	–	[93]
Polysilicon MRR	135 ps Optical switch $\alpha_0 \approx 10 dB/cm$	251	11200	–	[94]

Amorphous silicon and polysilicon are mainly used in optical switches thanks to the very short free carrier lifetimes achieved by defects and grains, respectively. The main disadvantage of using a-Si lies in the very high propagations losses α_0 due to scattering, polysilicon can partially mitigate this issue with lower losses and still present free carrier lifetime which are on order of magnitude lower with respect to what is typical measured for silicon MRRs where the free carrier lifetime is of the order of *ns*.

Given the importance of the free carrier lifetime, it is therefore necessary to make a careful estimate of the free carrier lifetime to determine the amount of non-linear loss, FCD, and power absorbed in MRRs. To this end, accurate modelling of the carrier lifetime is required so that the maximum power incident in the ring from the laser gain section (see Fig. 1.6) can be predicted (keeping the ring transmission unaltered from its linear characteristic). It is important to remind that many of the available models of NL effects in MRRs in the literature are based on the empirical values of the carrier lifetime obtained by fitting experimental measurements [55, 41, 56]. The main objective of this thesis is to present a model that, together with nonlinearity and self-heating, includes the formulation of Shockley-Read-Hall theory for the recombination of carriers in order to find the spectral responses of MRRs with different geometries in non-linear regime self-consistently. The capabilities of the model are demonstrated through measurements and design of ring resonators.

1.5 Thesis organization

This thesis is organised as follows. In chapter 2 we set the basis for the study of the MRRs by introducing the optical parameters in mircoring and the electromagnetic and thermal simulations performed to calculate them.
Chapter 3 is dedicated to the description of the model we developed by including the mechanisms related to nonlinear effects in silicon in both stedy state and pump-probe experiments. We also introduce a distributed version of our steady state model to model MRRs with generic waveguide cross-section where diffusion and heat spreading are of fundamental importance.
Then in chapter 4 we show that the developed model is able to reproduce measured ring transmission spectra in both steady state (SS) and pump-probe experiment with

physically sound-appropriate parameters [58, 88]. We also analyse MRRs consisting of polysilicon and silicon waveguides (Si/poly-Si MRR) and propose a method for determining the impact of grain size on NL effects in polysilicon [95–97] by extracting the nonlinear losses and FCD coefficients [98]. In fact these two quantities are well reported for silicon [38] but not yet documented in the case of polysilicon. To exemplify the strength of the developed model, in chapter 5 we show how it can be employed to model MRRs of an hybrid tunable laser with the aim of reducing NL effects. Chapter 6 summarizes the conclusions of this work and future prospectives. Figure 1.7 summarises the main topics threaded in this thesis with references associated to chapter and sections.

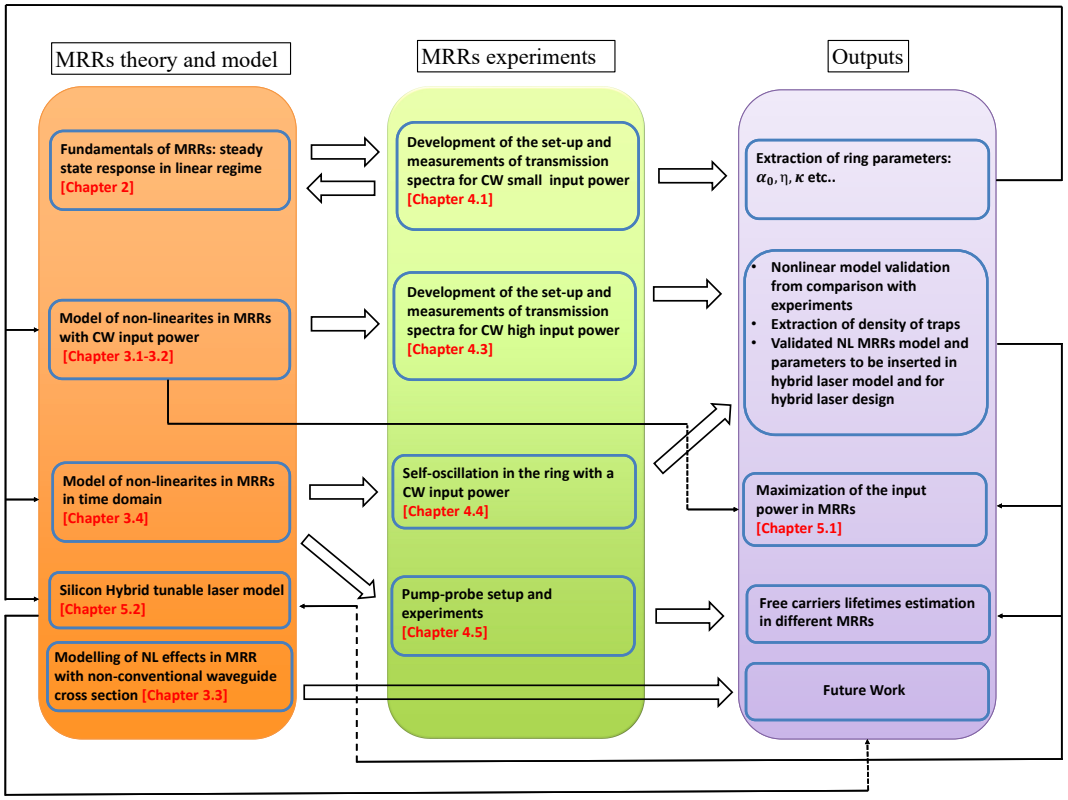

Fig. 1.7 Conceptual map of the topics analysed in this thesis divided in theoretical, experimental and output sections.

Chapter 2

Silicon microring resonators: electromagnetic and thermal modelling

2.1 Fundamental concepts of microresonators

A microring resonator is a resonant cavity which is the result of a looped waveguide where light can circulate either clockwise or counterclockwise. The term ring refers to circular-shaped resonators, whereas racetrack is used in all other cases. All the equations and theory derived hereafter are valid in both cases since the only geometrical difference between the two is the total resonator length.
Power can be injected in the MRR by coupling the evanescent light from one (all-pass configuration) or two straight waveguides (add-drop) represented by the coupling coefficient κ. Regardless of the configuration, if the phase shift of the roundtrip is a multiple of 2π, the resonator is on resonance and constructive interference occurs inside it. This causes a build-up of the circulating power P_c that can be as large as $100\,mW$ for just some mW of bus power. In an add-drop configuration destructive interference occurs at the through port which presents the minimum output power, the drop port experiences the maximum output power resulting from the circulating power build-up. Therefore a MRR support multiple resonances, in other words it has spectral response showing periodic peaks and dips at the drop and through ports respectively, as shown in Fig 2.1

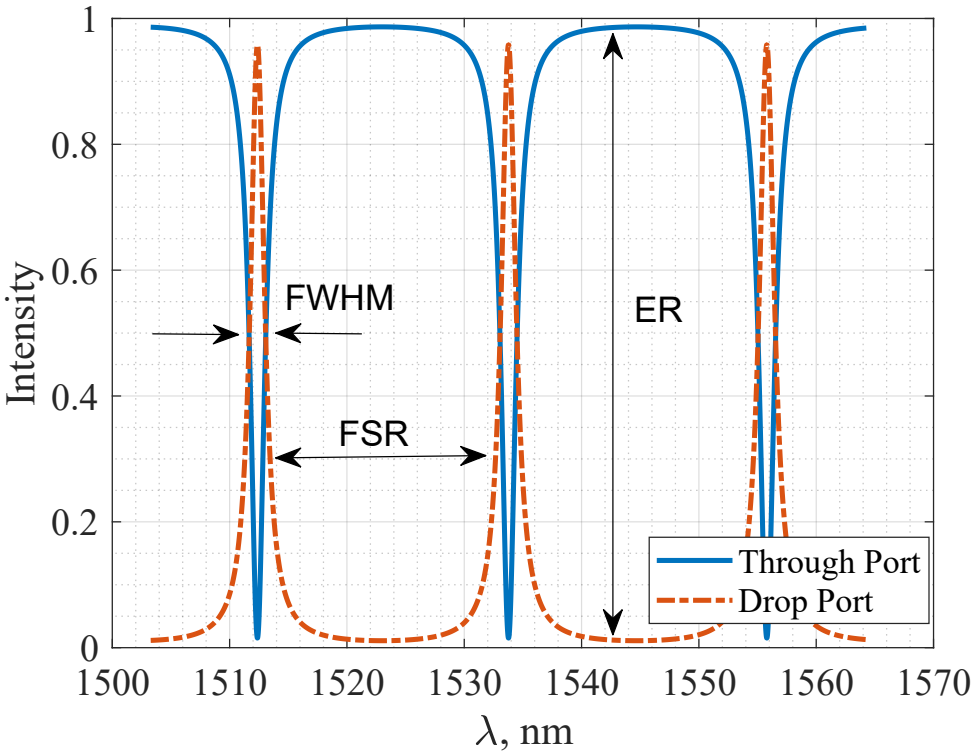

Fig. 2.1 Spectral response of an add-drop MRR. Here the resonator is lossy, as a result at resonance the output intensity is not 1 (0) at the through (drop) port resulting in finite extinction ratio (ER) defined as $ER = \frac{P_{thr,out,res}}{P_{thr,res}}$ where $P_{thr,out,res}$ and $P_{thr,res}$ are the output power at the through port out of resonance and at resonance respectively.

At resonance we have that:

$$\lambda_0 = n_{eff,0} L/m \tag{2.1}$$

where n_{eff} is the effective refractive index of the waveguide, L the total MRR length and m an integer number.

The general structure of the ring and racetrack resonators analysed in this thesis is shown in Fig. 2.2; in the case of a racetrack configuration, L_c is the coupler length and L_d the length of the straight waveguide, r is the curvature radius. For the classic ring configuration we have $L_c = L_d = 0$. The coupler has coupling coefficient κ and transmission coefficient t. The coupling loss in the bus-ring coupling region is indicated with parameter η^2, such that, defining P_{bus} the power entering in the coupler, the power loss per round trip in this region is $\eta^2 \cdot P_{bus}$ [99]. Here we assume

that the coupling coefficients of the top and bottom bus waveguides, i.e., κ_1 and κ_2 respectively, are equal; this holds for the racetrack resonator whereas they are generally different in the case of the Si and Si/poly-Si rings.
The power conservation in the bus-ring coupling region is therefore $t^2 + \kappa^2(1-\eta^2) + \eta^2 = 1$ from which we get $t^2 = (1-\kappa^2)(1-\eta^2)$.

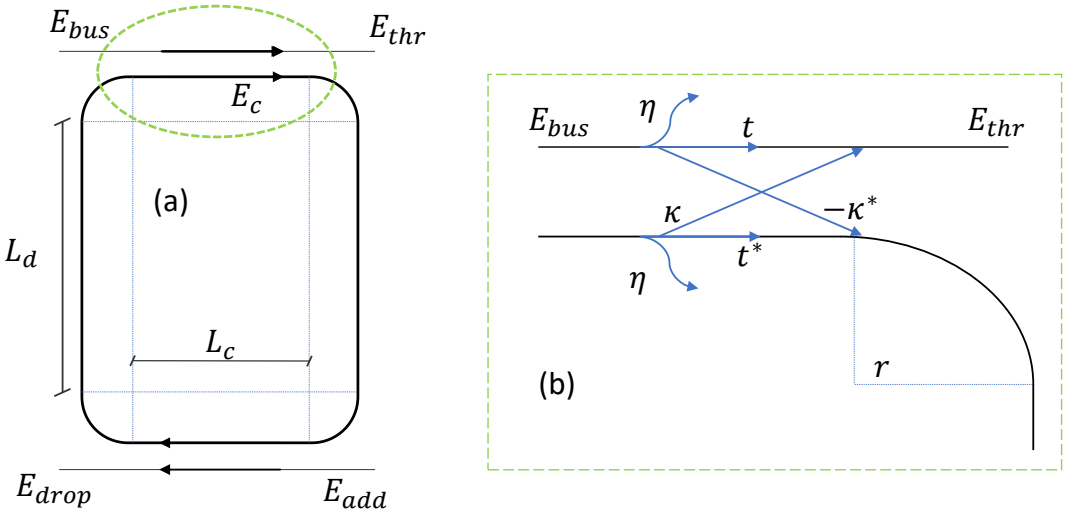

Fig. 2.2 (a) Schematic of the resonator structure and zoom in the bus-ring coupling region (b). The electric fields at the input bus port (E_{bus}), through port (E_{thr}), add (E_{add}), and drop (E_{drops}) ports are normalized such that $|E|^2$ is a power in Watt. The electric field propagating in the ring waveguide is E_c.

During the propagation in the ring, the field experiences modal losses expressed as $a = e^{-\alpha_{eff}L/2}$, where α_{eff} is:

$$\alpha_{eff} = \alpha_0 + \alpha_{rad}, \tag{2.2}$$

α_0 is the liner loss term attributed to light scattering, residual doping and single photon absorption (SPA) [100] in the silicon core, while α_{rad} is the term accounting for the bend loss and therefore for light radiated in the cladding. With this formulation, the power transmission coefficients at the through port is:

$$T_{thr} = t^2 \frac{|1-(1-\eta^2)ae^{j\theta}|^2}{|1-t^2ae^{j\theta}|^2}, \tag{2.3}$$

whereas at the drop port it is:

$$T_{drop} = \frac{\kappa^4(1-\eta^2)^2 a}{|1-t^2 a e^{j\theta}|^2}. \tag{2.4}$$

The optical power circulating in the ring waveguide can be calculated as shown in Appendix A:

$$P_c = P_{bus}\frac{\kappa^2(1-\eta^2)}{|1-t^2 a e^{j\theta}|^2} \tag{2.5}$$

θ is the total phase variation per round trip:

$$\theta = \theta_0 + \frac{n_g}{c}(\omega-\omega_0)L \tag{2.6}$$

θ_0 is the phase variation per round trip at the reference angular pulsation at resonance (ω_0) n_g is group refractive index which is a function of the effective refractive index in the resonator. It is generally defined as [101]:

$$n_g = n_{eff,0} - \lambda\frac{\partial n_{eff,0}}{\partial\lambda}, \tag{2.7}$$

that takes into account the effective refractive index dispersion of the propagating mode in the waveguide. Fig. 2.3 represents an example of the calculated group index in the case of a silicon straight waveguide with height h and width W equal to $107\,nm$ and $580\,nm$ respectively using Photon Design electromagnetic simulation. This rather high group velocity dispersion is related to the lower field confinement in the waveguide caused by dispersion in silicon [102].

Other important FOMs in the description of MRRs are the free spectral range (FSR), quality factor (Q), and finesse (F). The former is the distance between two adjacent resonance peaks, whereas the quality factor of a resonator represents the sharpness of a specific resonance. It is computed as [101]:

$$Q = \frac{\lambda_0}{FWHM}, \tag{2.8}$$

where FWHM is the full-width-half-maximum of the resonance peak as shown in figure 2.1. It also indicates how much power is circulating in the MRR; a large Q is associated with an high P_c, which leads to stronger NL effects when compared to a MRR with a smaller Q for the same input power, round trip losses and finesse [101].

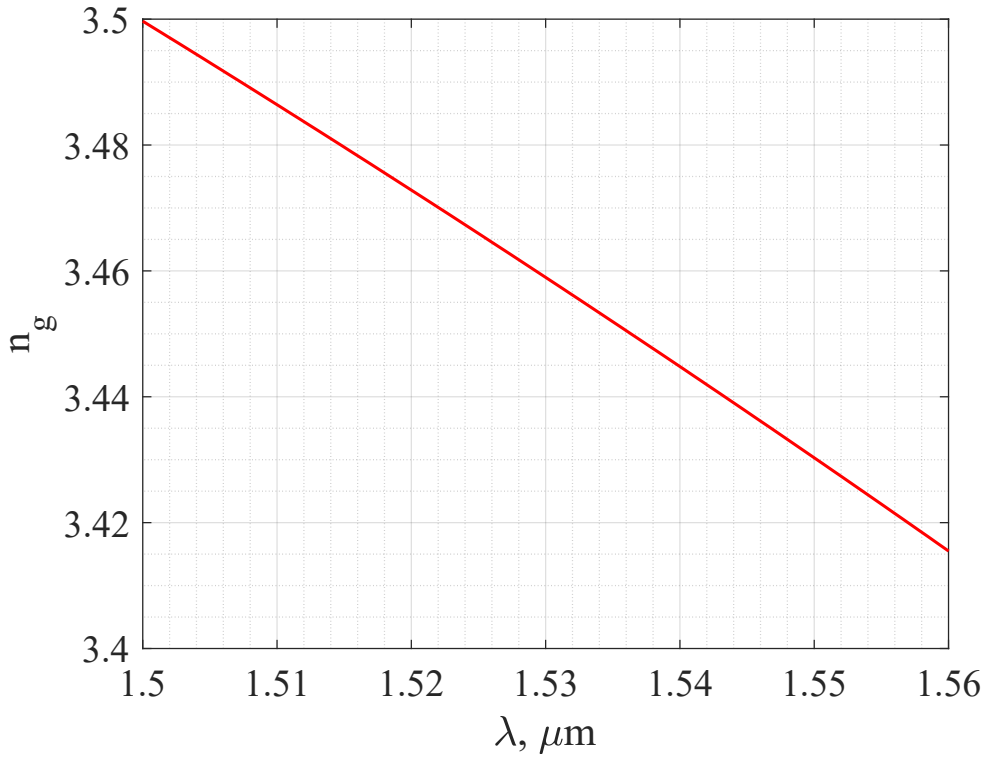

Fig. 2.3 Group index calculated with an optical mode solver in the case of a Si waveguide with cross section 107x580nm [103, 104].

The latter is defined as the ratio of the FSR and the FWHM. Lastly, we note that eq. (2.5) at resonance is a linear function with respect to the bus power that depends only on the ring characteristic:

$$P_{c,res} = P_{bus} \frac{\kappa^2(1-\eta^2)}{|1-t^2 a|^2} \tag{2.9}$$

If we consider the propagation and coupling losses to be negligible and in the case $\kappa << 1$, eq. (2.9) can be directly linked to the finesse as [101]

$$P_{c,res} = P_{bus} \frac{F}{\pi}, \tag{2.10}$$

under the same approximations it also holds that $Q = \frac{n_{eff,0}L}{\lambda_0} F$, therefore $P_{c,res} = P_{bus} \frac{Q\lambda_0}{n_{eff,0}L\pi}$.
When the ring experiences asymmetrical coupling coefficients, i.e., $\kappa_1 \neq \kappa_2$, a new

expression for the transmission coefficient is needed. For example we consider the structure shown in Fig. 2.4 where the input field is injected from a splitter on the left side of the ring to the bottom and upper arms. This particular configuration has been chosen in order to be as close as possible to the structure implemented in figure 1.6 for the passive mirror of the hybrid tunable laser.

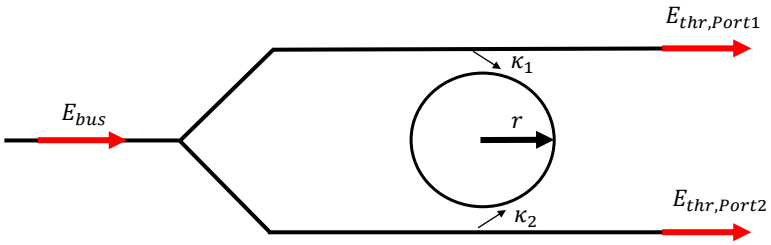

Fig. 2.4 Schematic configuration of a MRR where the power is injected in both upper and lower arms thanks to a splitter.

In this case, the output power can be collected either on top or bottom right output ports which are considered to be through port. For these rings, we mark the two ports mentioned above as port1 and port2. Eq. (2.3) becomes at port1:

$$T_{thr,Port1} = \left| t_1^2 - \frac{\kappa_1^2 t_2 a e^{j\theta}(1-\eta^2)}{1 - t_1 t_2 a e^{j\theta}} \right|^2, \tag{2.11}$$

while at port2 we have:

$$T_{thr,Port2} = \left| t_2^2 - \frac{\kappa_2^2 t_1 a e^{j\theta}(1-\eta^2)}{1 - t_1 t_2 a e^{j\theta}} \right|^2. \tag{2.12}$$

Figure 2.5 shows an example of the transmission at both port1 and port2 for a ring of radius $r = 5\,\mu m$.

2.1.1 Coupling regimes

MRRs can work in different coupling regimes depending on the coupling coefficient which is influenced by the bus-ring distance. Considering the simple case of an

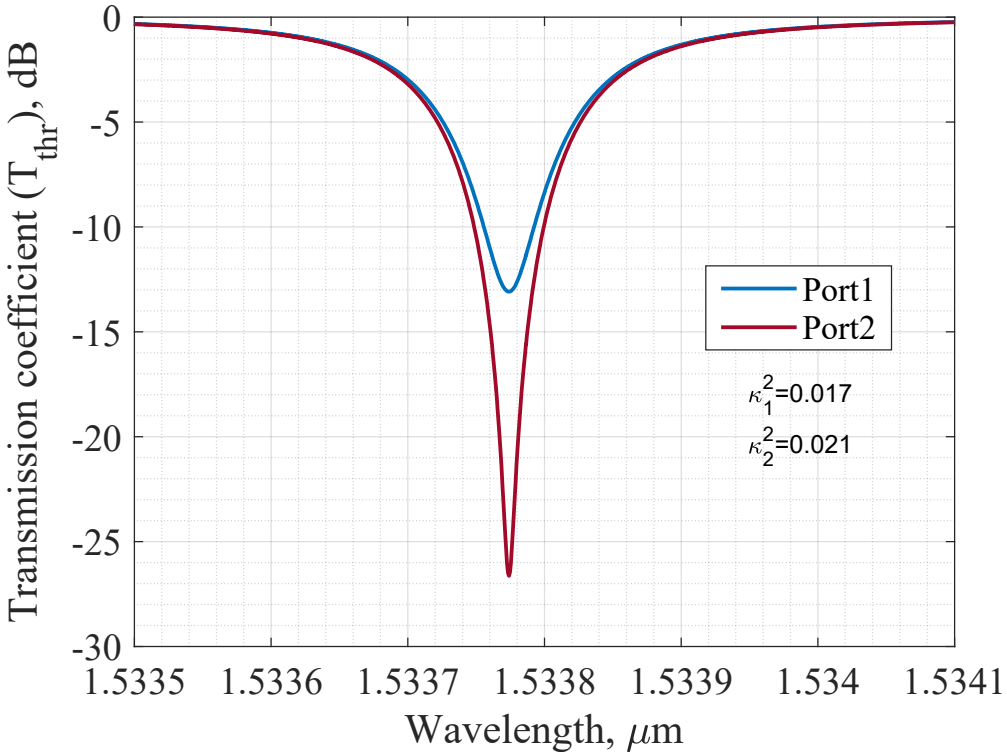

Fig. 2.5 Spectral response of a ring resonator with radius $r = 5\,\mu m$ at Port1 and Port2 with the parameters:$\kappa_1^2 = 0.017$,$\kappa_2^2 = 0.021$, $\alpha_0 = 1.02\,dB/cm$, $\alpha_{rad} = 1.73\,dB/cm$, $n_g = 3.45$, $n_{eff} = 1.95$, $\eta^2 = 0.002$.

all-pass MRR, the transmission coefficient is:

$$T_{thr,ALL} = \left| t^2 - \frac{\kappa^2 a e^{j\theta}}{1 - t a e^{j\theta}} \right|^2, \tag{2.13}$$

where we neglected bend and coupling losses. Depending on the value the transmission coefficient t assumes with respect to the propagation losses a, the MRR can be in three different regimes [105]. The ring is in the undercoupled regime when $t < a$, while $t = a$ corresponds to the critical coupling, and $a < t < 1$ to the overcoupled regime as illustrated in figure 2.6. The bus waveguide and ring distance for which critical coupling occurs is defined as d_{crit}, and it is particular important since at this value the MRR shows the highest possible quality factor. However due do tolerances during the fabrication process, it is usually difficult to ensure perfect critical coupling. This is especially true in the case of add-drop MRR where this

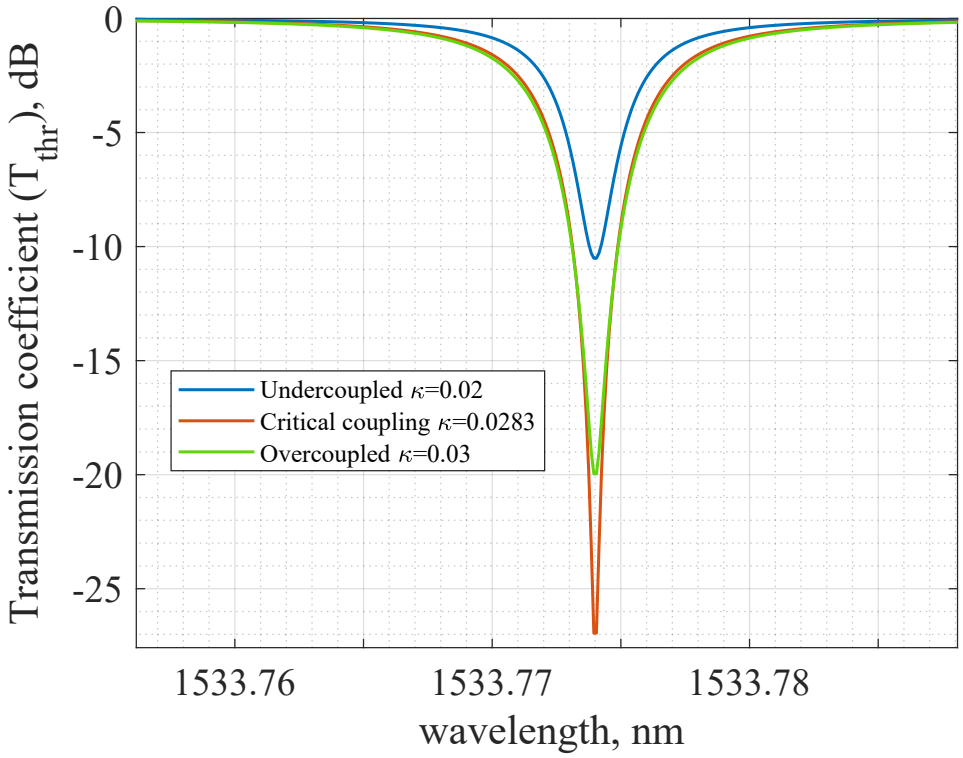

Fig. 2.6 Spectral response of an all-pass ring resonator with the parameters: $\alpha_0 = 1.02\,dB/cm$, $\alpha_{rad} = 1.73\,dB/cm$, $n_g = 3.45$, $n_{eff} = 1.95$.

condition happens only when $t_1 = at_2$ [106]. When the latter is not satisfied one port will be undercoupled ($t_1 < at_2$) and the other one overcoupled ($at_2 < t_1 < 1$).

2.2 Optical simulations

In order to develop a model that simulates rings in linear and NL regime some important optical parameters are needed. For example the confinement factor Γ and the waveguide effective area A_{eff} of the mode propagating in the waveguide are important parameters which affects the impact of NL effects in the ring. These quantities depends on the electromagnetic fields propagating in the resonators.
To this aim, the optical mode solver FIMMWAVE by Photon Design, was used to compute the optical modes in the ring cross section. In this framework three main solver are suited for our case: the film mode matching method (FMM), a finite difference method (FDM) and a finite element method (FEM). All results were

obtained by using the FMM, which is a semi-analytical solver based on the work by Sudbo [103, 115]. The solver locates almost any horizontal or vertical mode order of arbitrary or mixed polarisation. Since the FMM method is analytical, its speed and accuracy are superior than any numerical technique such as FDM and FEM. This makes the FMM solver of choice for epitaxially grown structures or generally for waveguides which have large parts of uniform refractive index such as the substrate and oxide typical of the SOI ring resonators. The FMM also includes a bend solver version which computes the modes of bent waveguides in cylindrical coordinates, which has been employed to calculate the bending loss for different radii.

2.2.1 FMM method

Given a rectangular-based structure, it can be divided in a a series of slices in which there is no refractive index variation in the x-direction, see fig. 2.7 (a). Thanks to this restriction, it is possible to represent an arbitrary physical field profile in the waveguide as a linear combination of vertical 1D modes of each slice; these 1D modes can be TE or TM polarised and represent the modes that would be found assuming the slice to be infinitely wide. In a given slice, any electro-magnetic field that is solution of Maxwell's equations can be expressed as a linear combination of all the 1D TE and TM modes according to:

$$F(x,y) = \sum_{j=1}^{(1D)nmode} [u_j^{TE} e^{ik_{xj}^{TE} x} \phi_j^{TE}(y) + u_j^{TM} e^{ik_{xj}^{TM} x} \phi_j^{TM}(y)]. \tag{2.14}$$

Here $u_j^{TE/TM}$is the mode amplitude for the 1D mode, $\phi_j^{TE/TM}$ the 1D field profile, and $k_{xj}^{TE/TM}$ the wavevectors. (1D) nmode is an input parameter in the solver and defines the total number of 1D modes to be considered in each slice. Since this method is rigours, the only limitation is given by the number of modes chosen for the simulation.

Once $F(x,y)$ has been computed, the 2D modes are obtained by solving the eigen-system generated by the propagation of the vertical modes in the x-direction. The appropriate number of 1D modes is usually determined by observing when the calculated effective refractive index index does not change as the number of modes increases.

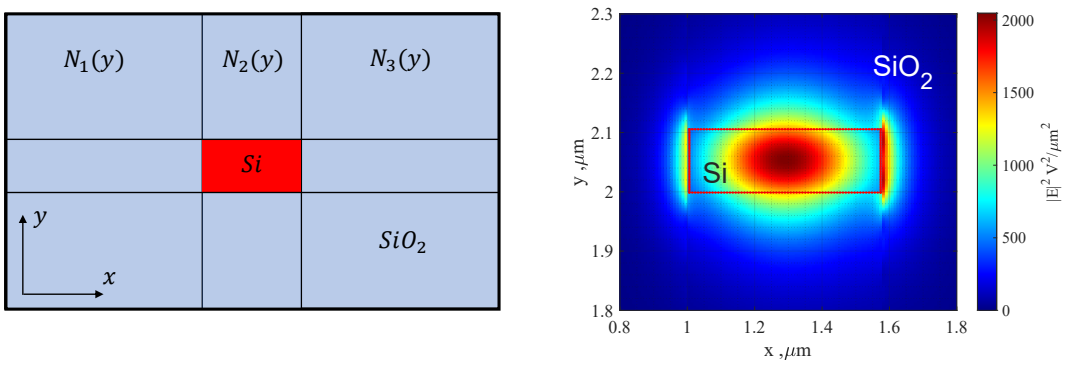

(a) (b)

Fig. 2.7 (a) Schematic of the slices division in the FMM method for the simple case of a rectangular Si waveguide. (b) Electric field in a waveguide with parameters listed in figure 2.5 for the fundamental mode at 1.533 μm, the asymmetry in field distribution is related to the waveguide bending.

When dealing with a rectangular bent waveguide, two types of boundary conditions (BCs) can be chosen on the leaky side, i.e., the outer direction of the bend: perfectly matched layers (PML) (PML) and transparent boundary condition (TBC) (TBC) [116]. Both BCs have to ensure that the radiated field is not reflected back at the boundary so that the solver is able to find a correct solution of the problem. In the PML case the wave is simply absorbed by a matched absorbing layer with variable width. The latter must be long enough to ensure complete absorption of the radiated wave. This problem is avoided with TBC where the whole travelling wave is analytically transmitted at the radiation boundary without any reflection. The convergence and accuracy of TBC depend on the complexity of the applied condition [116]. In fig. 2.7 (b) the complex FMM method with TBC has been used to retrieve the electric field distribution in the case of the bent waveguide whose parameters are listed in figure 2.5. It is interesting to see that the fundamental mode is not symmetric due to the non-negligible mode leakage in the waveguide towards the outer (right) side of the simulation window. As a result a TE field propagating in the ring will suffer bend losses α_{rad} as radiated mode, since we have $\alpha_{rad} = 1.73\,dB/cm$.

2.2.2 Optical parameters: optical confinement factor and effective area

Thanks to the FMM method, we are able to compute the transversal complex electric and magnetic field profiles of the fundamental guided mode $E(x,y)$ and $H(x,y)$ respectively. These fields are of great importance since they are needed in the computation of the optical confinement factor (Γ) and the effective area A_{eff}. Given a mode of order μ, frequency ω, and propagation constant β_μ, we have [117]:

$$\boldsymbol{E}_\mu(r,t) = \Re e\left(A_\mu(z,t)\frac{E_\mu(x,y,\omega)}{\sqrt{P_{n,\mu}}}e^{j(\omega t-\beta_\mu(\omega)z)}\right) \tag{2.15}$$

For the electric field, while for the magnetic field:

$$\boldsymbol{H}_\mu(r,t) = \Re e\left(A_\mu(z,t)\frac{H_\mu(x,y,\omega)}{\sqrt{P_{n,\mu}}}e^{j(\omega t-\beta_\mu(\omega)z)}\right). \tag{2.16}$$

$|A_\mu|^2$ corresponds to the average power in the waveguide, and $P_{n,\mu}$ is the power normalization constant for the mode μ such that:

$$P_{n,\mu} = \frac{1}{2}\int_{-\infty}^{+\infty}\int_{-\infty}^{+\infty}\Re e\left(E_\mu(x,y,\omega)\times H_\mu^*(x,y,\omega)\right)\cdot \boldsymbol{e}_z dxdy \tag{2.17}$$

with e_z the unit vector pointing in the propagation direction z.
The optical confinement factor (Γ) in the silicon cross section of the waveguide is [118, 119] :

$$\Gamma = \frac{n_{Si}c\varepsilon_0\int\int_A \left|E_\mu(x,y)\right|^2 dxdy}{\int\int_{A_{tot}}\Re e\left\{E_\mu(x,y)\times H_\mu(x,y)\right\}\cdot e_z dxdy}. \tag{2.18}$$

Where A is the area of the silicon cross section of the waveguide as in Fig.2.7 (b); A_{tot} is the total area of the simulation domain (including both Si and SiO_2) where the electromagnetic field has been computed. $n_{Si} = 3.48$ is the refractive index of Silicon. This definition of Γ refers to how well the optical medium is able to confine the light [118, 119], it can be slightly larger than one indicating the possibility of having a better field confinement in a waveguide than in the bulk case, a proof is shown in appendix A. Note that Γ is different from the so called filling factor, defined as:

$$FF = \frac{\int\int_A \Re e\{E_\mu(x,y) \times H_\mu(x,y)\} \cdot e_z dxdy}{\int\int_{A_{tot}} \Re e\{E_\mu(x,y) \times H_\mu(x,y)\} \cdot e_z dxdy} \tag{2.19}$$

Which is a measure of the mode power in the core waveguide with respect to the total power.

The effective area A_{eff} is defined accordingly to the model in [117]:

$$A_{eff} = \frac{Z_0^2}{n_{Si}^2} \frac{\left|\int\int_{A_{tot}} \Re e\{E_\mu(x,y) \times H_\mu(x,y)\} \cdot e_z dxdy\right|^2}{\int\int_A \left|E_\mu(x,y)\right|^4 dxdy} \tag{2.20}$$

$Z_0 = 377\,\Omega$ is the free-space wave impedance. The effective area is a measure of the nonlinear interaction of the optical field with Silicon; as it will be shown later, the generation of free carriers caused by light interaction with the material goes as $1/A_{eff}$.

Eq. (2.20) is completely general and holds for any refractive index contrast between the core and cladding, in the particular case of low contrast index waveguide it simplifies to the well-known expression [120]:

$$A_{eff} = \frac{\left(\int\int_{A_{tot}} \left|E_\mu(x,y)\right|^2\right)^2}{\int\int_A \left|E_\mu(x,y)\right|^4 dxdy} \tag{2.21}$$

Figure 2.8 collects the different waveguides parameters needed for the linear and NL modelling of waveguides and MRR in the example case of ring analysed in figure 2.5.

As it is possible to see Γ decreases as the wavelength increases. The same applies to the effective refractive and group indexes as explained earlier. While the bend losses and A_{eff} follow the opposite trend. Since the field is less confined in the structure as the wavelength increases, a larger portion of the field is radiated outside of the core causing an increment in bend losses.

To verify the correctness of our methodology, and of the expressions we implemented in eq. (2.18)-(2.20) we analysed the same structure proposed by the work of Koos et al. in [117], where they computed the effective area of a strip silicon waveguide with $W_{Si} = 400\,nm$ and $h_{Si} = 200\,nm$. Here the refractive index of the cover material is sweeped from 1 to 2.5. In Fig. 2.9 are able to accurately get the same values as in [117], meaning that the complex FMM method with TBCs and eq. (2.18)-(2.20) are

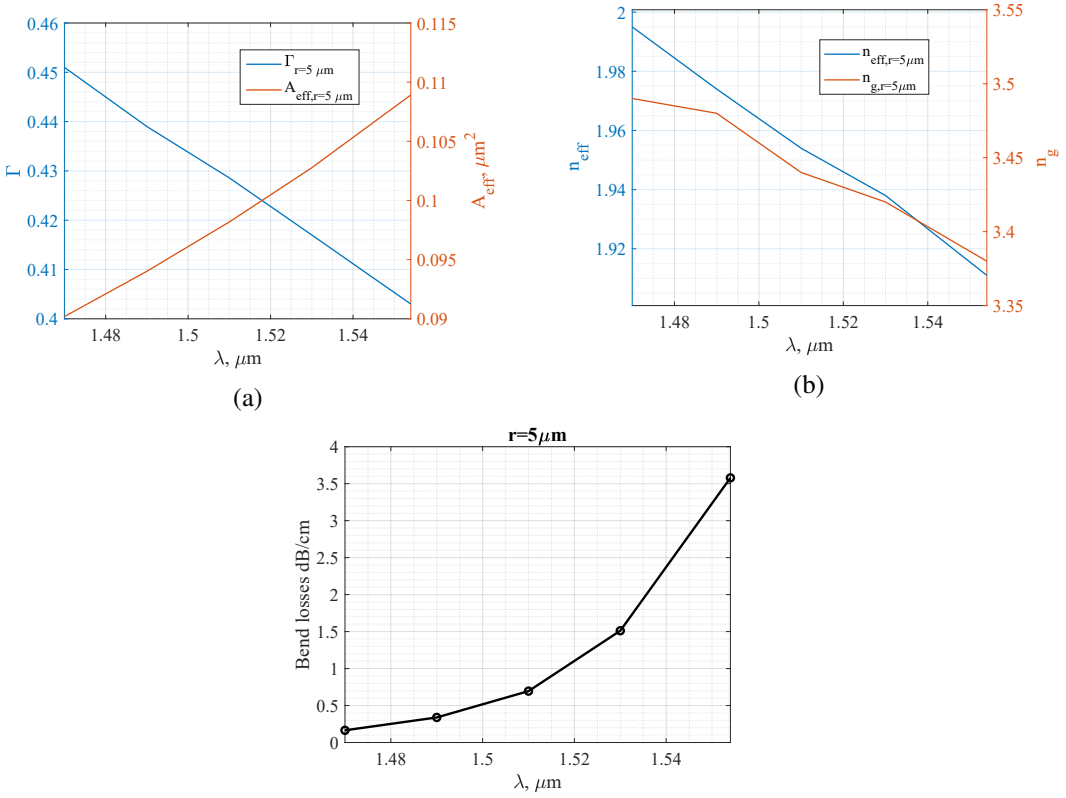

Fig. 2.8 Main parameters as a function of wavelength for the same waveguide of figure 2.5 obtained with the complex FMM method with TBCs; (a) Optical confinement factor and effective area; (b) effective index and group index; (c) bend losses.

consistent.

2.3 Thermal analysis

Self-heating in MRRs can be modelled by the so called thermal impedance of the ring Z_T which regulates the heat influence on the silicon refractive index caused by free carriers recombination. COMSOL has been used for thermal simulation of the complete resonator structures. Heat is generated in a silicon MRR in the self-heating process caused by the recombination and relaxation of free carriers generated by TPA and FCA. A MRR is a complex structure made of a silicon waveguide surrounded

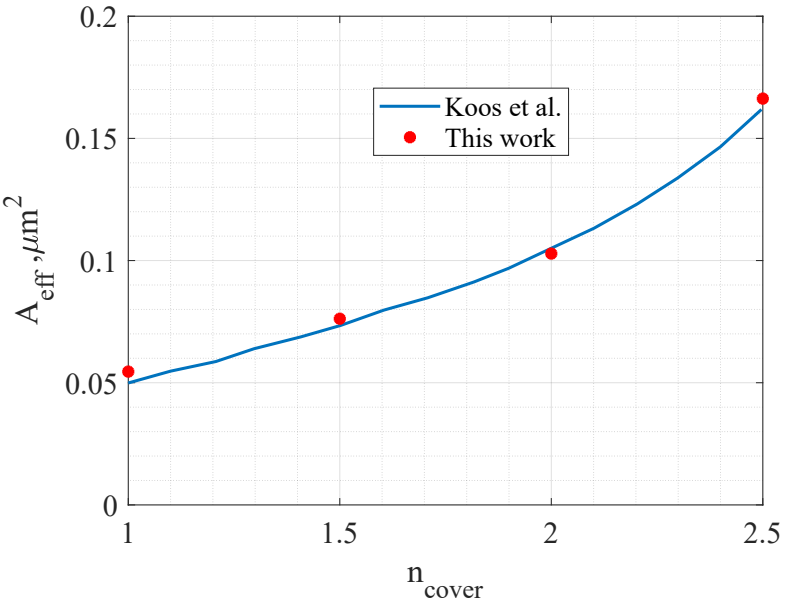

Fig. 2.9 Comparison of the effective area of a strip Silicon waveguide with SiO_2 as substrate and with variable refractive index from 1 to 2.5 in the cover. $W_{Si} = 400\,nm$ and $h_{Si} = 200\,nm$. Blue data reproduced from figure 3 (b) in [117].

by silicon oxide, silicon substrate, and air on top., since silicon oxide has a thermal conductivity ($k_{SiO_2} = 1.4\,\frac{W}{k \cdot m}$) much lower than silicon, the ring dissipates the heat with difficulty.

This property is taken into account in the so called thermal impedance of the ring defined in stationary regime and for strip waveguides as:

$$Z_T = \frac{\Delta T}{P_{abs}}. \tag{2.22}$$

With $\Delta T = T_{max} - T_0$; T_{max} is the temperature excursion in the core caused by heat generated through absorbed power P_{abs}, and T_0 is the ambient temperature set at $293.15K$. The lower Z_T the better is the thermal dissipation of the ring.

2.3.1 Thermal model

We use the COMSOL Multiphysic thermodynamic software to simulate the heat propagation inside the resonators. Here thermal transport is generally modelled

through the heat equation:

$$\rho(r)\cdot C_p(r)\left(\frac{\partial T(t,r)}{\partial t}\right)-\nabla\cdot(K(r)\nabla T(t,r))=Q(t,r), \tag{2.23}$$

$\rho(r)$, $C_p(r)$, and $K(r)$ are respectively the density (mass per unit volume) of the material, specific heat and thermal conductivity in the structure which are space dependent due to the different materials involved. $Q(r,t)$ is the heat source, in our case we assume the heat is generated uniformly in the silicon waveguide core with volume V_{Si}:

$$Q(t)=P_{abs}(t)/V_{Si} \tag{2.24}$$

In steady state, the rate of absorbed power by the resonator is constant, as a result the first term in eq. (2.23) is zero.

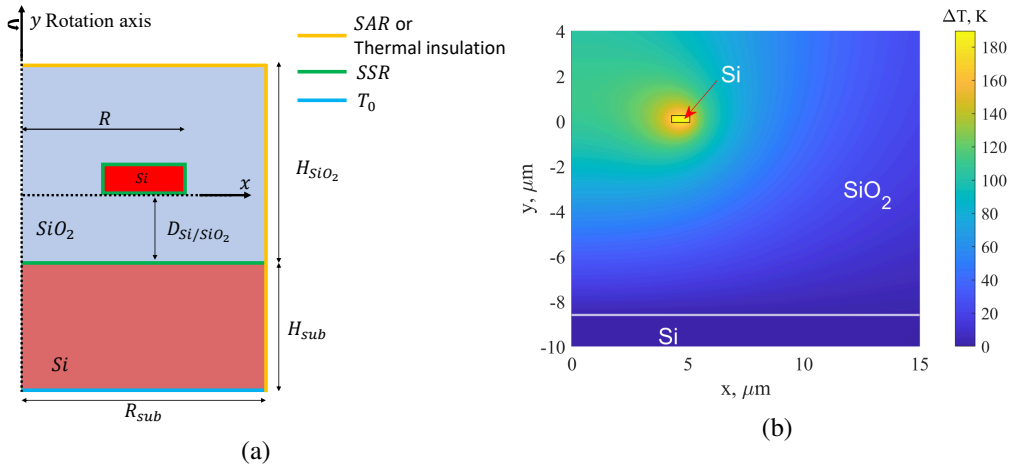

Fig. 2.10 (a) Cross-section of a silcon MRR, the cladding is silicon oxide on a silicon substrate. The different colors at the interfaces refer to the type of boundary conditions necessary to model the heat transfer between the different materials and with the environment; these are surface-to-surface radiation (SSR) and surface-to-ambient radiation (SAR). (b) Map of temperature increase in the MRR.

By exploiting the symmetry of the ring cross-section around its rotation axis, it is possible to avoid the full 3D simulation in the case of MRRs through the so called 2D Axysimmetric approximation.
Such approximation is not possible in the case of the racetrack resonator where the complete 3D model must be employed. In both cases eq. (2.23) is in cylindrical coordinates and solved with a FEM method. Fig. 2.10 shows the typical resonator

structure we consider in our study. Here the bending radius is R, whereas R_{sub} is the radius of the silicon disk composing the substrate. H_{sub},H_{SiO_2}, D_{Si/SiO_2}, are all geometrical quantities related to the foundry specification. D_{Si/SiO_2} is the distance between the waveguide and the Si susbtrate, it is a critical parameter for heat dissipation. In fact the larger this distance is, the worst the heat dissipation will be in the device due to the larger volume of oxide surrounding the silicon core. On the other hand a too small D_{Si/SiO_2} would make the guided mode in the waveguide coupled with the silicon substrate. In Fig. 2.10 (b) the heat over one section of a MRR is shown in the case of an absorbed power of $10\,mW$.

It is important to remind that heat transfer in the resonator is through conduction and convection. However the type of contact between the different material surfaces, as shown in Fig. 2.10, takes into account additional types of irradiation:

- Surface-to-surface radiation (SSR): it defines the heat transfer between two semi-transparent media by radiation. It is relevant when there is a non-negligible difference of temperature between two media and the emissivity ε_T, i.e., the ability of emitting radiation in comparison to a perfect black body ($\varepsilon_T = 1$) is larger than zero. As a result a portion of the radiation is transmitted over the surface and a portion is reflected back. In our case $\varepsilon_T = 0.7$ for both Si and SiO_2[121].

- Surface-to-Ambient radiation (SAR): these boundary conditions are used when heat is radiated from the domain to the environment, which is composed by air in our case.

- Thermal insulation: It is a BC that can be used at the outer edges of the structure that are in contact with the air. With this condition, the system is considered to be adiabatic and the additional air layers can be avoided. Such BC produces the same results as in the case of SAR, but due to reduced simulation space (since we no longer need the air layers), the simulation computational time is lower.

To validate the approach implemented in Comsol, we take into account the work done by Soltani in [122] where the author analysed the thermal conductance ($1/Z_T$) of a silicon microdisk resonator in steady state whose cross-section is shown in figure 2.11 (a) with $r = 20\,\mu m$.

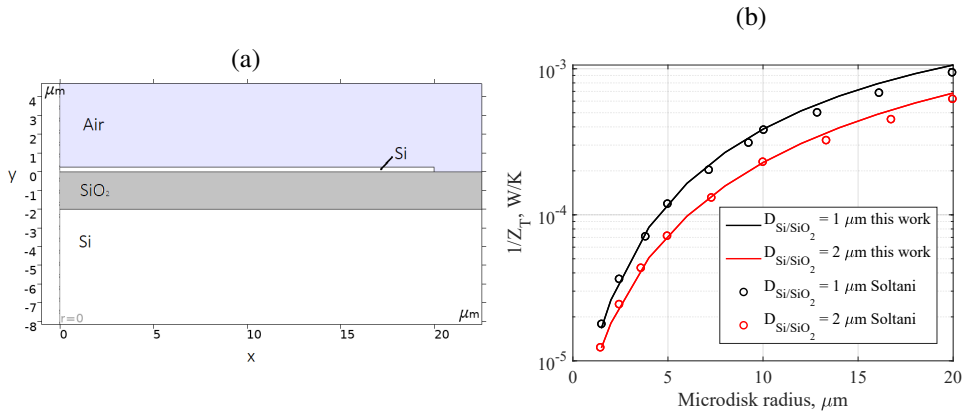

Fig. 2.11 (a) Cross section of the silicon microdisk reproduced from [122] for a microdisk radius of $r = 20\,\mu m$. (b) Thermal conductance of the microdisk for two different oxide thicknesses as a function of the microdisk radius. Our model results are compared with those by Soltani [122].

Here, we report results on two different oxide substrate thicknesses (D_{Si/SiO_2}) with $P_{abs} = 10\,mW$ uniformly distributed on the border of $2\mu m$ of the microdisk radius as shown in [122] through electromagnetic simulation of the fundamental mode distribution in the microdisk. As mentioned earlier, an higher thickness of SiO_2 is associated with lower thermal conductivity (higher thermal impedance). Our thermal model can reproduce the results of [122].

Stationary regime thermal analysis

The same procedure has been applied to MRR analysed before, the resulting thermal impedance is plotted in fig. 2.12. Th good matching between full 3D model and the 2D Axysimmetric approximation prove that the two method are equivalent for simulating thermal conduction in MRRs. We note that the thermal impedance decreases with increasing resonator length since the area where heat can be dissipated increases and therefore the structure dissipates heat more easily.

Dynamic regime thermal analysis

In some cases and for certain levels of input CW optical power, the ring can enter in a self-oscillation regime characterised by periodic oscillations of the resonant wavelength. During these self-oscillation the power entering in the ring is high

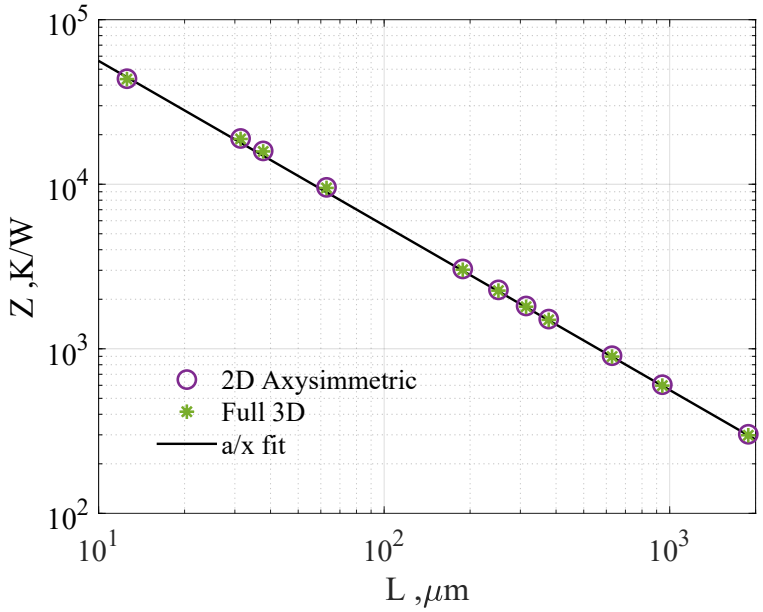

Fig. 2.12 Thermal impedance of a MRR as a function of the total resonator length. Results of 2D Axysimmetric and full 3d thermal simulation are indicated with circles and asterisks; whereas the black line represents a fitting of the type $y = a/x$.

enough that the free carriers lifetime becomes comparable with the resonator thermal time-constants [122, 123]. To calculate these time constants, we solve in COMSOL eq. (2.23); then the time dependent temperature variation in the ring is calculated when at $t = 0$ we start to dissipate $10mW$ of power in the silicon waveguide core. Results are shown in fig. 2.13 .

One of the most important outcome is that the transient response cannot be modelled by a single thermal time constant as done in other works [122–124], but multiple time constants are needed to characterize the thermal response of the resonator.
In this work we consider an equivalent electrical circuit called Foster model [125] made by the series of n nodes made by RC blocks as shown in the inset of Figure 2.13, where ΔT_i is the temperature variation at each node of the RC block. The total temperature variation in time is then:

$$\Delta T(t) = \sum_i^n \Delta T_i \cdot \left(1 - e^{\frac{t}{Z_{T,i} C_i}}\right). \tag{2.25}$$

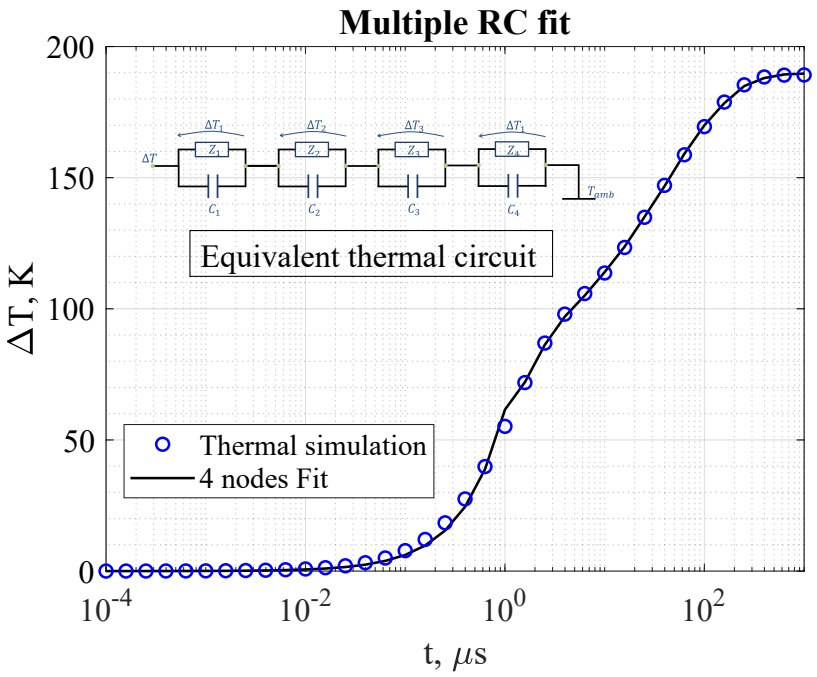

Fig. 2.13 Temperature variation versus time obtained from thermal transient simulation of the complete racetrack resonator in the case of a dissipated power set to $10\,mW$ starting from $t = 0$. In the inset the schematic of the equivalent circuit model is displayed.

We attribute the number of nodes to the heat flow between the stack of different Si and SiO_2 layers in the device structure; each node is the parallel between the thermal impedance Z_i and thermal capacitance C_i [125], whose product represents the thermal time constant [56, 123, 126]:

$$\tau_{th,i} = Z_{T,i} C_i, \tag{2.26}$$

By fitting the total temperature transient with eq. (2.25), $\tau_{th,i}$ and $Z_{T,i}$ can be obtained.

Chapter 3

Modelling of nonlinear effects in ring resonators

3.1 Overview of nonlinear effects in silicon

As introduced earlier, Silicon is affected, in both C- and O-band [60], by strong non-linear effects which cause a wavelength shift and distortion of the ring spectral response [41, 56, 57, 127] when the power injected in the ring increases. Fig. 3.1 (a) summarises these effects, here Two-photon-Absorption (TPA) and Free-Carrier-Absorption (FCA) are the main mechanisms responsible for the spectrum distortion [56]. In TPA, two photons are absorbed generating an electron-hole pair; these carriers can then absorb other photons due to free-carrier absorption (FCA) [41, 117, 127]; as a consequence, they are pushed to higher energies in conduction band or valence band. Therefore TPA and FCA rise the overall optical loss reducing the quality factor of the resonator. We refer to these free carriers as the free carrier density per unit volume n_e, in the conduction band, and p_e in the valence band. Apart from TPA, free carriers are also generated by surface-charge-absorption (SCA) [100, 128, 129], which is a one-photon transition related to intra-gap states located at the waveguide surface associated to surface state absoprtion (SSA), i.e., absorption of one photon promoted to intra-gap states which occur near the material surface. SCA is generally one order of magnitude lower in strength than TPA and often negligible.

The generated free-carriers (FCs) cause also a change in the refractive index called Free-carrier dispersion (FCD) which is responsible for a blue shift of the resonant wavelength of the ring. Whereas the relaxation of FCs (thermalization) and the recombination through SRH releases energy in form of heat (self-heating) which leads to a temperature increase in the resonator causing a thermal refractive index change and so a red shift of the ring resonant wavelength. Lastly radiative recombination is impossible in silicon, whereas Auger recombination is neglected in this thesis due to the low density of the generated free carriers [27]. We include also the Kerr effect as slight red shift of the refractive index variation, even if its contribution is negligible compared to FCA and self-heating.

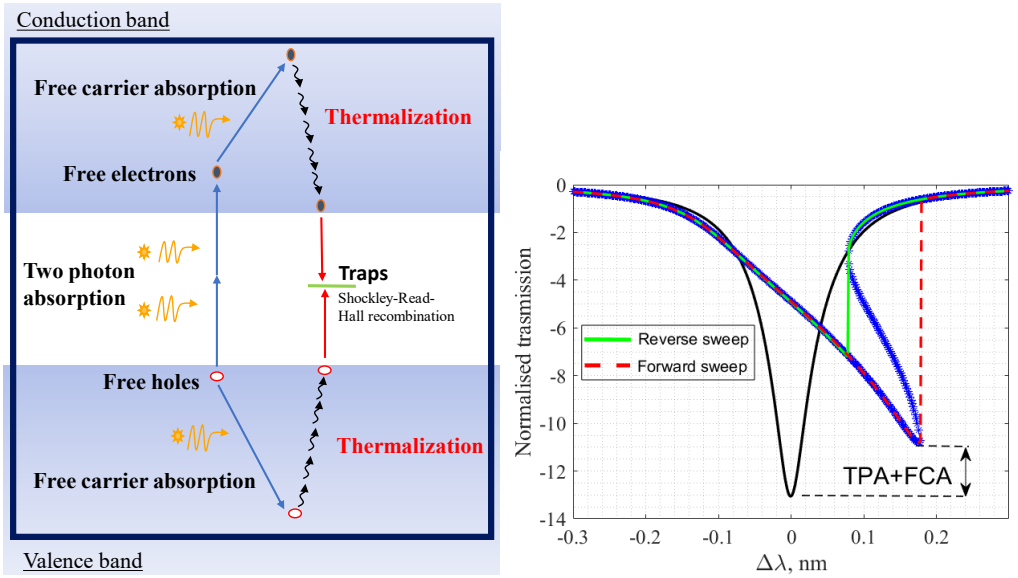

(a) (b)

Fig. 3.1 (a) Schematic of Si band diagram showing TPA, FCA, and self-heating effects due to free carriers thermalization. Carriers recombination is taken into account in the SRH formalism. (b) Modelled transmission spectrum of a MRR in linear (black curve) and NL regime (blue, red and green) showing the impact on NL effects and bistability in the ring with $P_{bus} = 2mW$. The blue curve represents all the solutions of the NL model, while the red and green curves correspond to the cases related to the laser source being swept from the short wavelength to long wavelength or vice versa respectively.

The amount of spectral distortion in the ring, as shown in figure 3.1 (b), is determined by the density of free-carriers accumulated in the conduction and valence band, and also by the temperature increase, which is proportional to the thermal impedance of the ring for the same amount of absorbed power. Here the resonant wavelength of the MRR is shifted due to self-heating being dominating over FCD,

and at the same time the quality factor decreases due to NL losses. The sharp increase in the transmission around $0.2\,nm$ is a consequence of the ring entering in the bistability region [122, 123] which is characterised by an hysteresis dependent on the type of wavelength sweep performed, i.e., forward (from low to high wavelength) or reverse sweep as indicated by the curves in red and green respectively.
In the particular case of a pump-probe experiment where two optical input of different wavelength are present, the absorption of one pump photon and one probe photon causes additional effective losses named cross two photon absorption (XTPA) or non-degenerate TPA (XTPA) [59, 130]. Similarly the probe/pump fields induce reciprocal phase variations through the Kerr effect, i.e., cross-phase-modulation (XPM) [124, 130], although its impact is appreciable only in amorphous silicon (a-Si) [124, 129].

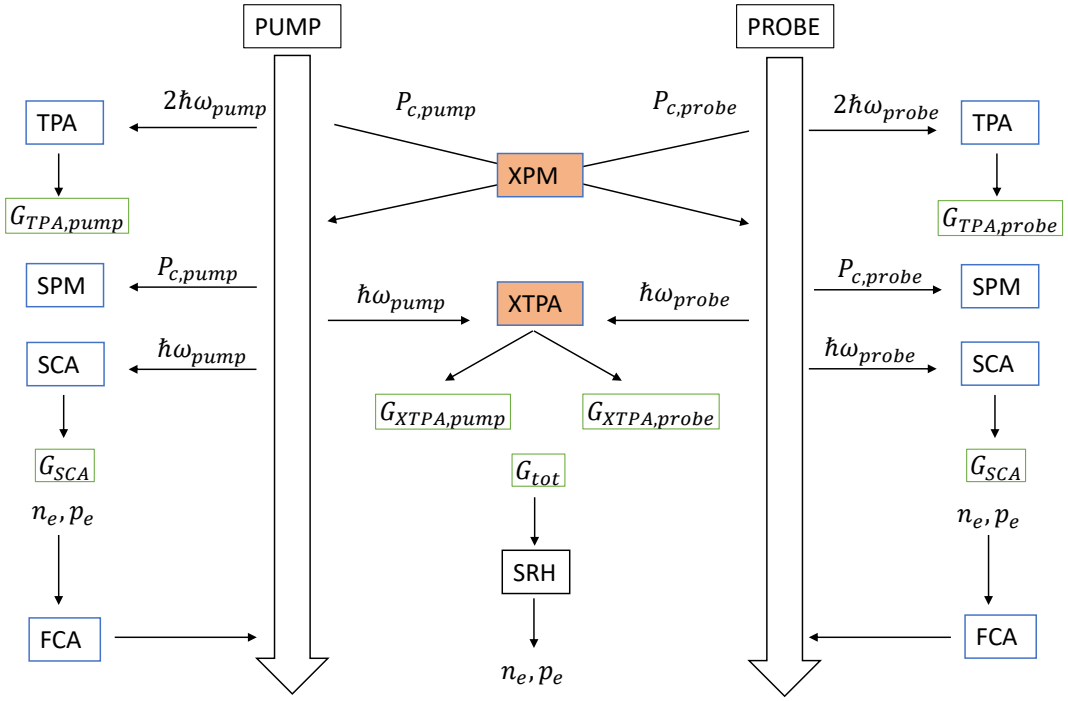

Fig. 3.2 Schematic of all NL effects acting on the pump and probe field.

In the next section we present the details of the NL model we developed that includes the previously introduced effects in a generic MRR. We also propose a new method for the modelling of all types of waveguide geometries based on the fitting

of optical and thermal parameters extracted from COMSOL simulation. Lastly we extend our lumped steady state model to the time domain.

3.2 Static analysis and SRH model for carrier recombination

3.2.1 Phase variation

The total phase variation in eq. (2.6) is modified by nonlinear effects, self-heating and Kerr effect as accounted in the term $\Delta\theta(Pc,\Delta T)$. As a result now the phase depends on the circulating power, temperature, and free carrier densities n_e and p_e:

$$\theta(P_c,T,n_e,p_e) = \theta_0 + \frac{n_g}{c}(\omega-\omega_0)L + \Delta\theta(P_c,T,n_e,p_e). \tag{3.1}$$

Where the nonlinear term is related to the refractive index variation $\Delta n_{eff}(P_c,T,n_e,p_e)$ as $\Delta\theta = 2\pi L/\lambda_0 \cdot \Delta n_{eff}$.

3.2.2 Propagation losses

The modal loss of the optical field per round trip now includes the total loss in the ring waveguide due to linear, and non-linear effects. These effective losses are expressed as:

$$\alpha_{eff}(P_c,n_e,p_e) = \alpha_0 + \alpha_{rad} + \Delta\alpha(P_c,n_e,p_e). \tag{3.2}$$

With

$$\Delta\alpha(P_c,n_e,p_e) = \alpha_{TPA}(P_c) + \Delta\alpha_{FCA}(n_e,p_e). \tag{3.3}$$

$\alpha_{TPA}(P_c)$ is the modal loss caused by two-photon absorption, which depends on the power propagating in the ring and it is expressed as [117]:

$$\alpha_{TPA}(Pc) = \frac{\beta_{TPA}}{A_{eff}}P_c, \tag{3.4}$$

which scales linearly with the circulating power; proof for this equation is shown in Appendix A. $\beta_{TPA} = 0.8\,cm/GW$ is the TPA absorption coefficient in C-band [41, 60, 127, 131]. The modal free-carrier-absorption losses α_{FC} are expressed as

a function of the free electron and hole densities through the empirical expression reported in [38]:

$$\Delta\alpha_{FCA}(n_e, p_e) = \Gamma\big(8.88 \cdot 10^{-21} n_e^{1.167} + 5.84 \cdot 10^{-20} p_e^{1.109}\big). \tag{3.5}$$

Where the coefficients above are for C-band, while n_e and p_e are expressed in $[cm^{-3}]$.

3.2.3 Refractive index variation

We neglect in our model the variation of silicon refractive index due to TPA because it is negligible compared to the contribution due to FCA and temperature [56]. The effective refractive index is the sum of contributions due to generated free-carriers, temperature and SPM, namely:

$$\Delta n_{eff} = \Delta n_{eff,FCD} + \Delta n_{eff,T} + \Delta n_{eff,Kerr}. \tag{3.6}$$

The FCD effect, $\Delta n_{eff,FCD}$, is again modelled with an empirical relation in C-band [38]:

$$\Delta n_{eff,FCD} = -\Gamma(5.4 \cdot 10^{-22} n_e^{1.011} + 1.53 \cdot 10^{-18} p_e^{0.838}) \tag{3.7}$$

Thermal dispersion

For what regards thermal dispersion due to self-heating, its derivation is similar to [41, 56, 126]. The power dissipated by the ring, P_d, is expressed as $P_d = P_{rad} + P_{abs}$, where P_{rad} represents the light lost and radiated in the cladding, and P_{abs} the absorption contribution which is converted into heat. The radiated power can be written as :

$$P_{rad} = \eta^2 \cdot (P_{bus} + P_c \cdot (a + a^2 \cdot t^2)) + P_c(1 - a_{rad})(1 + t^2 \cdot a). \tag{3.8}$$

The first term at the right hand side of eq. (3.8) is associated to the power lost at the coupler whereas the second term is power lost due to ring bend and therefore radiated in the cladding with $a_{rad} = e^{-\alpha_{rad} \cdot L/2}$. The power absorbed in the core, P_{abs} is due to TPA, FCA and also waveguide loss α_0 [41, 56, 126, 132] and can be written as:

$$P_{abs} = P_c(1 - a_{abs})(1 + t^2 \cdot a), \tag{3.9}$$

with $a_{abs} = e^{-(\alpha_0+\Delta\alpha(P_c))\cdot L/2}$. The demonstrations of equations (3.8) and (3.9) are included in Appendix A. Finally the absorbed power is converted into heat changing the effective refractive index of silicon through the relation:

$$\Delta n_{eff,T} = \Gamma \frac{dn_{Si}}{dT} Z_T P_{abs}. \tag{3.10}$$

$\frac{dn_{Si}}{dT} = 1.86 \cdot 10^{-4} K^{-1}$ is the silicon thermo-optic coefficient [41], while Z_T, the thermal impedance of the ring, is obtained from thermal simulation.

Kerr effect

The Kerr effect is modelled as a variation on the effective refractive index called self phase modulation (SPM):

$$\Delta n_{eff,Kerr} = \Gamma n_2 \frac{P_c}{A_{eff}}, \tag{3.11}$$

where $n_2 = 4.4 \cdot 10^{-18} [m^2/W]$[60, 124] is the Kerr coefficient in silicon.
It is important to highlight that TPA and SPM can be considered as instantaneous processes when compared to FC recombination and diffusion in silicon. The time scale of this type of transition can be computed with the uncertainty principle as $|\omega - E_g/\hbar|^{-1}$ [59, 133]. With $E_g = 1.12\,eV$ in the C-band we get response times around $2-10\,fs$ which are completely negligible when compared with FC lifetimes always larger than $100\,ps$ as measured in our experiments.

3.2.4 SRH model

It is clear from eq. (3.5) and (3.7) that the free carrier density plays a fundamental role in defining NL effects in silicon. In literature, rate-equations based on recombination rate such as $\frac{N}{\tau}$ are often employed, where N is the free carrier density and τ a generic lifetime for the recombination process. This recombination model implicitly assumes that electron and hole FC densities are equal (i.e., $n_e = p_e = N$) and that the carrier lifetime is a constant value independent on the carrier density and thus on the pumping power. This assumption is not true for the silicon waveguide case; in [134] experimental measurement on Si straight waveguides showed that the FC

dynamics is rather non-linear and dependent on the optical power in the waveguide. In the same work, the authors demonstrated that the non-linear carrier dynamics can be well explained in the frame of the rigorous SRH recombination theory [135]. The findings in [134] can also justify why in previous works on non-linear ring resonators [55, 41, 56] it was necessary to assume an empirical carrier lifetime depending on circulating power to explain measured results.

In order to reliably model different ring resonators without having to rely on the previous assumptions, we derive the free carrier densities through SRH recombination [58] where traps act as recombination/trapping centers (trap-assisted recombination) upon the capture/trapping of a hole and an electron.

We indicate with E_t the trap energy level inside the energy band gap, and with N_f the bulk trap density per unit of volume in the silicon waveguide. The latter can be linked to the density of surface traps N_s, referred to waveguide side-walls imperfection, through the expression[134]:

$$N_f = N_s \cdot \frac{2(W+h)}{W \cdot h}, \tag{3.12}$$

which implies that the surface defects are equally distributed all over the surface of the silicon core in contact with SiO_2.

In this contest, defining a total carrier generation rate G, the rates of variation of excess electron (n_e) and hole (p_e) densities in the MRR are [135]:

$$\begin{aligned} \frac{\partial n_e}{\partial t} &= G - \frac{1}{\tau_{n0}} \left(\frac{(n_0+n_1+n_e)(n_e-p_e)}{N_f} - \frac{n_e n_1}{n_e+n_o} \right) \\ \frac{\partial p_e}{\partial t} &= G - \frac{1}{\tau_{p0}} \left(\frac{(p_0+p_1+p_e)(p_e-n_e)}{N_f} - \frac{p_e p_1}{p_e+p_o} \right) \end{aligned} \tag{3.13}$$

The right hand side in eq. (3.13) are the recombination rate for electrons (R_e) and holes (R_h) with $\tau_{n0} = (N_f \sigma_n v_n)^{-1}$,$\tau_{p0} = (N_f \sigma_p v_p)^{-1}$ representing the shortest capture time of carriers in the trap when it is not occupied by electrons and holes. $\sigma_{n,p}$ is the capture cross section, and $v_{n,p}$ the thermal velocity of electrons and holes equal to $2.3 \cdot 10^{15}\, m/s$ and $1.65 \cdot 10^{15}\, m/s$ respectively [136]. We note here that the different capture cross section and thermal velocity of electrons and holes cause a different capture rate in the traps that eventually unbalance electron and hole densities. Thus the assumption that $n_e = p_e = N$ fails. We also see that in eq. (3.13) it is rather difficult to identify a unique carrier lifetime τ; as discussed in the following we can only define equivalent carrier lifetimes once the rate equations in

(3.13) are solved and the carrier densities obtained.
n_0 and p_0 are electron and hole concentration in the absence of traps at equilibrium; $n_1 = n_0 e^{(E_t-\psi_f)/k_bT}$ and $p_1 = p_0 e^{(\psi_f-E_t)/k_bT}$ depend on the difference between the Fermi energy level, ψ_f, of the silicon bulk (with a possible residual doping level) and E_t.
In steady state ($\frac{\partial n_e}{\partial t} = \frac{\partial p_e}{\partial t} = 0$) any thermal or carrier transient is concluded [134] and eq. (3.13) reduces to two polynomial equations with unknowns n_e and p_e. Through a normalisation with respect to p_0 [135] and defining the normalised electrons and holes carrier densities $y = p_e/p_0$, $x = n_e/p_0$, the equation for holes yields:

$$\begin{aligned} &y^3 + y^2\left[(2+b+ab) + N_e b/(1+b) - G_e(1+\gamma^{-1})\right] + \dots \\ &y[(1+b)(1+ab) + N_e b/(1+b) - G_e/\gamma(1+b)(1+a+2/\gamma) - \dots \\ &-N_e G_e(1+2b)/\gamma(1+b)] - G_e\left[(1+b)^2(1+a/\gamma) - N_e(G_e-\gamma)/\gamma^2\right] = 0. \end{aligned} \tag{3.14}$$

Whereas for electrons:

$$\begin{aligned} &x^3 + x^2\left[(1+a+2ab) + N_e/(1+b) - G_e(1+\gamma^{-1})\right] + \dots \\ &x[a(1+b)(1+ab) + N_e ab/(1+b) - G_e(1+b)(1+a+2a/\gamma) - \dots \\ &-N_e G_e(2+b)/(1+b)] - G_e\left[a(1+b)^2(1+a/\gamma) - N_e(G_e-ab)\right] = 0. \end{aligned} \tag{3.15}$$

In both eq. (3.15) and (3.14): $a = n_1/p_0$, $b = p_1/p_0$, $G_e = G\frac{\tau_{n0}}{p_0}$, $N_e = N_f/p_0$, and $\gamma = \tau_{n0}/\tau_{p0}$ are all normalised parameters with respect to the hole carrier density at equilibrium.
Considering the hole equation, it can be solved through the search of all trigonometric solutions of a depressed cubic equation with eq. (3.14) expressed in the form $a_y y^3 + b_y y^2 + c_y y + d_y = 0$. The solutions y_k with $k = 0,1,2$, are then uniquely associated to the excess electron density x_k through the expression:

$$x_k = y_k - \frac{N_e}{\gamma\cdot(y_k+1+b)}\left(G_e - \frac{\gamma b y_k}{1+b}\right), \tag{3.16}$$

which has been obtained from the hole rate equation in (3.13) in steady state. Among the different solutions, only $k = 0$ provides a physically sound solution since it guarantees that the excess electron and hole densities satisfy the condition:

$$0 < (p_{k,e} - n_{k,e})/N_f < 1, \tag{3.17}$$

that represents the fraction of occupied traps when we consider donor like trap that suppose the electron capture cross section to be larger than the hole ones as proved experimentally around the midgap [55]. For this reason, from now the index k is dropped as it is always equal to 0.
As a consequence of the different capture cross sections, the electron and hole capture times, τ_{n0} and τ_{p0}, are different [55] resulting in an unbalance between electron and hole densities. For any normalized generation rate G_e, we may write an equivalent electron and hole lifetime defined as $\tau_n = n_e/G_e$ and $\tau_p = p_e/G_e$. With this method, the hole carrier lifetime can be explicitly written as:

$$\begin{aligned}
\tau_p &= \frac{\tau_{n0}}{G_e}\left\{2\sqrt{-\frac{p}{3}}cos\left[\frac{1}{3}\arccos\left(\frac{3q}{2p}\sqrt{-\frac{p}{3}}\right)-2\pi k/3\right]-\frac{b_y}{3a_y}\right\} \\
p &= \frac{3a_yc_y-b_y^2}{3a_y^2} \\
q &= \frac{2b_y^3-9a_yb_yc_y+27a_y^2}{27a_y^3}
\end{aligned} \tag{3.18}$$

and a similar expression is obtained for electron lifetime.
In the case of very high input power, such that we assume $G_e \to \infty$, we get:

$$\tau_{e,\infty} = \tau_{p,\infty} = \tau_\infty = \tau_{n0}(1+\gamma^{-1}) \tag{3.19}$$

Calculation of the total generation rate G

SRH rate equation are clearly dependent on the carrier generation rate G. In steady state it is the result of SCA (G_{SCA}) [100, 128] and TPA induced carrier generation, namely:

$$G = \frac{\alpha_0\eta_{SCA}P_c}{\hbar\omega_0 AA_{eff}} + \frac{\alpha_{TPA}P_c}{2\hbar\omega_0 A}. \tag{3.20}$$

η_{SCA} is the SCA efficiency which indicates what fraction of the total linear loss α_0 contributes to the defect assisted single photon absorption (SPA) intra-gap states where we have additional photon absorption; it is usually $\eta_{SCA} < 0.1$. The total SRH generation rate is then the sum of free carriers generated by SCA [100, 128, 129] and those from TPA. The factor 2 in the TPA generation rate is due to the absorption of two photons, whereas SCA generation rate is associated with only one.
Inserting G in eq. (3.15) and (3.14) the excess electron and hole carrier densities n_e

and p_e can be computed for any given P_c. This allows the computation of α_{eff} and NL phase variation $\Delta\theta$ as a function of P_{bus} and P_c. We highlight that now eq. (2.5) is a complex non-linear equation with unknown P_c:

$$P_c = P_{bus}\frac{\kappa^2(1-\eta^2)}{\left|1-t^2a(P_c)e^{j\theta(P_c)}\right|^2} \tag{3.21}$$

This equation can be solved numerically in steady state to get the circulating power for a fixed bus power at any input wavelength λ. From the circulating power, we then get the effective loss and the transmission coefficient at the through port self-consistency as summarised in figure 3.3. When bistability occurs, the non-linear equation can have up to three distinct possible solutions [126] as shown in figure3.1 (b). Experimentally only two cases are observable: one that corresponds to the stable state obtained by increasing the injected wavelength with respect to a previous stable state (i.e., wavelength sweep from blue to red), whereas the other solution is found with the opposite wavelength sweep (i.e., from red to blue) [56, 117, 126].

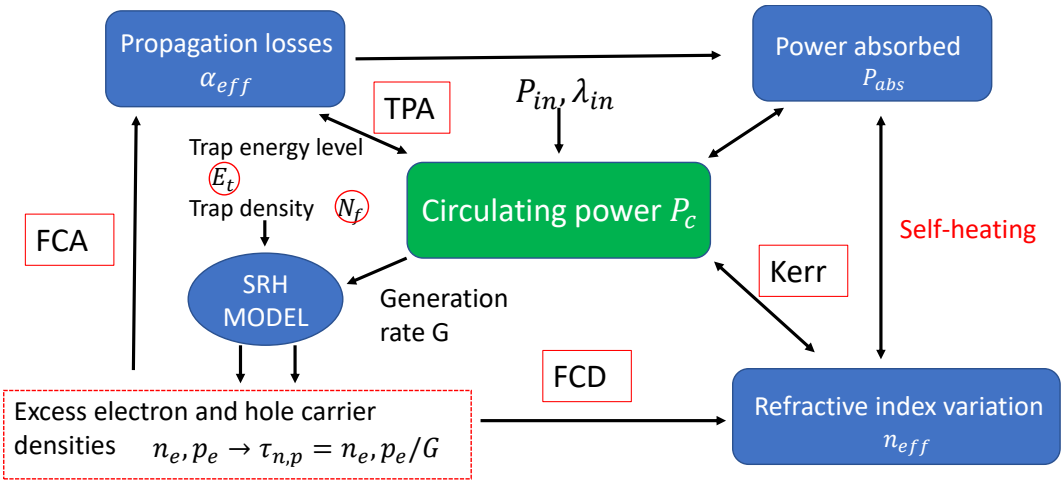

Fig. 3.3 Summary of the developed self-consistent model for NL effects in silicon MRRs including SRH recombination to estimate excess electrons and holes densities. The trap energy level and density are highlighted as the model fitting parameters.

3.3 Distributed steady state formulation

As we will show in the experimental section, the previous model is rather good in predicting NL effects in MRR with strip waveguides where diffusion of FC is

negligible. For rib or more complex waveguides geometries, FC tend to diffuse in the device [137], see Fig. 3.4 (a), causing quantities such as the ring thermal impedance Z_T, FCD, and FCA to be calculated with 2D simulations.

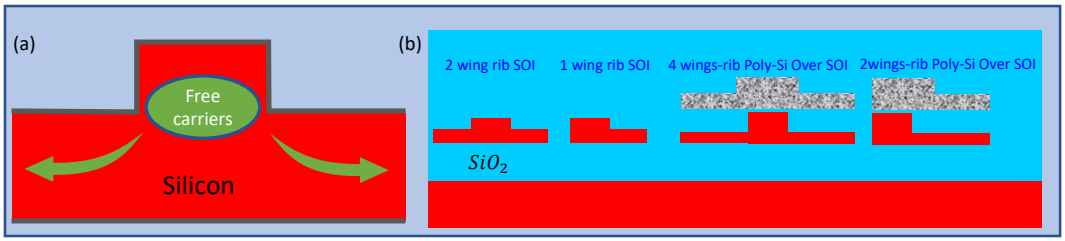

Fig. 3.4 (a) Sketch of diffusion process in a rib waveguides: free carriers, generated in the middle of the waveguide, spread as a result of diffusion. (b) Different geometries waveguides for MRRs including also composite waveguides with silicon and polysilicon ribs.

In this section we demonstrate that, by simulating with COMSOL the MRR, we can extract the impact of NL effects in the MRR as a function of the circulating power for any given geometry such as those shown in Fig. 3.4 (b).
To do so we import the electromagnetic field distribution in the ring cross section simulated with RSOFT in COMSOL multyphisics semiconductor tool where a drift-diffusion model is coupled with the thermodynamic model, eq. (2.23). The total set of coupled equations are summarised below [138]:

$$\nabla(\varepsilon_0\varepsilon_r\nabla\phi(r,t)) = -q(p_e(r,t) - n_e(r,t) + N_d - N_a), \tag{3.22}$$

$$\frac{\partial p_e(r,t)}{\partial t} = \nabla(J_p(r,t)) - (G_{cell}(r,t) - R_p(r,t)), \tag{3.23}$$

$$\frac{\partial n_e(r,t)}{\partial t} = -\nabla(J_n(r,t)) - (G_{cell}(r,t) - R_n(r,t)), \tag{3.24}$$

$$J_p(r,t) = \sigma_{e,p}(r,t)\nabla\phi(r,t) + D_p\nabla p_e(r,t), \tag{3.25}$$

$$J_n(r,t) = \sigma_{e,n}(r,t)\nabla\phi(r,t) - D_n\nabla n_e(r,t). \tag{3.26}$$

Where: $\sigma_{e,n}(r,t) = q \cdot n_e(r,t)\mu_n$, $\sigma_{e,p}(r,t) = q \cdot p_e(r,t)\mu_p$. ϕ is the potential caused by FC accumulation, and $G_{cell}(r,t)$ the local generation rate.
We remind that simulations are performed in the 2D-axisymettric approximation (see chapter 2.4.1), therefore $n_e(x,y,z,t), p_e(x,y,z,t)$, and $\phi(x,y,z,t)$ are constant over the z direction. For this reason we focus the analysis only on the cross section

of the ring and at steady state, i.e., $n_e(x,y), p_e(x,y)$ $\phi(x,y)$. For this preliminary study we neglect the Kerr and SCA effect whose strength is always lower than FCD, self-heating and FCA.

Generation rate

In order to compute the generation rate for each cell of the mesh of volume $V_{si} = dxdydz$ we first consider the Maxwell equations:

$$\nabla x \boldsymbol{E}(r,t) = -\frac{\partial \boldsymbol{B}(r,t)}{\partial t} \tag{3.27}$$

$$\nabla x \boldsymbol{H}(r,t) = \frac{\partial \boldsymbol{D}(r,t)}{\partial t} \tag{3.28}$$

where $\boldsymbol{B}(r,t) = \mu_0 \boldsymbol{H}(r,t)$ and the electrical displacement $\boldsymbol{D}(r,t) = \varepsilon_0 n_{si}^2 \boldsymbol{E}(r,t) + \boldsymbol{Pl}^{(nl)}(r,t)$. Here $\boldsymbol{Pl}^{(nl)}(r,t)$ is the local polarization in the material caused by third-order nonlinear susceptibility tensor $\boldsymbol{\chi}^{(3)}$. By approximating the latter as a scalar quantity, $\boldsymbol{Pl}^{(nl)}(r,t)$ becomes [117, 139]:

$$Pl^{(nl)}(x,y,\omega) = \frac{3\omega\varepsilon_0}{4}(\chi^{(3)})E_\mu |E_\mu|^2 E_\mu \tag{3.29}$$

With $E_\mu = E_\mu(x,y)$ as defined in eq. (2.15). We remind that $\chi^{(3)}$ is generally complex i.e., $\chi^{(3)} = \chi_R^{(3)} - j\chi_{Im}^{(3)}$. By performing the difference between eq. (3.27) and (3.28) and following the same approximations done in [117], at steady state when $\frac{\partial E_\mu}{\partial t} = \frac{\partial H_\mu}{\partial t} = 0$ we have:

$$\frac{\partial I_{opt}/A_\mu^*}{\partial z} = -j|A_\mu(z)|^2 A_\mu(z) Pl^{(nl)} E_\mu^*/4P_{n,\mu}^2 \tag{3.30}$$

Where the optical power per unit area I_{opt} is:

$$I_{opt}(x,y,\omega,z) = A_\mu(z)\cdot A_\mu^*(z)\frac{(E_\mu \times H_\mu^* + E_\mu^* \times H_\mu)\cdot \hat{z}}{4P_{n,\mu}} \tag{3.31}$$

where $P_{n,\mu}$ has been defined in eq. (2.17). The power flowing in a given cell of cross section dx and dy and with section of length dz, is then $P(x,y,z) = I_{opt}dxdy$; the power loss is $\Delta P(x,y,z) = P(x,y,z) - P(x,y,z+dz)$. Thus we multiply eq. (3.30) by

$A^*_\mu dxdy$ and using the transformation $dz = v_g dt$, after some calculations we get to:

$$\frac{\partial \Delta P(x,y,z,t)}{\partial t} = -2v_g |A_\mu(z,t)|^4 \gamma_L \tag{3.32}$$

Where we used the property $\frac{(\partial A_\mu \cdot A^*_\mu)}{\partial z} = A_\mu \cdot \frac{\partial A^*_\mu}{\partial z} + A^*_\mu \cdot \frac{\partial A_\mu}{\partial z}$, γ_L is the local absorption rate to the power $[\frac{1}{W \cdot m}]$ defined as:

$$\gamma_L(x,y,\omega) = \frac{3\omega\varepsilon_0 |E_\mu(x,y,\omega)|^4 \chi^{(3)}_{Im} dxdy}{16 P^2_{n,\mu}} \tag{3.33}$$

Since we want to derive an expression for the photons loss associated to free carrier generation due to TPA, eq. (3.32) must be real; therefore we consider the imaginary part of $\chi^{(3)}$ as written in eq.(3.33) . In order to get the generation rate in the cell $dxdy$, we first consider the number of photons $S_{tot}(x,y,z,t)$ related to the power $P(x,y,z,t)$ in a given cell, namely:

$$S_{tot}(x,y,z,t) = \frac{P(x,y,z,t)}{dz} v_g \hbar\omega \tag{3.34}$$

We perform the derivative with respect to time of S_{tot} and substitute eq. 3.32 reminding that the quantity $\frac{1}{2}\frac{\partial S_{tot}}{\partial t}$ represents the number of photons absorbed due to TPA, which ultimately results in free carriers generation. The total number of carriers $N_{tot,cell}$ in a cell with volume $V_{si} = dxdydz$ must then satisfy a rate equation with G_{cell} the generation rate in a cell which is equal to

$$G_{cell}(x,y,z,\omega) = \frac{P_c(z)^2 \beta_{TPA} n^2_{si} |E_\mu(x,y,\omega)|^4}{\hbar\omega 8 Z_0^2 P^2_{n,\mu}}. \tag{3.35}$$

With $\chi^{(3)}_{Im} = \frac{2n^2\beta_{TPA}}{3k_0 Z_0}$ [117] and $P_c(z,t) = |A_\mu(z,t)|^2$. Eq. (3.35) represents the local generation rate in our model, it can be seen that the integral of G_{cell} over the whole area of a rectangular waveguide coincides with the lumped expression of the generation rate, i.e., $G_{tot} = \frac{1}{A}\int G_{cell} dxdy = \frac{\beta_{TPA} P_c^2}{2\hbar\omega A A_{eff}}$. We highlight that this generation profile directly follows the electric field distribution in the waveguide without the need of relaying on A_{eff} and the waveguide area A whose definitions become ambiguous in more complex structures such as rib waveguides.

Distributed FCD and FCA

By inserting eq. (3.35) in the SRH rate equations, eqs. (3.13), at steady state we compute $n_e(x,y)$ and $p_e(x,y)$ over the ring cross section. These FC influence the silicon refractive index through FCD and self-heating as in the lumped model. We defined the local variation of losses and refractive index due to FC as $\Delta\alpha_{FCA,D}(x,y)$ and $\Delta n_{eff,FCD,D}(x,y)$. respectively. To calculate the variation of the complex propagation constant of the waveguide, we start from the complex relative dielectric constant $\Delta\varepsilon = \Delta\varepsilon_r + j\Delta\varepsilon_i$ in the medium. The variation of propagation constant of the guided mode [140, 141] is:

$$\Delta\beta_{r,i} = \frac{\omega_0 \int\int_\infty \Delta\varepsilon_{r,i}(x,y)\cdot E_\mu(x,y,\omega_0)^* E_\mu(x,y,\omega_0)dxdy}{4P_{n,\mu}} \tag{3.36}$$

By definition all quantities in eq. (3.36) except for $\Delta\varepsilon_{r,i}(x,y)$ refer to the unperturbed model where the NL effects caused by TPA, FCA and FCD are considered as perturbation.
The variation of the complex dielectric constant caused by FCD and FCA is:

$$\Delta\varepsilon_{r,i}(x,y) = \varepsilon_0\left[\left(n_{Si} + \Delta n_{FCD,D}(x,y) + j\Delta\alpha_{FC,D}(x,y)\lambda/4\pi\right)^2 - n_{si}^2\right] \tag{3.37}$$

Since we threat the NL effects as perturbation of n_{Si}, it is possible to approximate $\Delta\varepsilon_r$ and $j\Delta\varepsilon_i$ as:

$$\begin{aligned}\Delta\varepsilon_r(x,y) &\approx 2\varepsilon_0 n_{si}\Delta n_{FCD,D}(x,y)\\ \Delta\varepsilon_i(x,y) &\approx 2\varepsilon_0 n_{si}\Delta\alpha_{FC,D}(x,y)\lambda/4\pi\end{aligned} \tag{3.38}$$

Finally by inserting eq. (3.38) in eq. (3.36) we get, for any given P_c, the total $\Delta\beta_{r,i}$. The effective refractive index variation is:

$$\Delta n_{eff,FCD}(P_c) = \frac{\lambda}{2\pi}\Delta\beta_r(P_c), \tag{3.39}$$

and the modal loss:

$$\Delta\alpha_{FC}(P_c) = 2\cdot\Delta\beta_i(P_c). \tag{3.40}$$

Which are completely equivalent to eq. (3.5) and (3.7) for rectangular waveguide geometries or more generally in all cases when $\Delta n_{FCD,D}(x,y)$ and $\alpha_{FC,D}(x,y)$ are constant over the entire waveguide cross section.

Distributed self-heating

What is still missing in the previous formulation is the effect of temperature in the MRR, we no longer assume the heat source to be uniformly distributed in the silicon strip cross-section as done in eq. (2.24), since we expect the diffused FCs to contribute differently to self-heating depending on where, over the ring cross section, the carriers recombine. The total heat source is [142, 143]:

$$Q = q_J + q_{FCA} + q_{SRH}, \tag{3.41}$$

where $q_J(x,y) = \frac{|J_n(x,y)|^2}{\sigma_{e,n}(x,y)} + \frac{|J_p(x,y)|^2}{\sigma_{e,p}(x,y)}$ is the Joule effect related to the current densities J_n and J_p, $q_{FCA}(x,y) = \alpha_{FC,D}(x,y) I_{opt}(x,y)$ is the thermalisation of free carriers, and $q_{SRH}(x,y) = R_e(x,y) \cdot (2\hbar\omega_0 - E_t) + R_p(x,y) \cdot (E_t - E_v)$ the SRH heat originating from relaxation of TPA induced FCs to the trap states (with energies E_t) from the conduction (E_c) and to the valence band (E_v). The factor $2\hbar\omega_0$ is a consequence of TPA, in other words the energy of FC is slightly larger than the bandgap E_g, in fact it holds that $E_{2\hbar\omega_0} = 1.59\,eV > E_{g,si}$ as it is possible to see in the sketch in figure 3.1. Performing the thermal simulation we get the temperature profile $\Delta T(x,y)$ whose local impact on the refractive index is computed as $\Delta n_{T,D}(x,y) = \frac{dn_{Si}}{dT} \Delta T(x,y)$. By following the same procedure explained earlier for FCD and FCA, first we compute the local variation of the real permittivity:

$$\Delta\varepsilon_{r,T}(x,y) \approx 2\varepsilon_0 n_{si} \Delta n_{T,D}(x,y). \tag{3.42}$$

By substituting the latter in eq. (3.36), the effective refractive index variation as a function of the circulating power P_c and due to self-heating is:

$$\Delta n_{eff,T}(P_c) = \frac{\lambda}{2\pi} \Delta\beta_{r,T}(P_c) \tag{3.43}$$

Finally we can calculate equations (3.40), (3.39), and (3.43) from the 2D simulations as a function of P_c and fit the curves obtained with a polynomial, we then insert these relations in the lumped model as a replacement of equations (3.5), (3.7), and (3.10) respectively. An example will be given in the next section

Model validation

To validate our distributed model we consider the waveguide and ring structure of [6] where the authors performed steady state measurements on a multimode ring resonator of radius $r = 100\,\mu m$ and made of a rib waveguide as shown in figure 3.5 (a). We extracted the linear regime parameters, summarised in table 3.1, from the fitting of the ring transmission at $P_{bus} = -16.5\,dBm$ reported in [6] where the fundamental mode was considered.

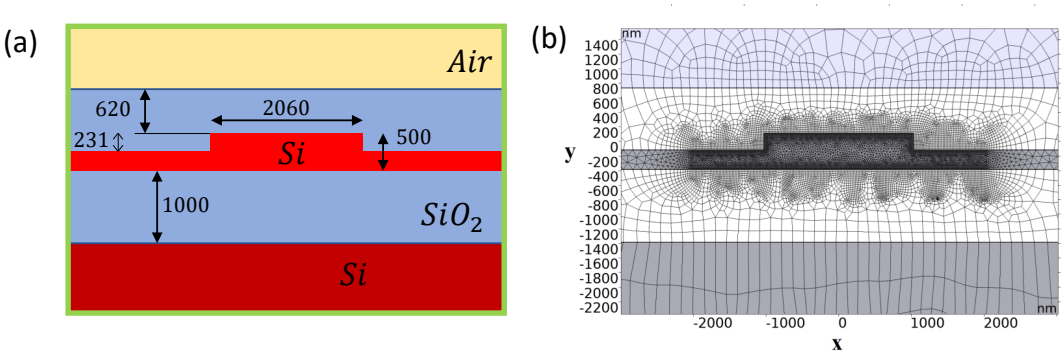

Fig. 3.5 (a) Dimensions (in *nm*) of the rib waveguide structure from [6]. (b) Non-uniform mesh built in COMSOL for the simulation of the ring.

Table 3.1 Parameters of the silicon MRR analysed in [6] with radius $r = 100\,\mu m$. The waveguide geometries labels are defined in fig. 3.8 (c).

Parameter	Value	Unit
L	628	μm
W_1	2.06	μm
h_1	500	nm
h_2	269	nm
κ^2	0.0038	–
η^2	0	–
α_0	0.38	dB/cm
n_g	3.74	–
α_{rad}	0	dB/cm
$n_{eff,0}$	3.25	–
β_{TPA}	0.5	cm/GW

By importing the electromagnetic field distribution in MATLAB coupled with COMSOL, we are able to define $G_{cell}(x,y)$ in COMSOL over all the waveguide cross section as shown in figure 3.6 (a). Here we used a non-linear mesh with higher

density near the core of the rib, see figure 3.6 (b). Figures 3.6 (b) and (c) show

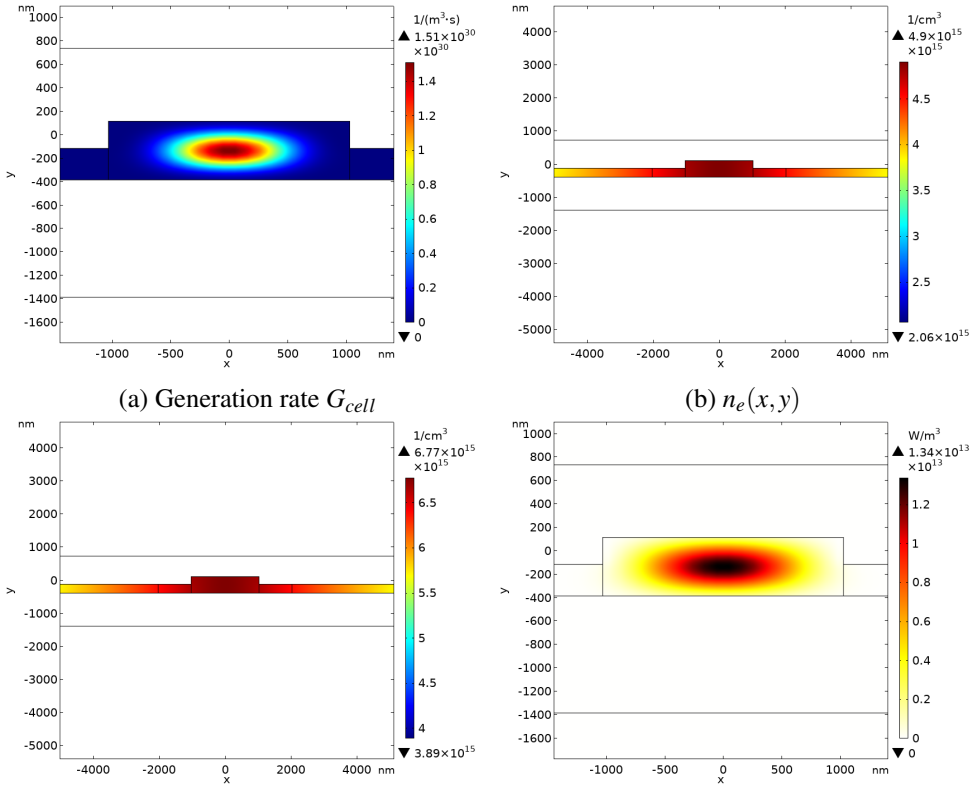

(a) Generation rate G_{cell}

(b) $n_e(x,y)$

(c) $p_e(x,y)$

(d) Heat source Q_{tot}

Fig. 3.6 (a) Generation rate G_{cell} in the rib waveguide considered in [6]. (b) and (c) are the electrons and holes FC solutions of the drift-diffusion model in COMSOL. (d) Heat source in the rib waveguide as defined in eq. (3.41). In all cases the circulating power was fixed at $P_c = 100\,mW$ with a trap density $N_f = 2 \cdot 10^{15}\,cm^{-3}$.

the simulation result assuming a circulating power in the ring of $100\,mW$ and a trap denisty for the SRH model equal to $N_f = 2 \cdot 10^{15}\,cm^{-3}$. We note how carriers diffuse towards the wings, proving that this type of waveguide cannot be treated with a lumped model, rather a distributed model is needed. In figure 3.6 (c) the heat source, eq. (3.41), is shown as well. It is clear that it follows the generation rate since q_{FCA} is order of magnitudes larger than q_j and q_{SRH} whose impact is therefore completely negligible. An uniform trap density distribution N_f was then used as a fitting parameter to reproduce the resonant wavelength shift and variation of transmission at resonance as measured in [6] whereas the trap energy fixed around the midgap, i.e., $E_t = 0.63\,eV$. Figures 3.7 (a), (b) and (c) show the relations between $n_{eff,FCD}$, $n_{eff,T}$, and α_{FC} and the circulating power. These quantities have been

obtained by using the previously introduced method, eqs. (3.39), (3.43), and (3.40) respectively, for three different trap densities.

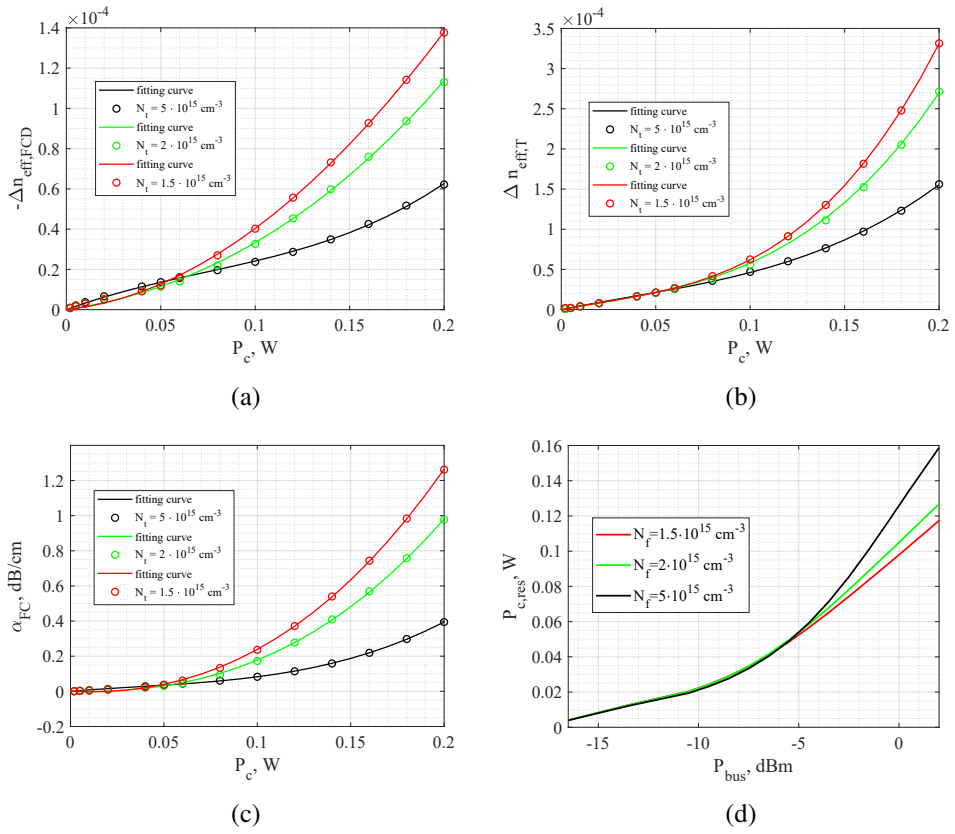

Fig. 3.7 (a) Refractive index variation due to FCD and (b) self-heating, and (c)free carriers losses versus circulating power in the ring for different trap densities. (d) Self-consistent circulating power obtained with the lumped model at steady state versus bus power for different trap densities using the expressions in (a), (b), and (c).

We can then include in the previously developed lumped model all the information about the impact of NL effects in the ring by fitting the refractive index variation due to FCD, self-heating and NL losses with ad-hoc polynomial expression of the type $y(P_c) = a_3P_c^3 + a_2P_c^2 + a_1P_c$. For example in the case $N_f = 2 \cdot 10^{15}\,cm^{-3}$ we have:

$$\begin{aligned}
&\alpha_{FC}(P_c) = 12.3P_c^3 + 3.5P_c^2 - 0.12P_c;\\
&\Delta n_{eff,FCD}(P_c) = -(1.9 \cdot 10^{-3}P_c^3 + 1.7 \cdot 10^{-3}P_c^2 + 1.3 \cdot 10^{-4}P_c);\\
&\Delta n_{eff,T}(P_c) = 3 \cdot 10^{-2}P_c^3 - 1.3 \cdot 10^{-3}P_c^2 + 4.1 \cdot 10^{-4}P_c.
\end{aligned} \tag{3.44}$$

Simulation results are shown in figure 3.8 (a) and (b) where we demonstrate that with our lumped model, fed with expressions taking into account carrier diffusion, we are able to follow well the shift of the resonant wavelength and qualitatively the transmission degradation at resonance due to NL effects. The low power spectrum form which we extracted the model parameters is shown in figure 3.8 (c), whereas the spectrum obtained with our model is superimposed to some of the curves (dashed black lines) extracted from [6] for the same input powers. We attribute the discrepancy between our results and the experiment at high bus power to self-oscillations in the ring causing the value of the transmission coefficient to oscillate in time as we will see also experimentally in chapter 4.4.
We also show that the trap density is a critical parameter in defining the FCs physics inside the MRR.

3.4 Time domain formulation

In the previous section, the equations regulating TPA, FCA, and thermal effects were investigated. In particular equations (3.4), (3.5), (3.7), and (3.10) are valid also in the case of an input power variable in time $P_{bus}(t)$; in this case the circulating power $P_c(t)$, $n_e(t)$, $p_e(t)$, and the temperature variation $\Delta T(t)$ are now time dependent as a consequence of free carrier recombination in time and thermal time constants [88]. In the following, we develop the general lumped time domain formulation in the case of a pump-probe experiment. In this case a pump pulse is injected: the probe can be either a CW signal or a another single pulse. Additional terms related to the interaction between probe and pump fields introduce further NL effects in the ring that play an important role during the pulse duration. The self-oscillation regime sometimes observed with CW input, represents a particular case of this model that will be discussed as well.

3.4.1 Pump-probe differential equations

Generally in a pump-probe experiment, whose results are shown in chapter 4.5, we have two input signals set at two different cold resonant wavelengths of the ring, $\lambda_{0,1}$ and $\lambda_{0,2}$ corresponding to the pump and probe field respectively. The high power

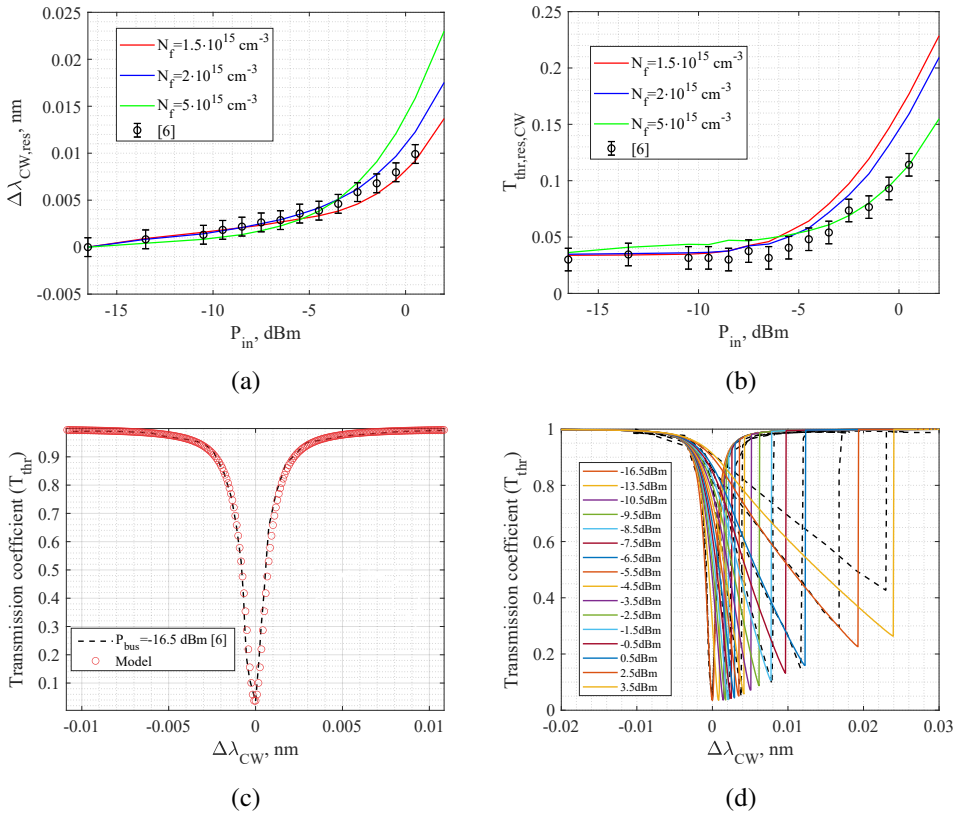

Fig. 3.8 (a) Resonant wavelength shift $\Delta\lambda_{CW}$ and variation of the transmission coefficient at resonance (b) as a function of the continuous wave input bus power before the ring P_{bus}, black markers represent data extracted from figure 2 (a) in [6]. (c) Low power transmission spectrum extracted from [6] fitted with ur model in linear regime. (d) Model spectrum superimposed to some of the curves (dashed black lines) extracted from the experimental spectrum in figure 2 (a) in [6], the legend is P_{bus} .

pump optical field excites NL effects resulting from strong free carriers generation, whereas the probe field is used to monitor the FC effects and get information on the ring dynamics. Therefore there are two circulating fields in the ring: $E_{ring,1}(t) = E_{c,1}(t) \cdot e^{(-j\cdot\omega_{0,1}t)}$, and $E_{ring,2}(t) = E_{c,2}(t) \cdot e^{(-j\cdot\omega_{0,2}t)}$. In both cases subscripts 1 and 2 refer to the pump and probe cold resonances respectively. The coupling coefficient κ (and the transmission coefficient as well t) and Γ may be different in the two cases since they are wavelength dependent; this is especially true in high FSR rings such as the Si/poly-Si one where $FSR \approx 40nm$. The differential equations of the fields inside the ring can be obtained through the inverse Fourier transform of eq. (2.5) by performing the Taylor expansion of $e^{j\cdot\theta_{1,2}}$ around the phase-variation per round trip

$\theta_{0_{1,2}}$, see eq. (2.6); since the reference pulsation $\omega_{0_{1,2}}$ corresponds to the cold ring resonance, we have that $e^{j\cdot\theta_{0_{1,2}}} = 1$. We then get the equations for $E_{c,1}(t)$:

$$\begin{aligned}\frac{\partial E_{c,1}}{\partial t} = -(\frac{\kappa_1\cdot\sqrt{1-\eta^2}}{t_1^2 a_1(t)}E_{bus,1} + E_{c,1}(t)(\frac{1}{t_1^2 a_1(t)} - 1) + \\ j\cdot(\frac{L}{c}\Delta\omega_{r,1}(t) + \tau_{g1}\delta\omega_1)\cdot E_{c,1}(t))/\tau_{g,1},\end{aligned} \tag{3.45}$$

and similarly for $E_{c,2}(t)$

$$\begin{aligned}\frac{\partial E_{c,2}}{\partial t} = -(\frac{\kappa_2\cdot\sqrt{1-\eta^2}}{t_2^2 a_2(t)}E_{bus,2} + E_{c,2}(t)(\frac{1}{t_2^2 a_2(t)} - 1) + \\ j\cdot(\frac{L}{c}\Delta\omega_{r,2}(t) + \tau_{g,2}\delta\omega_2)\cdot E_{c,2}(t))/\tau_{g,2}.\end{aligned} \tag{3.46}$$

With $P_{bus_{1,2}} = |E_{bus_{1,2}}|^2$,$P_{c_{1,2}} = |E_{c_{1,2}}|^2$, $\Delta\omega_{r_{1,2}} = \omega_{0_{1,2}}\cdot\Delta n_{eff_{1,2}}$, and $\tau_{g_{1,2}} = L\cdot n_{g_{1,2}}/c$. $\delta\omega_{1,2}$ is the pump and probe detuning with respect to the cold resonances. In our case it is $\delta\omega_1 \approx 0$ since the pump is tuned at the ring cold resonance to generate highest possible circulating field for carrier generation; whereas the probe can be detuned around $\lambda_{0,2}$. In eq. (3.45) and (3.46), the round trip loss $a_{1,2}$ and variation of resonance due to NL $\Delta\omega_{r_{1,2}}$ are now time dependent, because the carrier densities in eq. (3.13) and temperature vary with time. We note that, since Γ and A_{eff} can be different for the two resonances, we will have $\Delta\omega_{r,1} \neq \Delta\omega_{r,2}$.
The temperature dynamic can be written by using an approximated version the heat equation defined in eq. (2.23) [123, 126], by assuming that heat is uniform inside the waveguide, that is:

$$\frac{\partial\Delta T_i(t)}{\partial t} = -\frac{\Delta T_i(t)}{\tau_{th,i}} + \frac{P_{abs,1}(t) + P_{abs,2}(t)}{C_i}, \tag{3.47}$$

for pump and probe fields with $i = 0,1,2,3$ referring to the four nodes equivalent thermal circuit of the ring defined in the previous chapter.
Here $P_{abs_{1,2}}$ has the same expression of eq. (3.9). At steady state, i.e., $\frac{\partial\Delta T_i(t)}{\partial t} = 0$, eq. (3.47) reduces to eq. (3.9). The total temperature increase in the silicon core is the

sum of the four nodes contributions: $\Delta T_{tot}(t) = \sum_i^n \Delta T_i(t)$. The refractive index due to self-heating is directly computed as:

$$\Delta n_{eff,T,1,2} = \Gamma_{1,2} \frac{dn_{Si}}{dT} \Delta T_{tot}. \tag{3.48}$$

The dynamic response of the resonator can be obtained by solving the system of ordinary differential equations formed by eq. (3.13), (3.45), (3.46), and (3.47).

3.4.2 Pump-probe effective losses, generation rate and XPM

The generation rate characteristic of steady state as shown in eq. (3.20) is generally valid in the time domain description. However in a pump-probe experiment the presence of two different fields gives additional contributions to carrier generation $G(t)$ and field losses $\alpha_{eff,1/2}(t)$. In the case of NL losses, XTPA causes a pump (probe) photon to be absorbed together with another probe (pump) photon in the TPA process. For the pump field we have:

$$\alpha_{eff,1} = \alpha_0 + \frac{\beta_{TPA}}{A_{eff,1}} P_{c,1} + 2 \cdot \frac{\beta_{TPA}}{A_{eff,av}} P_{c,2} + \Gamma_1 \Delta\alpha_{FCA}, \tag{3.49}$$

while for the probe:

$$\alpha_{eff,2} = \alpha_0 + \frac{\beta_{TPA}}{A_{eff,2}} P_{c,2} + 2 \cdot \frac{\beta_{TPA}}{A_{eff,av}} P_{c,1} + \Gamma_2 \Delta\alpha_{FCA}. \tag{3.50}$$

Where $A_{eff,av} = \sqrt{A_{eff,1} A_{eff,2}}$. The term $2 \cdot \frac{\beta_{TPA}}{A_{eff,av}} P_{c_{1,2}}$ is related to XTPA, here the factor 2 originates from cross-term contribution of the nonlinear polarization χ^3 causing the mixing of the pump and probe fields (which are set at two different ω) to exhibit twice total components than in the case of SPM.[59, 130].
For the losses related to the pump field propagation, the effect of XTPA caused by the probe is completely negligible with respect to the TPA by the pump since during the pump propagation (i.e., when the pump pulse is On) the probe power is very low ($P_{bus} < -20dBm$). However in the case of probe losses, see eq. (3.50), the XTPA contribution by the pump causes losses that are comparable to FC losses. For this reason in a pump-probe experiment, to retrieve the carrier dynamics, we have to analyse the probe signal after the pump pulse has ended so that eq. (3.50) reduces to

(3.2).
The losses due to XTPA causes additional free carrier generation, neglecting SCA due to the probe, eq. (3.20) now becomes:

$$G = G_{SCA,1} + \frac{\beta_{TPA} P_{c,1}^2}{2\hbar\omega_{0,1} A A_{eff,1}} + \frac{\beta_{TPA} P_{c,2}^2}{2\hbar\omega_{0,2} A A_{eff,2}} + \frac{\beta_{TPA} P_{c,1} P_{c,2}}{\hbar\omega_{0,1} A A_{eff,av}} + \frac{\beta_{TPA} P_{c,1} P_{c,2}}{\hbar\omega_{0,2} A A_{eff,av}}. \tag{3.51}$$

The first three terms are the SCA and TPA contributions from pump and probe which are completely analogous to those defined in eq. (3.20). Whereas $\frac{\beta_{TPA} P_{c_{1,2}} P_{c_{2,1}}}{\hbar\omega_{0_{1,2}} A A_{eff,av}}$ is the generation term related to XTPA free carriers. Here the factor 2 at denominator is missing since in XTPA only one probe (pump) photon is absorbed instead of two photons, as in TPA, since the other photon is provided by the pump (probe). The third term in eq. (3.51) is completely negligible with respect to the pump case for what said previously about the probe bus power. Moreover the XTPA cross terms gives an important contribution only during the pump propagation, when the high number of generated carriers will greatly increase NL losses. Lastly the pump and probe influence each other also in the so called cross-phase modulation (XPM) effect that adds up to the SPM effect defined in eq. (3.11):

$$\Delta n_{eff,Kerr,1,2} = \Gamma_{1,2} n_2 \left(\frac{P_{c,1,2}}{A_{eff,1,2}} + 2\frac{P_{c,2,1}}{A_{eff,av}} \right), \tag{3.52}$$

The second term represents the effect of the probe (pump) field on the other pump (probe), and includes an additional factor 2 for the same reason as in the case of $XTPA$.
We conclude this section by noting that the transmission at the through port given in eq. (2.3) is valid only in steady state. $T_{thr}(t)$ is a function of time and is obtained by the sum the fraction of the input bus power not coupled with the ring and the circulating power escaping from the ring, namely:

$$T_{thr,1}(t) = \left| \sqrt{P_{bus,1}} t_1 + E_{c,1}(t) \kappa \sqrt{1-\eta^2} a_1(t) \right|^2 / P_{bus,1} \tag{3.53}$$

We neglect here the short delay, τ_g between bus power and probe circulating power in one round trip since it is much smaller than any carrier recombination lifetime: for example when $n_g = 3.45$ we have $\tau_g = 1.12\,ps$ which is negligible when compared

to free carrier lifetimes of the order of *ns* as measured in this thesis in the case of silicon MRRs.

Self-oscillation

In a pump-probe experiment the self-heating effect is usually negligible with respect to FCD due to the small pump pulses energies (μJ). However the thermal dynamics is relevant when the ring enter in self-oscillation. Here the output power of the ring suffers periodic oscillations with CW injection; this instability is caused by the interplay between the temperature increase and free carrier generation and recombination [123, 126] as we will show in chapter 4.5. Such scenario represents a simplified case of the previous theory where only one circulating field related to a constant bus power is considered, for example assuming to have $P_{bus,1}$ constant with time and $P_{bus,2}, P_{c,2}, P_{abs,2}$ are all zero.

Chapter 4

Characterization of microring resonators

4.1 Devices under tests

In this thesis we consider three types of SOI MRRs labelled as $R1$, $R2$ and $R3$ whose layout is shown in figure 4.1 (a), (b), (c) and (d). We highlight that the racetrack resonator $R1$ has been fabricated in a different foundry than the $R2$ and $R3$. In the racetrack resonator $R1$, light is coupled vertically through surface grating coupler (SGC), whereas in the cases of rings $R2$ and $R3$ an edge coupling technique is adopted with SSCs used to optimise the coupling efficiency between the field and small waveguide cross section in the chip [32]. Polarization controllers (PCs) have been used to accurately select the polarization of the incident light on both SGCs and SSCs, since these have been designed to work only for TE polarization.
The main characteristics of these rings are summarised in table 4.1 whose electric field distribution of the bent waveguide is shown in figure 4.1 (e).

Table 4.1 Dimension of MRRs analysed in this thesis.

Parameter	Si racetrack $R1$	Si ring $R2$	Si/poly-Si Ring $R3$	Unit
L	80	31.4	12.6	μm
W	450	580	$W_{Si} = W_{poly-Si} = 400$	nm
h	215	107	$h_{Si} = 115$, $h_{poly-Si} = 125$	nm

In $R1$ case, the bending sections, see fig. 2.2, have a radius of $5\mu m$, $L_d = 19\,\mu m$,

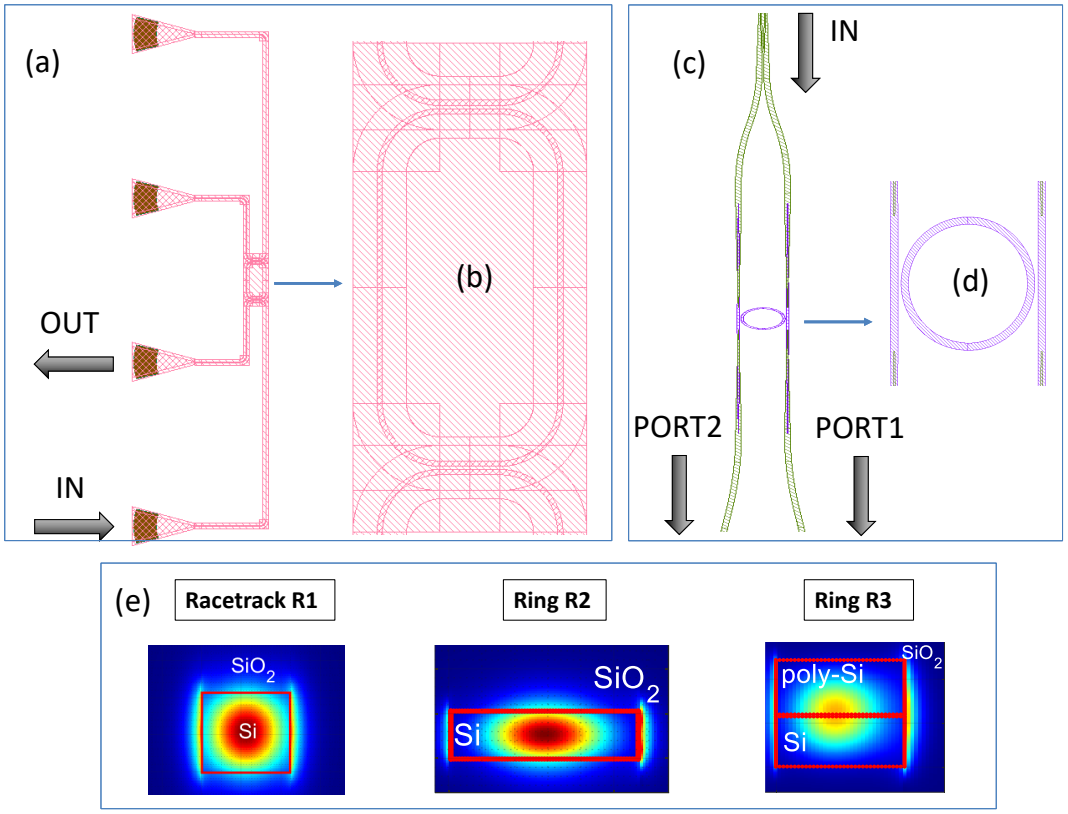

Fig. 4.1 (a) Layout of the racetrack resonator $R1$ and (b) zoom in the bus-ring coupling region and (c) and (d) for MRRs $R2$ and $R3$. (e) Electric field distributions in the cross sections of the three resonators considered in this thesis.

and $L_c = 5\,\mu m$. Lastly, $R3$ structure is based on SISCAP platform [107] where the ring waveguide consists in a rectangular undoped polysilicon core on top of a Si core. In poly-Si, the defects within the crystalline grains act as recombination centers for free carriers, dramatically decreasing the free carriers lifetimes with consequent reduced impact of FCA and increase of switching time when the MRR is employed as an all optical switch [108]. However polysilicon has generally larger linear losses than silicon due to the defect state absorption caused by the high number of defects associated to the grain boundaries. In this contest, the grain size plays a fundamental role in determining the material properties [96, 97, 109–111]. In fact the carrier electrical mobility, trap density, and thermal conductivity [112] are dependent on the grain size and so on the deposition technique [113, 114]. What makes this type of ring interesting is that the field propagating in the structure is almost equally confined in both cores (at $\lambda = 1579.1\,nm$ the optical confinement factors in silicon and polysilicon are $\Gamma_{Si} = 0.46$ and $\Gamma_{poly} = 0.51$). As a result the total linear and

NL losses affecting the circulating field in the ring will be the weighted sum of the silicon and polysilicon contributes by the respective confinement factors, whereas the free carriers lifetime will be different in the two materials due to the faster recombination in polysilicon. Moreover the total height of the waveguide equal to $240\,nm$ makes it possible to reach ring radii lower than silicon, in fact for ring R3 is $r = 2\,\mu m$.

4.1.1 Thermal impedance

In order to reproduce the experimental results, we simulated resonators $R1$ and $R2$ on COMSOL to retrieve the thermal impedance that accounts for self-heating as explained in section 2.3. The geometrical parameters defined in section 2.3 associated to the distances between the different materials in resonators $R1$ and $R2$ are summarised in table 4.2.

Table 4.2 Si and SiO_2 layers specifications for resonators $R1$ and $R2$.

Parameter	Si racetrack R1	Si ring R2	Unit
R_{sub}	500	500	μm
H_{sub}	710	565	μm
H_{SiO_2}	3.6	14	μm
D_{Si/SiO_2}	1.9	8.6	μm

While the simulation results are shown in figure 4.2. We notice that, for the same length, racetrack $R1$ has always a lower Z_T than ring $R2$ due to the distance between the substrate and Si core being lower in $R1$ case.
Finally, the set of thermal time constants and thermal impedances introduced in section 2.3 for the characterization of the MRRs in time domain are summarised in table 4.3, here the capacitance is computed by inverting eq. (2.26). The minimum number of nodes required to have good fitting with the Foster equivalent circuit is 4 for both resonators $R1$ and $R2$. The significant difference between the time constants of $R1$ and $R2$ is associated again with the distance between the core and the substrate, see table 4.2 and to resonator $R1$ being more than twice longer than ring $R2$ making heat dissipation easier.

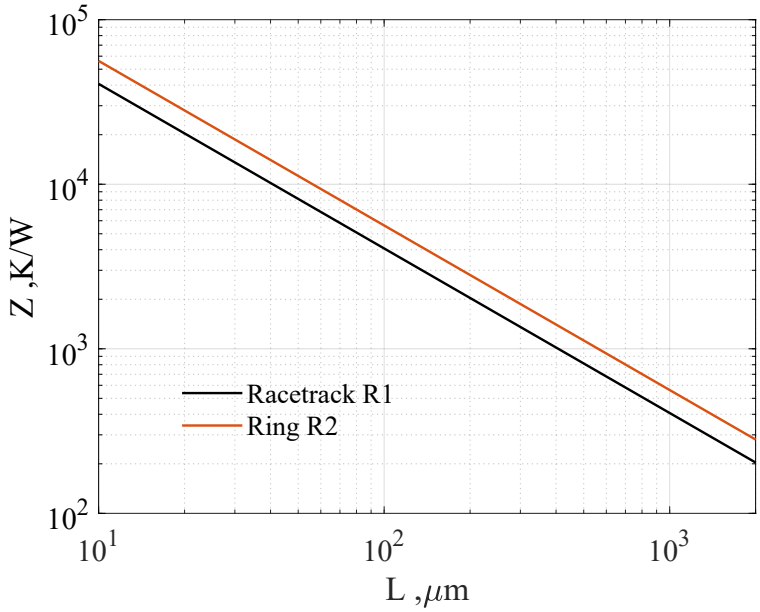

Fig. 4.2 Thermal impedance of resonators $R1$ and $R2$ as a function of the total resonator length.

Table 4.3 Thermal time constants and impedance for each of the 4 nodes of the Foster equivalent circuit of resonators $R1$ and $R2$.

time constant	Si racetrack R1	Unit	Si ring R2	Unit
$\tau_{th,1}$	14.7	ns	1.15	μs
$\tau_{th,2}$	130.8	ns	1.15	μs
$\tau_{th,3}$	891.4	ns	18	μs
$\tau_{th,4}$	5	μs	91	μs
$Z_{T,1}$	538	Ω	3.4	$k\Omega$
$Z_{T,2}$	1.2	$k\Omega$	5.5	$k\Omega$
$Z_{T,3}$	1.1	$k\Omega$	4.1	$k\Omega$
$Z_{T,4}$	2.2	$k\Omega$	5.8	$k\Omega$

4.2 Experimental setup

In this section we validate our model by comparing the simulation results with measurements of transmission spectra of different resonators. Then measurements on ring $R3$ are introduced together with a method for the extraction of the carrier lifetime in ring resonators.
A scheme of the experimental setup is shown in Fig. 4.3 for continuous wave and pump-probe characterization of the MRRs.

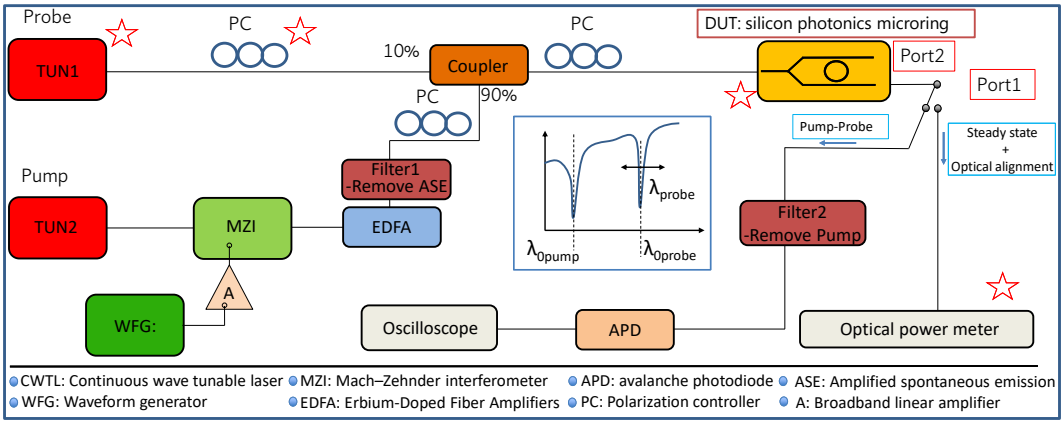

Fig. 4.3 Setup implemented in CW and pump-probe MRR measurement. We remind that in the case of the racetrack resonator $R1$ the input power is sent only at the through port of the ring, see Fig. 2.2. The optical coupling with the DUT is done by vertical coupling for resonator $R1$, and by edge coupling for rings $R2$ and $R3$. Red stars indicate the instruments used for steady state measurements. A sketch of the basic principle of the pump-probe measurement is displayed in the inset: the pump wavelength is kept constant at one ring resonance $\lambda_{0,pump}$ and the probe wavelength λ_{probe} varied around an another resonance $\lambda_{0,probe}$.

Steady state setup

To measure the ring transmission coefficients in both linear and non-linear regime in steady state, the power is injected in the bus waveguide from the tunable laser labelled as TUN 1 (Agilent 81980A) amplified with an Erbium Doped Fiber Amplifier (EDFA) . In this way it is possible to reach powers entering in the ring as high as $7\,dBm$, the residual Amplified Spontaneous Emission (ASE) is minimized by an optical filter. Then by sweeping the tunable laser wavelength from blue to red wavelengths around one selected resonant wavelength of the ring $\lambda_{0,R1/R2}$, we get the transmission coefficient at the through port measured as the ratio between the power in the bus waveguide and the power at the through port of the ring by an optical power meter (PM). The I/O fiber-chip alignment is achieved by means of a 6 degree mechanical stage positioning system with a precision of $\pm 0.06 \mu m$. Lastly the chip is positioned on top of a Peltier cell whose temperature is kept fixed at 25° by using a Thermo Electric Cooler (TEC) controller with an accuracy of $\pm 0.05\,K$.

To detect self-oscillation in the output power we use an optical receiver and an oscilloscope with bandwidth (BW) $1.1\,GHz$ and $300\,MHz$ respectively.

Pump and probe setup

In order to perform a pump-probe experiment two different CW tunable lasers, a probe (TUN1) and a pump (TUN2: N7714A Agilent Multiport) must be usually employed [123, 124, 144]; the pump-probe wavelengths are positioned on adjacent ring resonances separated by one FSR as shown in the inset of Fig.4.3, i.e., $\lambda_{0,pump}$ and $\lambda_{0,probe}$. The high power pump CW signal is first modulated by a MZI (extinction ratio $\approx 27\,dB$) and subsequently amplified by an EDFA in order to achieve high peak power pulses. A waveform generator (Anritsu WFG $BW = 40\,GHz$) makes it possible to have pump pulses from the MZI with period as small as $100\,ps$, while the CW probe power in the bus is kept below $-20\,dBm$, in order to avoid any NL effect and self-heating due to the probe. Furthermore, the pump repetition rate ($4\,kHz$) is by design much larger than the pump pulse so that we avoid any thermal effects.
Filter1 is an optical grating filter which is centered at the pump wavelength and it is used in order to remove the amplified spontaneous emission by the EDFA. The pump is then fixed at $\lambda_{0,pump}$ and the probe wavelength (λ_{probe}) varied around the resonant wavelength ($\lambda_{0,probe}$). After TPA and FCA partially absorb the pump pulse and generate free electrons and holes, the CW probe monitors the nonlinear response of the ring over time for any wavelength. An avalanche photodiode (APD Lab Buddy, $BW = 7\,GHz$) coupled with a fast oscilloscope (Agilent Infinium 83484A $BW = 50\,GHz$) are used to detect the weak probe signal collected at the output of the resonator with the residual pump pulses filtered out by Filter2.

4.3 Linear regime parameters

To understand NL effects and precisely setting a pump-probe experiment, we need to perform a preliminary study of the MRRs in linear regimes. In the next three sections the low input power (LP) spectra of all three resonators considered in this thesis are characterised. Since the power in the racetrack resonator $R1$ is injected into the input port, and the resonator exhibits very similar coupling coefficients for both upper and lower waveguides (i.e., $\kappa_1 = \kappa_2$), the ring response is measured only at the through port, see fig. 2.2, making the steady state characterisation procedure faster.

Racetrack resonator R1

Figure 4.4 shows the low power transmission spectrum at the through port in the case of the racetrack resonator $R1$ for two adjacent resonances, $\lambda_0 = 1540\,nm$ and $\lambda_0 = 1547\,nm$. Since we have no NL effects, we can fit the experimental measurements with eq. (2.3),(2.6) to get the coupling coefficient κ and coupling losses η^2. The linear losses in the resonator are estimated by the foundry, of about $\alpha_0 = 2\,dB/cm$, whereas the group index is calculated by simulating the bent waveguide on Photon Design.

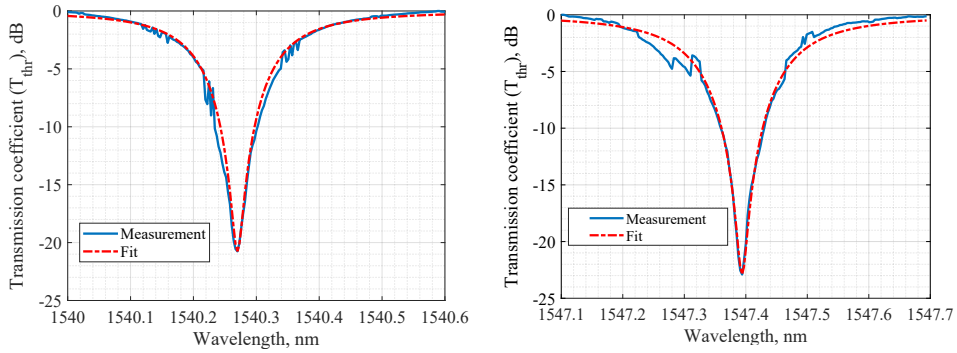

Fig. 4.4 Experimental and fitted linear transmission spectra at the through port of the racetrack resonator $R1$ at two adjacent resonances of about $1540\,nm$ (a) and $1547\,nm$ (b).

Coupling losses do not depend on wavelength, but are caused by the bus waveguide and resonator distance [99], therefore we fix $\eta^2 = 0.0047$ for both resonances. The fitting gives $\kappa^2_{1540\,nm} = 0.0668$ and $\kappa^2_{1547\,nm} = 0.0811$ associated to quality factors $Q_{1540\,nm} = 9738$ and $Q_{1547\,nm} = 8378$. We see that the dispersion causes the ring quality factor to naturally reduce with increasing wavelength. Therefore, in the pump-probe experiments, the pump is always placed at the lower wavelength resonance, this allows an higher generation of free carriers in the MRR as a consequence of the superior circulating power build-up .

Ring resonator R2

We repeated the same procedure for rings $R2$, however the coupling coefficients of the upper and lower arms are different due to deviations of the bus-ring distances from the nominal value of $250\,nm$. This is clearly seen in figure 4.5 where we recorded

the ring transmission coefficients at both Port1 and Port2. Here eqs. (2.11),(2.12)

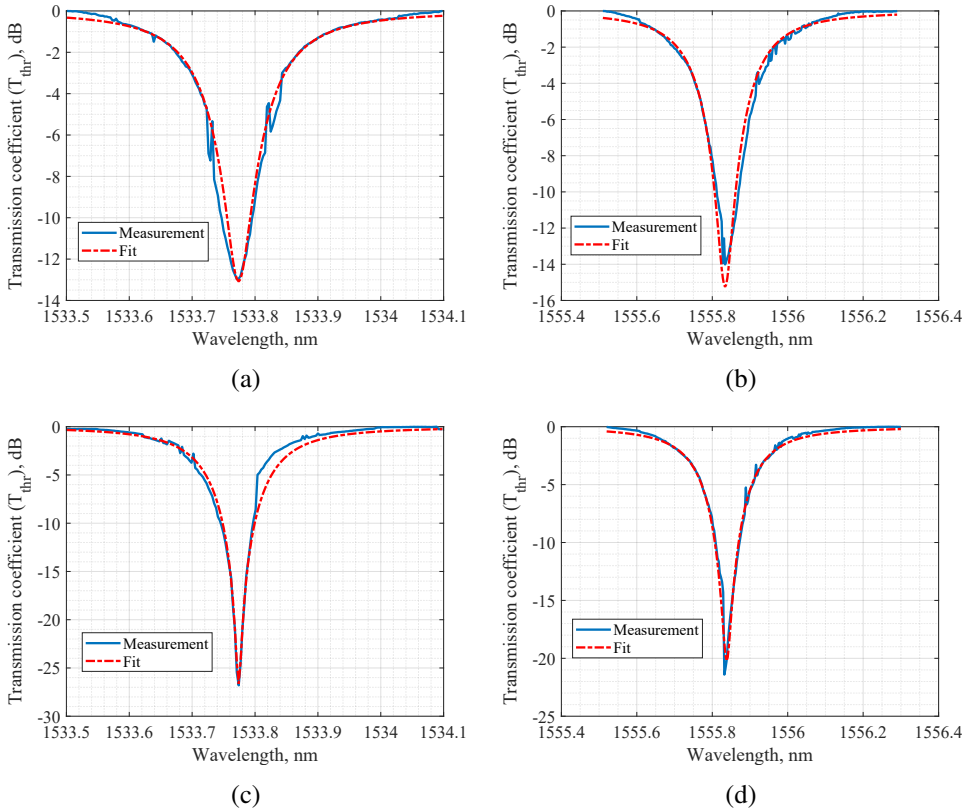

Fig. 4.5 Experimental (blue) and fitted (red) linear transmission spectrum of ring $R2$ (a) and (b) at port1, (c) and (d) at port2.

have been used to fit the experiment. All the linear parameters for resonators $R1$ and $R2$ are summarised in table 4.4. This ring has a Quality factor at the pump resonance equal to $Q_{1533} = 9900$.

Table 4.4 Model parameters extracted from the transmission spectra of resonators $R1$ and $R2$ at low input power and by simulation of the resonator bent waveguide with an the electromagnetic mode solver (Photon Design).

Parameter	R1 Pump	R1 Probe	R2 Pump	R2 Probe	Unit	Source
λ_0	1540.3	1547.4	1533.7	1555.8	nm	Fitting of $T_{thr}(\lambda)$
κ^2	0.066	0.081	$\kappa_1 = 0.0172$, $\kappa_2 = 0.021$	$\kappa_1 = 0.0175$, $\kappa_2 = 0.02068$	-	Fitting of $T_{thr}(\lambda)$
η^2	0.0047		0.002		-	Fitting of $T_{thr}(\lambda)$
α_0	2		1.02		dB/cm	Foundry specification
n_g	4.26		3.45	3.42	-	Electromagnetic mode solver.
α_{rad}	< 0.01		1.73	3.8	dB/cm	Electromagnetic mode solver.
$n_{eff,0}$	2.34	2.33	1.95	1.93	-	Electromagnetic mode solver.
Γ	1		0.69	0.67	-	eq. (2.18)
A_{eff}	0.075		0.104	0.109	μm^2	eq. (2.20)

Ring resonator R3

The linear regime characterisation of Si/poly-Si ring is shown in in fig. 4.6, with the ring cross-section displayed in the inset of fig. 4.6 (b). As previously explained, the total linear loss in the ring is written as the combination of the silicon and polysilicon waveguide contributions weighted by the confinement factors Γ_{Si} and Γ_{poly}. For the optical simulation we assumed the polysilicon refractive index to be the same of silicon since, at $1.5\,\mu m$, the difference between c-Si and undoped poly-Si is marginal ($< 3\%$ [110, 145]).
Considering that the distance between the bus and ring waveguides is the same for ring $R2$ and $R3$ ($250nm$) and the two resonators are placed on the same chip, we assume $R3$ coupling losses to be approximately the same of ring $R2$, i.e., $\eta^2 = 0.002$.

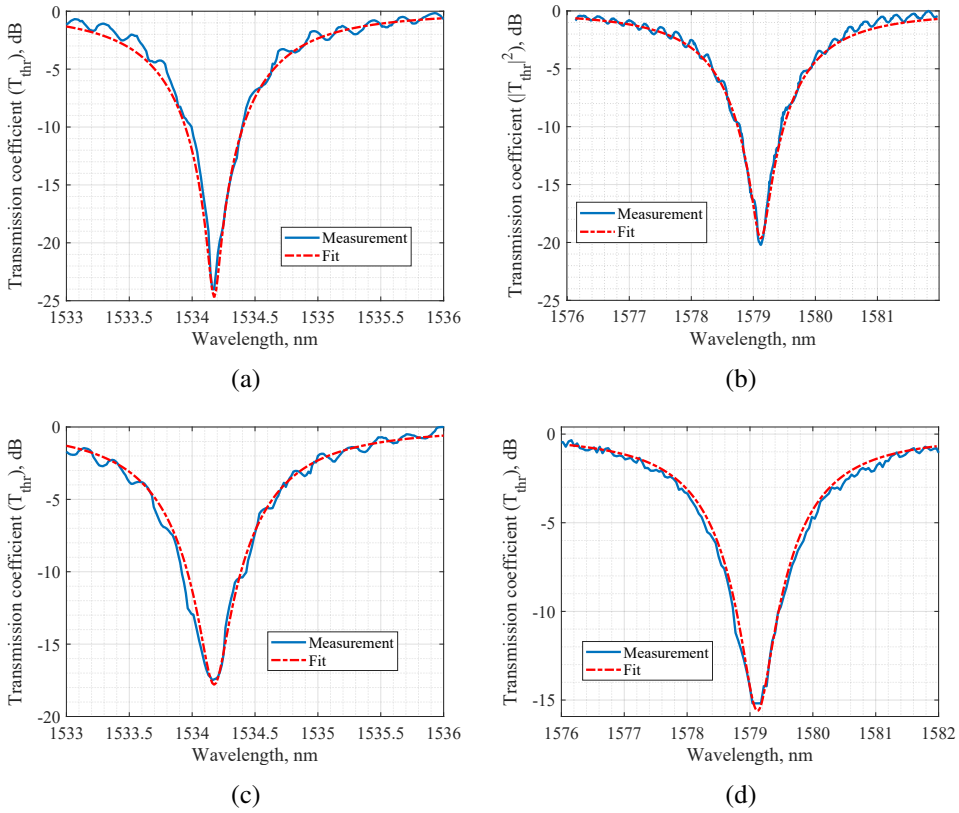

Fig. 4.6 Experimental (blue) and fitted (red) linear transmission spectrum of ring $R3$ (a) and (b) at port1, (c) and (d) at port2.

Table 4.5 Model parameters extracted from the transmission spectra of resonators $R3$ at low input power and by simulation of the resonator bent waveguide with an the electromagnetic mode solver (Photon Design).

Parameter	R3 Pump		R3 Probe		Unit	Source
	Silicon	Polysilicon	Silicon	Polysilicon		
λ_0	1534.1		1579.1		nm	Fitting of $T_{thr}(\lambda)$
κ^2	$\kappa_1 = 0.098$, $\kappa_2 = 0.081$		$\kappa_1 = 0.164$, $\kappa_2 = 0.127$		-	Fitting of $T_{thr}(\lambda)$
η^2	0.002				-	Fitting of $T_{thr}(\lambda)$
α_0	1.02	8	1.02	8	dB/cm	Foundry specification
n_g	4.2		4		–	Electromagnetic mode solver
α_{rad}	5.44		16.63		dB/cm	Electromagnetic mode solver.
$n_{eff,0}$	2.31		2.26		-	Electromagnetic mode solver.
Γ	0.50	0.50	0.46	0.51	-	eq. (2.18)
A_{eff}	0.140	0.165	0.177	0.159	μm^2	eq. (2.20)

Figure 4.6 shows the measured and fitted spectrum for two adjacent resonances for ring $R3$, with the fitting parameters summarised in table 4.5. We note that in all the cases the spectrum present oscillations. Back reflection between the fiber tip and input waveguide cannot be ascribed as cause of these oscillations since we are using fiber lens with anti-reflection (AR) coating. In fact these oscillation are not present in the case of ring $R2$ where alignment conditions are essentially the same as for R3. We believe they originate from contra directional coupling of the propagating field inside the ring cavity caused by spurious reflections due to the grain boundaries, which we can associate with an equivalent higher surface roughness of the material [146]. This effect has also been observed in other studies involving polysilicon ring resonators [147]. For even larger values of surface induced reflection inside the ring, we have the splitting of the resonant wavelength, that we measured in other Si/poly-Si rings not reported here.

SRH fitting parameters

To reproduce the experimental results of next section, we obtained the SRH model parameters quantifying the capture dynamics of carriers in the traps by fitting steady state measurements and cross checking the results with pump-probe experiment (see section 4.6). In order to decrease the number of unknowns, we consider donor type traps with non degenerate energy levels [134] which are usually assumed to be close to the middle of the band gap [126, 132, 134, 135]; as a result we vary E_t from $0.6\,eV$ to $0.7\,eV$. The electron capture cross section is a function of the energy of the

traps (i.e., $\sigma_n(E_t)$), we extrapolate this function for energies above the mid-gap from measurements reported in [55] as shown in fig. 4.7.

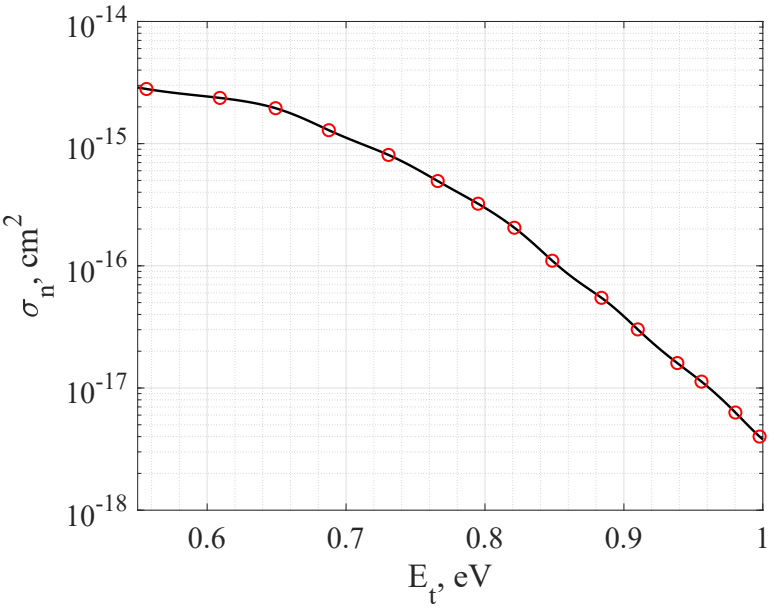

Fig. 4.7 Electron capture cross section as a function of trap energy level extracted from [55].

As reported in the literature [55, 134], it is not possible to measure both the electron and hole capture cross sections when the trap energy level is far from the mid-gap, therefore we suppose $\gamma = 0.05$ [135] which was estimated from the ratio of measured cross-sections when E_t is at mid-gap [55]. As a result once E_t is fixed, $\sigma_n(E_t)$ and $\sigma_p(E_t)$ are uniquely defined since $\gamma = \tau_{n0}/\tau_{p0} = \frac{v_p \sigma_p}{v_n \sigma_n}$. The residual doping of silicon is set to $N_a = 10^{15}\, cm^{-3}$ following the technology guidelines by the foundry in the case of ring $R2$ and corresponding to $\psi_f \approx 0.23\, eV$. This value has also been used for the resonator $R1$ due to the lack of data about residual doping. With the previous assumptions the total number of fitting parameters is reduced to two: the trap energy level E_t and trap density N_f. In the next chapter we validate the model by considering experimental measurements conducted on resonators $R1$ and $R2$.

4.4 Steady state measurements in nonlinear regime

In this section we characterize resonators $R1$ and $R2$ in steady state, we focus on the resonances referred as pump resonances in table 4.4 which are associated to FC generations.

4.4.1 Racetrack resonator R1

The measured and simulated transmission spectra are shown in fig.4.8 (a) and 4.8 (b) for different bus input powers. Here, the black curve corresponds the linear response

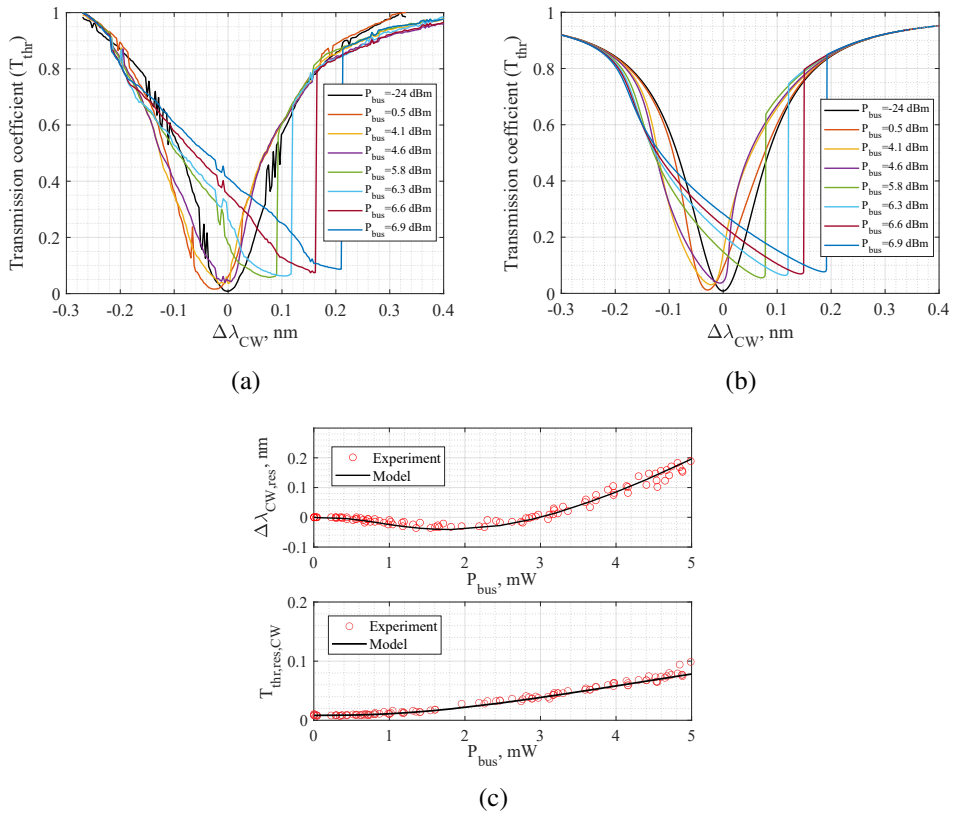

Fig. 4.8 Transmission coefficients at different input bus power measured (a) and simulated (b) by sweeping the input wavelength from the blue to red side of the resonant wavelength in the case of ractrack resonator $R1$. The simulated spectrum was obtained with $E_t = 0.65\,eV$ and $N_f = 7.9 \cdot 10^{15} cm^{-3}$. (c) Resonant wavelength shift $\Delta\lambda_{CW}$ (top) and variation of the transmission coefficient at resonance (bottom) as a function of the CW input bus power.

of the ring obtained with a low input power. For increasing P_{bus}, the circulating

power increases leading to higher propagation loss and variation of silicon refractive index. These cause first a slight blue shift of the resonant wavelength due to FC effect being dominant over the temperature rise, then a significant red shift caused by self-heating. The parameters we used to fit the experiment with our model are the variation of the ring resonant wavelength ($\Delta\lambda_{CW} = \lambda_{res} - \lambda_0$) and the transmission coefficients at the through port at resonance ($T_{thr,res,CW}$) as reported in Fig. 4.8 (c) and extracted from the measured transmissions spectra in fig.4.8 (a) and 4.8c (b). The continuous line in fig. 4.8 (c) is the simulation result obtained with $E_t = 0.65\,eV$ and $N_f = 7.9 \cdot 10^{15} cm^{-3}$. We set $\eta_{SCA,R1} = 0$ since we do not have this type of information from the foundry, while $\beta_{TPA,R1} = 0.8\,cm/GW$, i.e. the bulk silicon TPA coefficient. Using eq. (3.12) the calculated surface trap density is $N_s = 1.82 \cdot 10^{11}\,cm^{-2}$ that is in agreement with experimental measurements on Si/SiO_2 interfaces [55, 148]. Therefore the trap density and trap energy level play an important role in defining the carriers dynamics which determines the density of free carriers and hence the shift of the resonant wavelength and the degradation of the transmission coefficient, as we reported in [58]. Nonetheless we clearly see that the model can reproduce well the measured results with the only difference related to the transmission spectrum in fig. 4.8 (a) between $\Delta\lambda_{CW,res} = 0$ and $\Delta\lambda_{CW,res} = 0.2\,nm$. Such discrepancy is due to the self-oscillation of the output power at through port that are observed when the bus power is high enough and the input field wavelength close to the ring cold resonance as we will discuss later.

Based the on parameters extracted from the experiment, we have calculated with our model the FC lifetimes, FC densities and corresponding NL loss and effective refractive index change. The simulated free carrier lifetimes, calculated in chapter 3.2.3 as $\tau_p = p_e/G_e$ and $\tau_n = n_e/G_e$, are shown in fig. 4.9 (a), we note that at $P_c > 20\,mW$ which corresponds to a $P_{bus} = 2.6\,dBm$, the electron and hole FC lifetimes are very close the saturated equivalent carrier lifetime which is equal to $\tau_\infty = 59\,ns$ as calculated with eq. (3.19). At this power (see for example figure 4.9 (b)) free electron are almost equal to free holes, i.e., equal to $\approx 1 \cdot 10^{17} cm^{-3}$. This value and the τ_∞ introduced before are in accord to what obtained from fitting of dynamic measurements for a similar ring resonator structure reported in [132] which confirms our procedure. Fig. 4.9 (b) shows the contribution to the effective losses of linear losses (dotted red line), TPA losses (black dotted line) and total losses including also FCA (blue curve). We note how TPA losses are completely negligible with respect to FCA for this particular resonator. Lastly in fig. 4.9 (c) we summarise

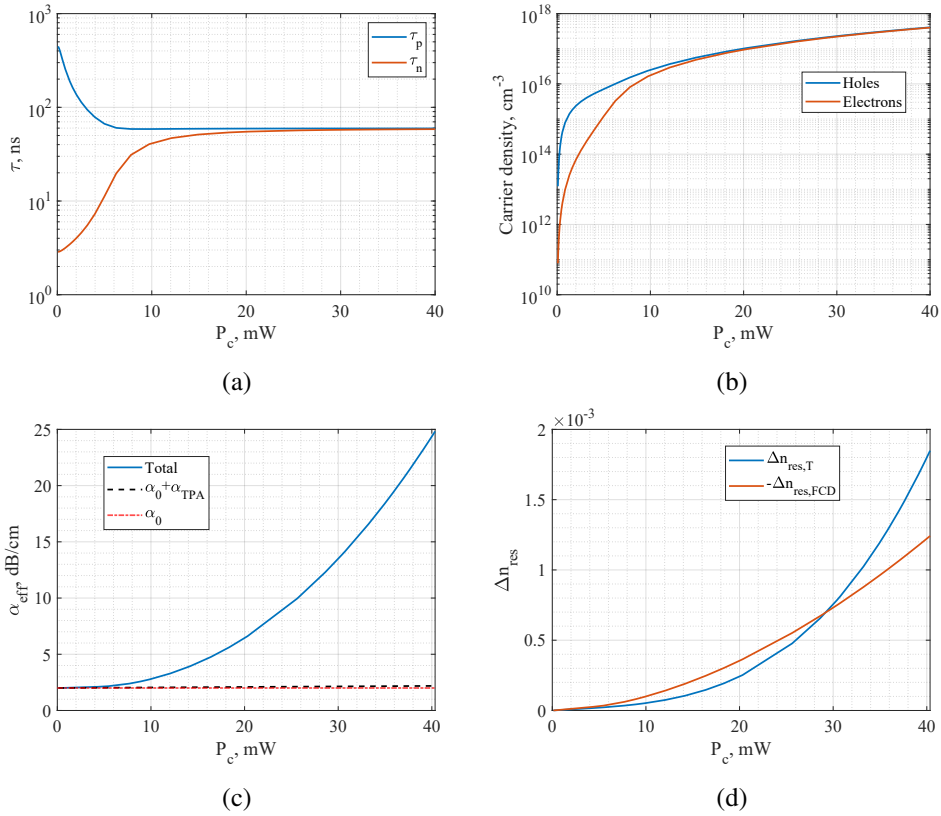

Fig. 4.9 (a) Free carrier lifetime and free carrier densities (b) of holes and electrons at resonance. (b) Effective losses at resonance versus the circulating power in the ring. (c) Contributions to the effective refractive index change of free carriers and temperature with FC contribution displayed with reverse sign.

the contributions of free-carriers and temperature due to self-heating to the overall refractive index shift in the silicon waveguide. The FC component is plotted with reverse sign in order to compare it with the temperature contribution. For circulating power below $P_c < 30\,mW$ ($P_{bus} \approx 3\,dBm$), the FC generation has a larger impact than self-heating casuing a blue shift of the resonance that can be observed in the resonant wavelength shift in figure 4.8 (c).

4.4.2 Ring resonator R2

In the case of ring $R2$, the foundry also provided power loss measurements on rectangular straight waveguides with same dimension as ring $R2$ waveguide, we have used these data to extrapolate values for η_{SCA} and β_{TPA}. Fitting of these data revealed

$\eta_{SCA,R2} = 0.04$ and $\beta_{TPA,R2} = 1.5 cm/GW$ as shown in Appendix B. With these parameters, the reproduction of the experimental transmission and resonant wavelength shift at resonance was possible with $E_t = 0.63\,eV$ and $N_f = 8.5 \cdot 10^{16} cm^{-3}$ associated to $N_s = 3.8 \cdot 10^{11} cm^{-2}$; results are shown in figure 4.10.

One main difference in the impact of NL effects on the ring response between this

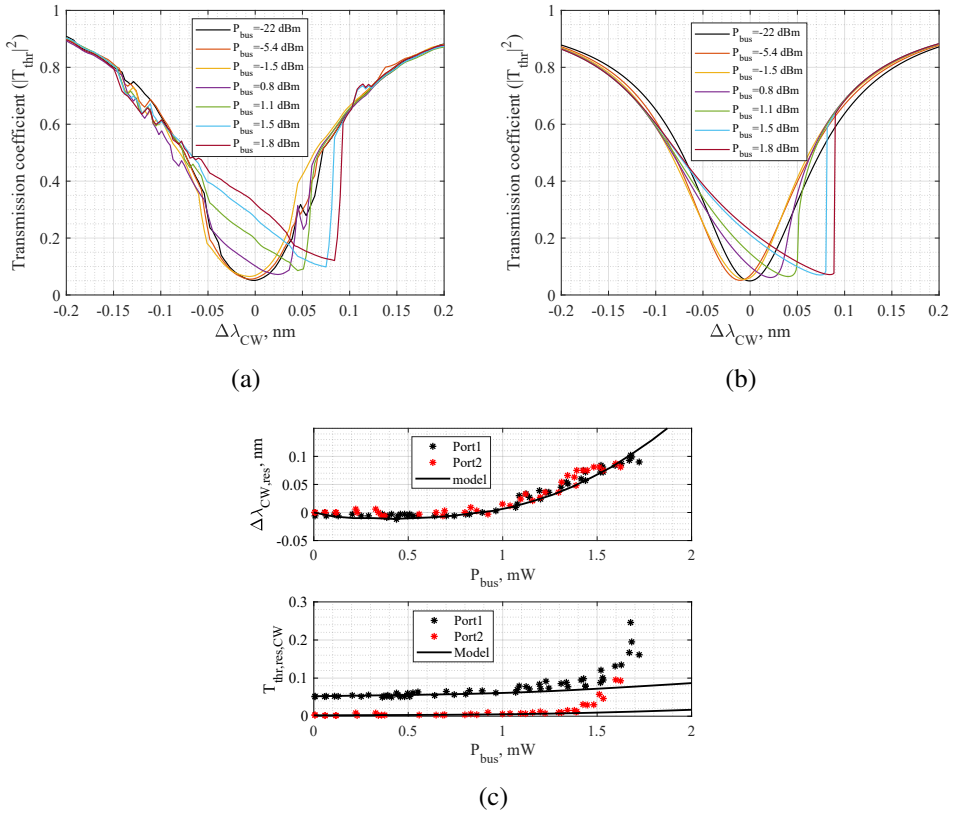

Fig. 4.10 Transmission coefficients at different input bus power measured (a) and simulated (b) by sweeping the input wavelength from the blue to red side of the resonant wavelength in the case of ring resonator $R2$ at Port1. The simulated spectrum was obtained with $E_t = 0.63\,eV$ and $N_f = 8.5 \cdot 10^{16} cm^{-3}$. (c) Resonant wavelength shift $\Delta\lambda_{CW}$ (top) and variation of the transmission coefficient at resonance (bottom) as a function of the CW input bus power for both Port1 and Port2.

ring and resonator $R1$ is that here the ring becomes unstable (see section 4.4) for input power as low as $1.7\,dBm$ ($P_{bus} = 1.5\,mW$). The reason is that the circulating power in this ring is more than twice the one in racetrack $R1$. In fact, in the case of an input power of $P_{bus} = 1\,mW$ at resonance, we have that $P_{c,R1,res} = 12\,mW$ whereas for ring $R2$ it is $P_{c,R2,res} = 37\,mW$. Also in the case of ring $R2$ we observe a good match between the theory and experiment.

It is important to remark that in order to reproduce the steady state measurements, and also NL power loss measurements on straight waveguides reported in the appendix, we increased the TPA coefficient up to almost double the value used in the case of racetrack $R1$, i.e., the bulk TPA coefficient. We associate this discrepancy to the very small area of the silicon waveguide, which results in enhanced NL effects in silicon with respect to the bulk case [100, 149, 150], in fact $R1$ height is more than twice the one of ring $R2$, see table 4.1.

4.5 Racetrack resonator self-oscillation

As we see in both resonators $R1$ and $R2$, when the input power is high enough the model is no more able to follow the experimental results, especially for what regards the transmission losses in the ring. The reason is due to self-oscillation of the ring output power over time [123, 126, 132], see figure 4.11 in the case of racetrack $R1$. In order to detect any oscillation in the ring, the output power at the through port of the ring is recorded by an optical receiver and visualised on an oscilloscope. The bus input power is calculated to be around $10\,dBm$ with $\lambda_{in} \approx \lambda_0$; we inject such an high power in order to clearly see the trace. As it is possible to see, the recorded

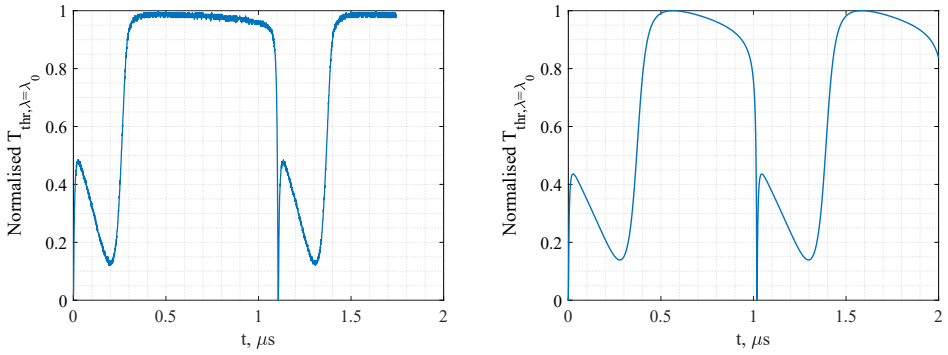

(a) (b)

Fig. 4.11 (a) Normalised measured output signal versus time out the optical receiver at the through port of racetrack $R1$ for a constant input bus power equal to approximately $10\,dBm$. (b) Normalised model response at the through port. In both cases $\lambda_{in} \approx \lambda_0$.

signal is not constant when we inject CW input power. Because the input power is high enough and the pump wavelength rather close to the cold resonance frequency, we measure stable oscillations. The measured trace in Fig. 4.11 (a) is in line with

experimental results from other studies [123, 126, 132] and can also be reproduced by our time domain model, section 3.4, with constant input power as shown in fig. 4.11 (b). The model parameters have been fixed from the fitting of the steady state measurements. In both figures the transmissions have been normalised as done in [123]. The comparison of figs. 4.11 (a) and (b) shows that the model can reproduce quite well the periodic oscillations of the output power with a measured period of $1.1\mu s$ in the experiment and $1\,\mu s$ in simulations. The mismatch in the two curves can be attributed to a possible experimental misalignment of the pump wavelength with the cold resonant frequency. In addition the thermal time constant indicates the speed at which free carriers cause the build up of the self-heating inside the ring: a smaller $\tau_{th,i}$ would produce a faster thermal dissipation affecting the overall signal period and relative position of the different peaks. In fact we remind that the thermal time constants we are using in the simulations, see table 4.3, were determined by separate thermal transient simulation in COMSOL; a better matching of the experimental trace could be accomplished by coupling our ODE system with FEM COMSOL simulation and train the model with experimental measurement as done in [132]. We avoid this process here in order to maintain the model complexity low and reduce as much as possible the total computational time.

To explain the measured trace in Fig. 4.11 we compare in fig. 4.12 (a) the temperature contributions of the four thermal nodes being part of the equivalent circuit illustrated in fig. 2.13. The nodes that exhibit longer thermal time constants, i.e., ΔT_2 and ΔT_3, need a larger amount of time with respect to the other two to dissipate the heat caused by self-heating. The overall effect of these 4 temperatures on the refractive index, $\Delta n_{eff,T}$, is shown in fig. 4.12 (b) along with the contribution of free-carriers to the effective refractive index change. To compare the strength of these two effects, $\Delta n_{eff,FCD}$ is reported with reversed sign. We also plot the variation of the resonant wavelength of the ring in time $\lambda_{SO} = \lambda_{res,SO}(t) - \lambda_0$, where $\lambda_{res,SO}$ is the instantaneous resonant frequency of the ring during self-oscillation and λ_0 the ring cold resonance.
By analysing this quantity we identify four regions marked with numbers (1 to 4) in fig. 4.12 (b). In the time range marked with (1) the pump wavelength and cold resonant frequency are almost aligned causing a large increase in circulating power, this leads to FC generation responsible for a blue shift of the resonant frequency (FCD) which causes the pump and cold frequency to misalign resulting in a rapid

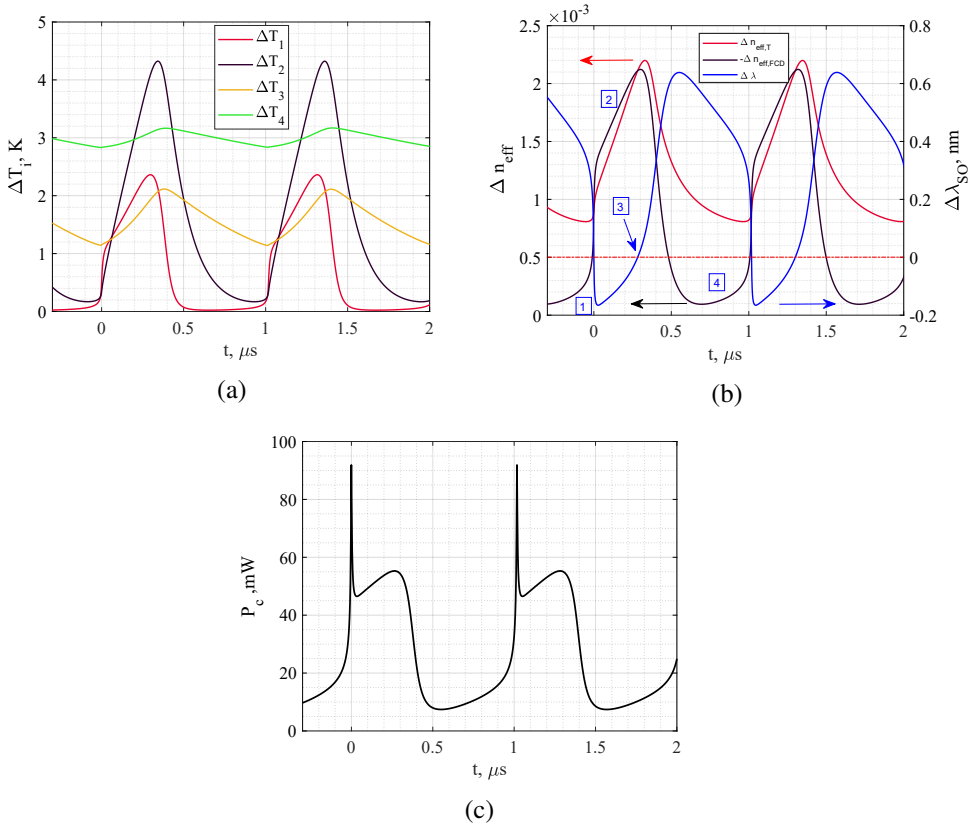

Fig. 4.12 (a) Temperature variation of the four nodes that form the equivalent thermal circuit, see fig. 2.13 with parameters from table 4.3 . (b) Temperature and FCD contributions (with reverse sign) to the effective refractive index in the silicon core (left), the variation of the resonant wavelength $\Delta\lambda_{SO} = \lambda_{res,SO}(t) - \lambda_0$ within the racetrack resonator over time is shown on the right. The red dashed line in (b) denotes the case when the resonance of the ring is equal to its cold value, i.e., $\Delta\lambda_{SO} = 0$. (c) Circulating power in the ring as a function of time.

decrease of circulating power. see for example figure 4.12 (c). In the meantime, the self-heating, originated by FC absorption, starts red shifting the resonance to its cold value (2). During this process, both FCD and self-heating increase in strength due to carriers generated by the rise in circulating power as the ring resonance approaches again the cold resonance. However, once the ring resonance is again at the cold resonance λ_0 (3), the maximum achievable circulating power is lower than in the initial case (1), because the quality factor is greatly degraded by the presence of many free carriers. The absorbed carriers translate into further heat dissipation making the resonance keep on shifting towards the red. Thus P_c decreases and therefore also the generated carriers. In time interval (4) the ring slowly cools down to the initial state once the slowest thermal dissipation process have concluded; here P_c increases

again and the whole process restarts. The complete behaviour explained above is in agreement with the literature [123, 126, 132], indicating that the model can be used to explain the experimental results even in this particular case.

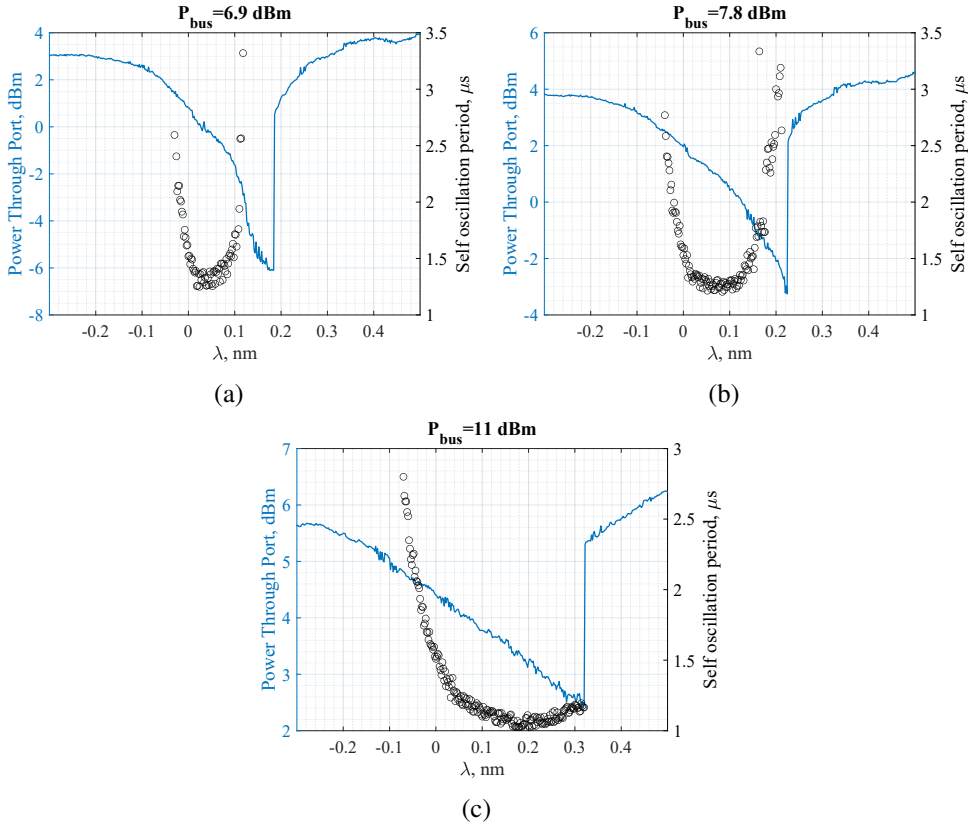

Fig. 4.13 Steady state output power at the through port in the case of racetrack $R1$ at different bus power (left) and recorded period of the self-oscillation at the drop port (right). The two measurements have been carried out simultaneously.

Self-oscillation depends not only on injected power, but also on the detuning of the probe wavelength in terms of cold resonance wavelength. This concept is well demonstrated in figure 4.13, where we collect the steady state spectrum at the through port for different powers while the drop port is sent to the oscilloscope. If some oscillations occur, the related period is simultaneously recorded on the oscilloscope. Thus, it is possible to accurately see when the ring enters the self-oscillation regime since both measurements are performed in the same alignment conditions. In addition, the duration of the oscillation does not depend on the type of port we consider, but only on the physics inside the resonator.

4.6 Pump-probe measurements

Pump-probe measurements exhibits a unique feature when characterising MRRs, in fact, thanks to the small energy high power optical pulses, it is possible to generate many free carriers inside the ring while keeping the self-heating effect completely negligible, with temperature variation estimated to be on the order of μK. In this section, we retrieve the time resolved transmission spectra of the MRR as it recovers to the linear state after a strong pump pulse has excited the non-linearity. By post-processing the NL loss and the refractive index variation due to FC can be extracted, making it possible to experimentally determine the free carrier density inside the ring. This procedure has been fully carried out for ring resonators $R2$ and $R3$. Whereas in the case of the racetrack resonator $R1$ we were unable to retrieve physically sound NL losses because we used an EDFA to amplify the output signal from the through port [124] since the APD was not available at that time and the signals were too noisy because of EDFA noise. Our model was able to reproduce the experimental results for both resonators $R1$ and $R2$. We remind that the pump pulse width is $100\,ps$ with a period of $25\,\mu s$, in addition we experimentally set the pump pulse in the time axis at approximately $5.1\,ns$ while the time resolved spectra were recorded after $5.4\,ns$. In this way we ensure that TPA and XTPA caused by the pump pulses on the probe traces are all vanished, so that we can then extract information on free carrier dispersion and ultimately the electrons and hole carrier densities in silicon and polysilicon.

4.6.1 Racetrack resonator R1

Results of the pump-probe experiment are summarised in fig. 4.14. Fig. 4.14 (a) and 4.14 (b) show the probe trace as recorded on the oscilloscope. We note how the trace trend depends on the detuning between the probe and cold resonance wavelength, i.e. $\delta\lambda = \lambda_{probe} - \lambda_{0,probe}$. Whereas fig. 4.14 (c) collects respectively the maps of the measured and simulated probe traces at different wavelengths.

Once the pump interacts with the material, a large amount of free carriers are generated resulting in blue shift in the ring resonant wavelength. The upwards or downwards direction of the probe traces in fig. 4.14 (a) and (b) can be understood by looking at the time resolved spectrum in fig. 4.14 (d). This has been obtained by sampling the map of probe traces in fig. 4.14 (c) at several time instants after

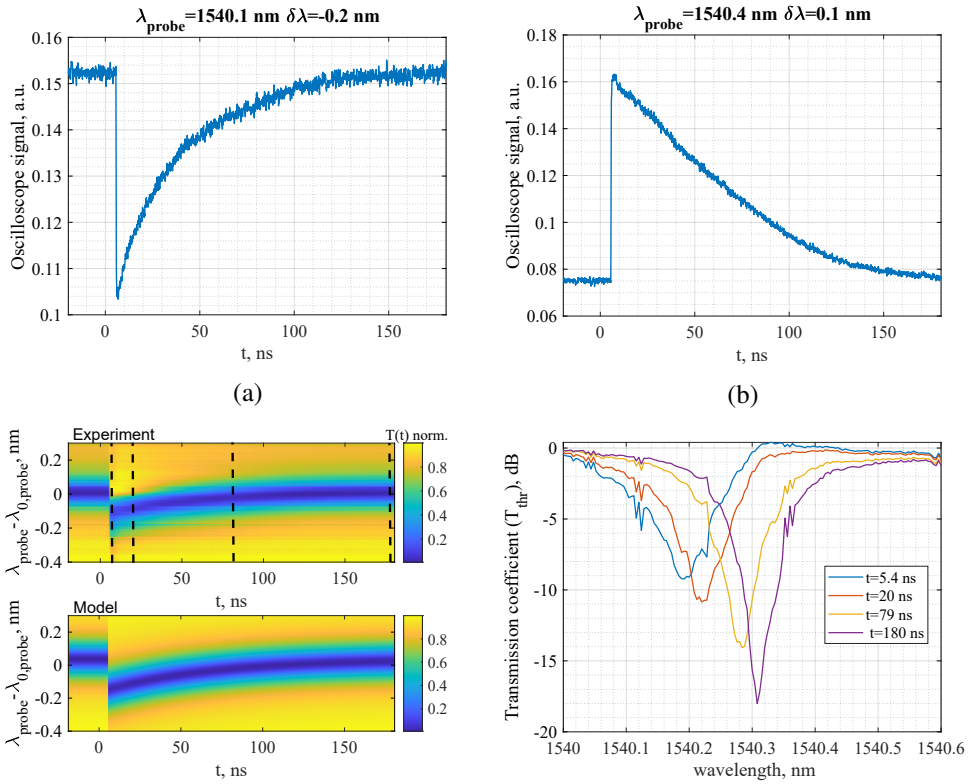

Fig. 4.14 Probe powers traces signals recorded at the oscilloscope at the through port for probe wavelength below (a) and above (b) the cold resonance. (c) Measured (top) and simulated (bottom) probe traces at different wavelengths in the case of a pump pulse with peak power equal to 21 dBm. (d) Transmission spectrum of the ring reconstructed from fig. 4.14 (c) at different time instants after $t = 5.4\,ns$.

the maximum excursions at $5.4\,ns$, as shown for example by the black lines which corresponds to the curves in figure 4.14 (d). We observe the recovery of the ring transmission spectrum from the maximum of the nonlinear response (blue spectrum just after the pump) to the linear response (purple curve). For positive detuning we usually have the upwards shift of the probe trace, see for example $\lambda = 1540.35\,nm$ in fig. 4.14 (d), since the whole spectrum shifts to lower wavelength due to FCD. Whereas for negative detuning the probe trace experiences a downwards shift with a maximum absolute value at approximately $\lambda = 1540.2\,nm$. We note that the model can reproduce very well the experimental map of the probe response (fig. 4.14 (d)), as also shown in fig. 4.15 where we plotted the variation of the resonant wavelength due to FCD in the pump-probe experiment $\Delta\lambda_{PP}(t) = \lambda_{res,probe}(t) - \lambda_{0,probe}$.

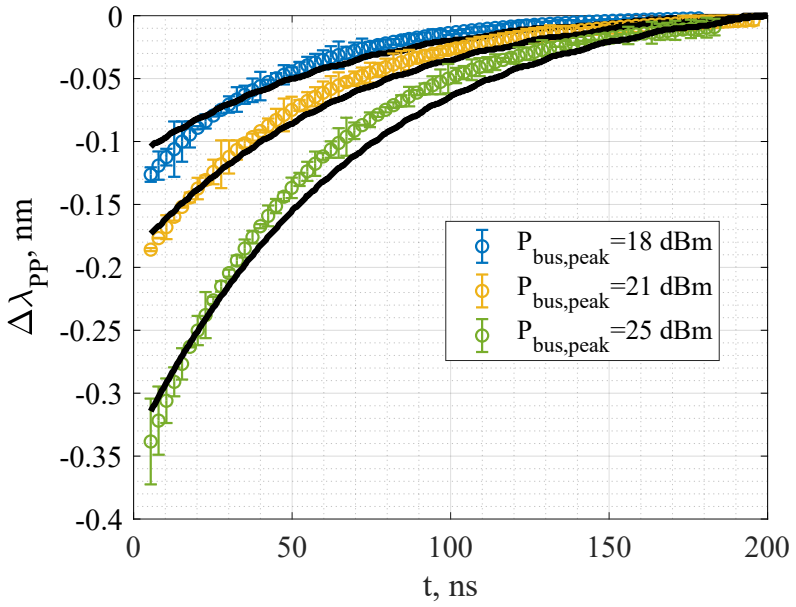

Fig. 4.15 Variation of resonant wavelength extracted from the time resolved transmission spectrum in fig. 4.14 due to FCD for different pulse peak power. The black line represents the model result.

The black lines in fig. 4.15 are the model results obtained by implementing the same experimental procedure with the time domain model developed in section 3.4: we inject a Gaussian pump pulse with $FWHM \approx 100\,ps$ and peak power estimated from the experiment. We then record the different probe transmission responses expressed with eq. (3.53) and finally reconstruct the transmission spectrum at all time instants after the pump has ended. We attribute the small discrepancy between model and experimental results to the additional pump dispersion in the ring, NL EDFA amplification [124] and system misalignment during the total measurements. In fact the time duration of the measurement is sufficiently long ($\approx 20\,minutes$) that the system suffers additional coupling losses with respect to the nominal value due to the environment noise in the laboratory.

4.6.2 Ring resonator R2

We performed pump-probe measurement also on ring $R2$, as explained earlier we were able to use an APD to detect the probe signal from the ring instead of an EDFA coupled with a receiver. This allowed to further characterize the ring dynamics using

a new method based on the empirical relationship between the electron and hole carrier densities and the NL changes in the refractive index and propagation losses in silicon, see eq. (3.5) and (3.7).

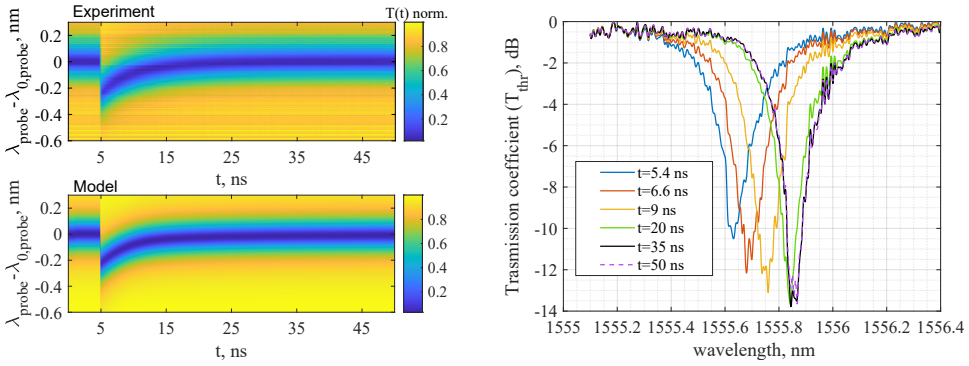

(a) (b)

Fig. 4.16 Measured (top) and simulated (bottom) probe traces at different wavelengths in the case of ring resonator $R2$ and peak power of $18\,dBm$. (b) Transmission spectrum of the ring reconstructed from Fig. 4.16 (a) at different time instants after the pump.

Figure 4.16 collects the trace map (a) and time resolved transmission spectrum associated (b) in the case of a peak bus power of $18\,dBm$. Again the model is able to reproduce very well the experimental map.
By fitting, with the analytical expression of the transmission spectrum of the probe, the spectra measured at the different time instants, we can extract the variation with time of the total optical modal loss ($\alpha_{eff}(t)$) inside the ring, that is the sum of the loss variation due to FCA, and linear losses $\alpha_{0,tot} = \alpha_0 + \alpha_{rad}$; Therefore FCA losses are calculated as $\Delta\alpha_{FCA,exp}(t) = \alpha(t) - \alpha_{0,tot}$. TPA loss of the probe signal in the time range after the pump pulse are negligible because the circulating probe power is low. From the minima of the transmission spectra, we get the variation of the resonant wavelength ($\Delta\lambda_{PP,exp}(t)$) with respect to the linear case and then the variation of the waveguide refractive index due to FCD [151] (see appendix A for proof):

$$\Delta n_{eff,FCD}(t) = \Delta\lambda_{PP}(t) \cdot n_g/\lambda_0. \tag{4.1}$$

The results are shown in fig. 4.17 (a), the black solid lines are the model results in good agreement with the experiments, where we attribute the small mismatch in NL losses between measurements and model to the noise of APD and additional insertion losses in the filter-APD-oscilloscope configuration.

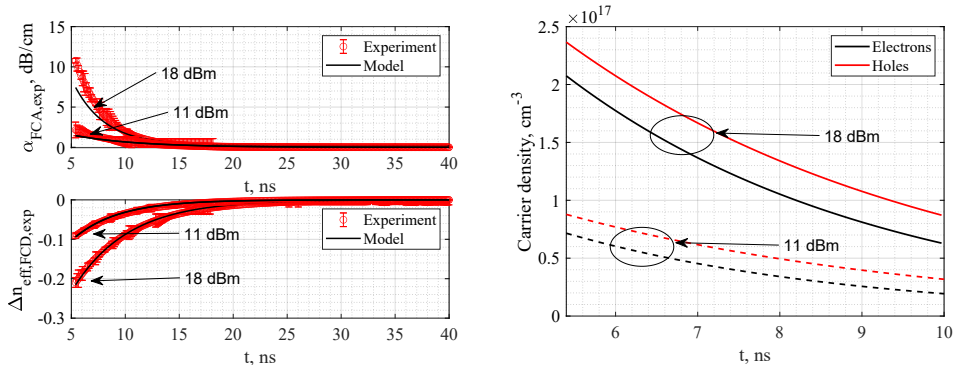

(a) (b)

Fig. 4.17 (a) Variation of nonlinear losses and resonant wavelength due to FCA and FCD for two different pulse peak power extracted from the time resolved transmission spectrum in fig. 4.16 (b); (c) Calculated electron and hole carrier densities versus time.

The variation of the silicon optical loss and refractive index depend on the density of electrons (n_e) and holes (p_e) as expressed in eqs. (3.5) and (3.7). Having measured in fig. 4.17 (a) these variations, we can compute numerically from eqs. (3.5) and (3.7) the electron and hole densities with the constraint $0 < (p_e - n_e)/N_f < 1$ since $(p_e - n_e)/N_f$ is the fraction of occupied traps and cannot be larger than 1, whereas it must be larger than zero following our assumption of donor like traps. Note that this condition is equivalent to the solution $k = 0$ we set in the SRH model in eq.3.16. Results are displayed in fig. 4.17 (b), the difference between electron and hole densities is justified by the respective capture cross section of traps in silicon. By fitting the curve with a single exponential, we can extract the initial electron and hole equivalent lifetimes referred to the first $10ns$ of carrier transient. These are summarized in Table 4.6 and compared to those obtained with our model.

Table 4.6 Experimental and simulated initial electron and hole lifetimes.

$\tau\,[ns]$	Experiment	Theory
$\tau_{n,18dBm}$	3.6 ± 1	2.7
$\tau_{p,18dBm}$	4.35 ± 0.5	5
$\tau_{n,11dBm}$	1.15 ± 0.6	0.83
$\tau_{p,11dBm}$	6.5 ± 0.4	6.4

We refer to these lifetimes as "initial" since in general the lifetimes are carrier dependent: as the carrier density decreases the carrier lifetime tends to change as has been reported also in other studies [134]. This effect is also observed in our

measurements by the initial lifetimes reported in the table at different powers: with higher pump power we generate more free carriers resulting in a reduction of the hole lifetime while the electron lifetime increases with respect to lower peak power case ($P_{bus,peak} = 11\,dBm$). Thus, with the SRH theory, we can determine the nonlinear behaviour of both carriers which ultimately depend on the trap density and trap energy level [58, 88, 135, 152]. Over a larger time window ($t > 10\,ns$), NL effects are too small that the procedure becomes inaccurate. Nonethelees we consider this method a good way to estimate the initial carrier lifetime in a resonator also thanks to the fact that the extracted experimental values are quite close to the theoretical ones as it is possible to see in table 4.6. These values present an uncertainty as indicated in the table arising from the constraint $0 < (p_e - n_e)/N_f < 1$ we used to solve numerically eqs. (3.5) and (3.7). For example considering the case at high power, i.e. $P_{bus,peak} = 18\,dBm$, we repeated the procedure explained above by assuming values for trap densities ranging from $10^{15}\,cm^{-3}$ to $10^{17}\,cm^{-3}$ resulting in an absolute uncertainty of only $\delta\tau_{n,18dBm} = \pm 1\,ns$ and $\delta\tau_{p,18dBm} = \pm 0.5\,ns$ to the associated values reported in table 4.6. We can then assert that this procedure does not require any prior knowledge on the trap density in the material when estimating the initial free carrier lifetime.

4.6.3 Ring resonator R3

With the developed procedure, it is possible to extract the carrier lifetime in materials different than silicon, this is the case of ring $R3$ which is made of two rectangular silicon and polysilicon waveguides. An higher pump peak power of approximately $24\,dBm$ has been injected to excite enough free carries in both Si and poly-Si cores, since coupling losses for ring $R3$ are usually higher than in resonators $R1$ and $R2$ ($4\,dB$ against $2-3\,dB$ typical). The time-resolved transmission spectra are shown in fig. 4.18 (a) as reconstructed from the map of measured probe traces in fig. 4.18 (b). We note that the probe experiences large losses in the first instants after the pump absorption and moderate non-zero losses after $1.5-2\,ns$. Therefore, since the two waveguides are separated by a small gap of SiO_2, and considering that the single silicon waveguide analysis revealed carrier lifetimes longer than $1\,ns$, see table 4.6, we attribute this fast initial transient to the polysilicon material.

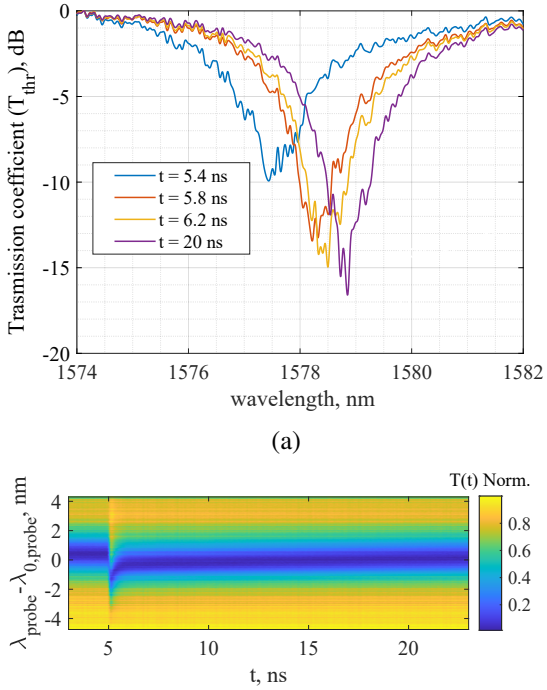

Fig. 4.18 (a) Time-resolved transmission spectra of the Si/poly-Si ring and related probe trace (b). The pump peak power is $P_{bus,peak} \approx 24\,dBm$.

We make use of the optical confinement factors, Γ_{Si} and Γ_{Poly}, in silicon and polysilicon, as reported in table 4.5, to weight the influence of the two waveguides on the propagating field, hence we can write:

$$\Delta\alpha_{FCA,exp}(t) = \Gamma_{Si}(\Delta\alpha_{FCA,exp,Si}(t)) + \Gamma_{poly-Si}(\Delta\alpha_{FCA,exp,poly-Si}(t)). \tag{4.2}$$

Similarly for the variation of refractive index it is:

$$\Delta n_{eff,FCD,exp}(t) = \Gamma_{Si}(\Delta n_{eff,FCD,exp,Si}(t)) + \Gamma_{poly-Si}(\Delta n_{eff,FCD,exp,poly-Si}(t)). \tag{4.3}$$

Where $\Delta\alpha_{FCA,exp,Si}(t)$ and $\Delta\alpha_{FCA,exp,poly-Si}(t)$ are the losses due FCs in the silicon and polysilicon waveguides respectively, while $\Delta n_{eff,FCD,exp,Si}(t)$ and $\Delta n_{eff,FCD,exp,poly-Si}(t)$ the variation of refractive index due to FCD in the two waveguides.

The silicon and polysilicon contributions have been separated by fitting eq. (4.2) and (4.3) with a double exponential function ($y = \Gamma_{Si} a_{Si} e^{-b_{Si} \cdot t} + \Gamma_{poly-Si} a_{poly-Si} e^{-b_{poly-Si} \cdot t}$), results are shown in fig. 4.19 (a).

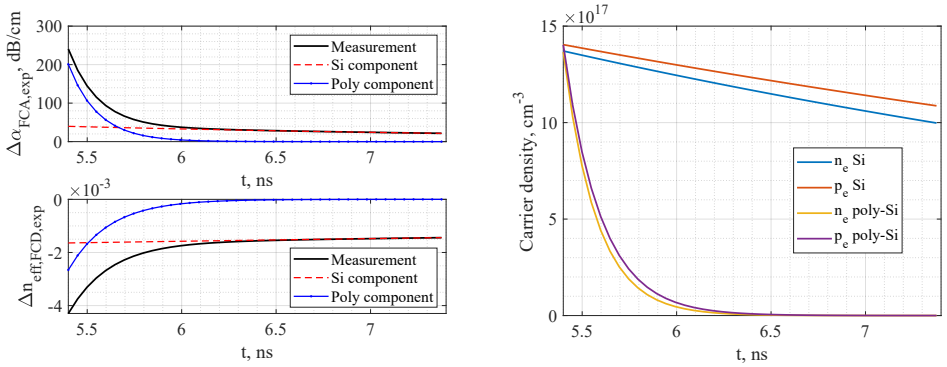

(a) (b)

Fig. 4.19 (a) Losses and refractive index variation in the Si/poly-Si ring recovered from the pump and probe traces with two exponential functions: the blue line is attributed to FC recovery in poly-Si, and the dashed red line to Si. the black line is the total sum of the two. (b) Extracted electron and hole carrier densities in the Si and poly-Si cores.

Assuming that β_{TPA} is equal in both materials, we expect approximately the same number of carriers (generated by TPA) in the Si and poly-Si cores after the pump at $t = 5.4ns$ (i.e., $n_{e,Si}(t = 5.4ns) = n_{e,poly-Si}(t = 5.4ns)$ and $p_{e,Si}(t = 5.4ns) = p_{e,poly-Si}(t = 5.4ns)$). We can use then eq. (3.5) and (3.7) to fit the red dashed curves of the silicon response and retrieve the carrier density in silicon as done for ring resonator $R2$.

FCA coefficients are expected to be larger in poly-Si when compared to crystalline silicon [96, 97, 109–111] since FCA scales, as a first approximation, as $1/\mu_{n,p}$ [59] (with $\mu_{n,p}$ the carrier mobilities) and the mobility in poly-Si is lower depending on the grain size and the number of grain boundaries that populate the material [95]. As a result we should not use eq. (3.5) and (3.7) in polysilicon. For this reason, we take advantage of the initial values of carrier density calculated in silicon at $t = 5.4ns$ to find, from the blue curves at $t = 5.4ns$, the coefficients $A_{poly}, B_{poly}, C_{poly}, D_{poly}$ of the expressions:

$$\Delta\alpha_{FCA,poly} = \Gamma_{poly}\left(A_{poly} n_e^{1.167} + B_{poly} p_e^{1.109}\right), \tag{4.4}$$

$$\Delta n_{eff,FCD,poly} = -\Gamma_{poly}(C_{poly} n_e^{1.011} + D_{poly} p_e^{0.838}). \tag{4.5}$$

The minimization procedure at the initial value $t = 5.4\,ns$ results in $A_{poly} = 5.2 \cdot 10^{-20}\,cm^2$,$B_{poly} = 1.2 \cdot 10^{-19}\,cm^2$,$C_{poly} = 6.6 \cdot 10^{-22}\,cm^3$, and $D_{poly} = 2.4 \cdot 10^{-18}\,cm^3$. We note that the coefficients A_{poly} and B_{poly} are one order of magnitude higher than those of silicon, which means that poly-Si suffers a higher FCA as previously explained.
Fixing these coefficients and using eq. (4.4) and (4.5) for the polysilicon components and eq. (3.5) and (3.7) for silicon, at $t > 5.4\,ns$, we can get the carrier densities dynamics in both materials as reported in fig. 4.19 (b); the extracted initial carrier lifetimes are summarized in Table 4.7. We see that in polysilicon the free carrier

Table 4.7 Experimental initial carrier lifetimes in Si/poly-Si waveguides.

$\tau\,[ns]$	Silicon	polysilicon
τ_n	6.4	0.17
τ_p	7.7	0.2

lifetime is greatly reduced due to the large trap density resulting in reduced free carrier lifetimes. Lastly, we remark that the Si/poly-Si ring we analysed has a measured thermo-optic efficiency of $K_{Si/poly-Si} \approx 75\,pm/K$ which is close to what we obtained for silicon in the same platform, i.e. $K_{Si} = 70\,pm/K$, making it possible to maintain a good tunability, decrease the ring radius, and also have a reduction of NL effects thanks to the smaller lifetime. However the main disadvantage of polysilicon is the larger linear losses caused by grain boundaries and increased trap density with respect to crystalline silicon; for this reason we investigated the hybrid structure of ring $R3$ that is composed of silicon and polysilicon, which results in the contribution of polysilicon to the total linear losses being half of its nominal value.

Chapter 5

Design of microrings for hybrid tunable laser

In this chapter we present two possible applications of our model to the design of the hybrid tunable lasers presented in [87]. First we show that we are able to quantify the maximum power that can enter in the two MRRs to guarantee tuning range covering the C-Band, high SMSR and narrow laser linewidth. Then we introduce the theoretical framework needed for the modelling of a silicon hybrid tunable laser with the inclusion of NL effects of the silicon MRRs.

5.1 Maximisation of the input power in ring resonators

As intensively shown in this thesis, NL effects in silicon MRR pose important limitations to power entering the ring and so to the power the laser can generate. For this reason hybrid tunable laser with Si MRRs and high output power employ an additional semiconductor optical amplifier [87]to reach the same power of lasers where silicon nitride rings are employed (for example as done in [62]).
Therefore we investigate in this section what is the maximum input bus power that a Si microring can handle without a significant degradation of the ring transmission by applying the model we developed for MRRs. The complete model of the hybrid tunable laser, shown in fig. 1.6, was presented in [66] in the case of silicon nitride MRRs. Here we use silicon MRRs with the aim of optimising the ring coupling coefficient in order to have the best trade off between the minimization of NL

effects and the FOMs that characterize the hybrid tunable laser. FOMs of the laser are: the tuning range, the side-mode-suppression-ratio, and the laser linewidth, see Appendix C for additional details. The radii of the two rings (r_1 and r_2) are selected to provide wide tunability based on the Vernier principle [43, 78]. We fix one radius to $r_1 = 20\,\mu m$ since it represents the best compromise between the ring FSR (and therefore tuning range), the maximum temperature increase (related to the thermal tuning of the rings) to cover the FSR and laser SMSR. Then the radius of the second ring is calculated such that the tuning range is sufficient to cover the C-band. We

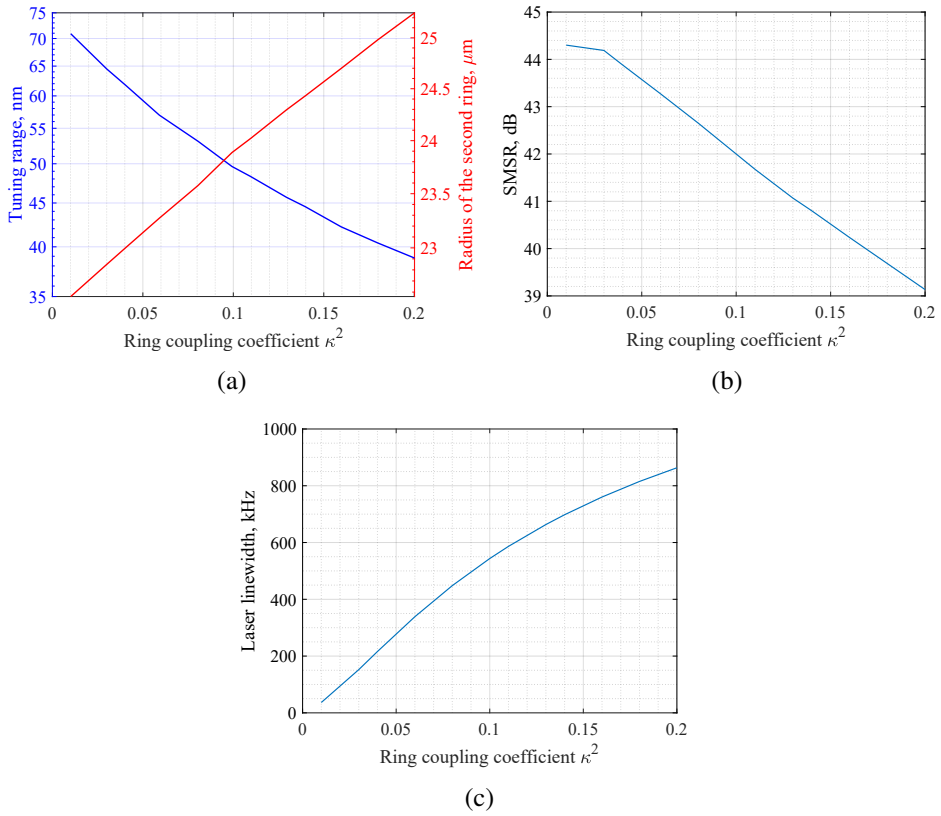

Fig. 5.1 (a) Calculated tuning range and radius of the second ring as a function of the ring coupling coefficient; (b) SMSR and laser linewidth (c) versus the ring coupling coefficient.

report in figure 5.1 (a) the calculated tuning range, (b) the SMSR and (c) the laser linewidth calculated at 4.7 times the threshold current of the laser as function of the ring coupling coefficient in the case the design employs silicon rings similar to ring resonator $R2$ whose parameters are summarised in table 5.1 [58]. Since the ring radius is large enough, bend losses are negligible, i.e., $\alpha_{rad} < 0.01\,dB/cm$. Once κ is chosen r_2 is fixed as it is possible to see in the red curve in fig. 5.1 (a). Looking at fig.

Table 5.1 Parameters and dimension of the ring resonator with radius $r_1 = 20\,\mu m$.

Parameter	Value	Unit
L	125	μm
W	580	nm
h	107	nm
Γ	0.679	–
A_{eff}	0.1089	μm^2
$n_{eff,0}$	1.91	–
n_g	3.38	–
α_0	1.09	dB/cm
η^2	0.002	–

5.1 we note how a small coupling coefficient seems to represent the best strategy for the optimization of all 3 FOMs. For example considering a transition from $\kappa^2 = 0.2$ to $\kappa^2 = 0.1$ the laser linewidth is halved and the tuning range increases by 30%; whereas the SMSR has a maximum excursion of only 12%. Nonetheless, the smaller the coupling coefficient, the more NL effects will occur since the circulating power will increase. We focus our analysis on the ring with radius r_1 since, it is always smaller than the second ring meaning that it will experience a larger circulating power P_c for the same P_{bus} in the ring and so a larger spectral distortion. Therefore we sweep the coupling coefficient in the range reported in figure 5.1 using the steady state model and we calculate the quality factor of the ring as a function of the bus power for three different trap densities, see figure 5.2 (a) and (b). The dashed line indicates where the Q has reduced of 10% with respect to the linear regime value. We note that with decreasing κ^2 the low power quality factor (Q_{LP}) increases which is a consequence of eq. (2.8) that goes as $Q_{LP} \propto 1/\kappa^2$ when $\kappa << 1$ in linear regime [101]. With increasing surface trap density the generated free carriers are more easily trapped resulting in a lower total free carrier density. As a result FCA, FCD and self-heating caused by FCA are reduced, making it possible to send more power into the ring. The maximum power incident in the ring, $P_{bus,max}$, such that the degradation of the ring quality factor does not exceed 10% is displayed in fig. 5.2 (c). In other words,$P_{bus,max}$ determines the maximum power we can extract from the tunable laser in the configuration reported in [66], as expected it increases with increasing κ^2 since the linear quality factor decreases. Thanks to our model, we can quantitatively predict how this maximum depends on the trap density for a fixed trap energy around

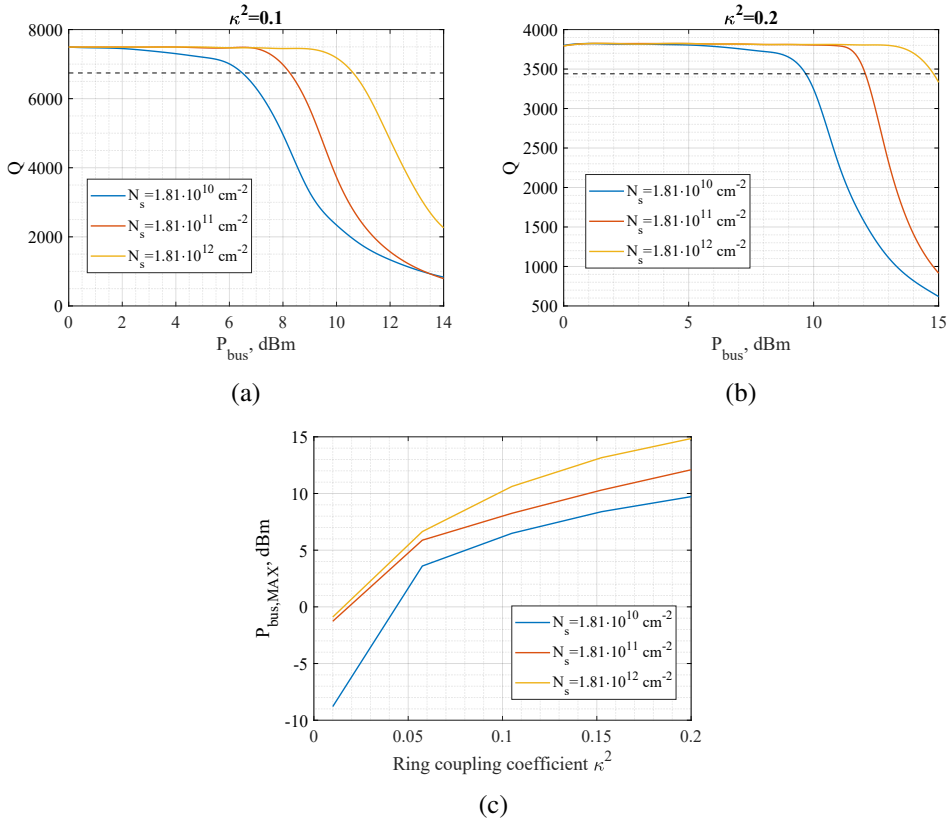

Fig. 5.2 (a) Example of the quality factor degradation versus P_{bus} in the case $\kappa^2 = 0.1$ and for (b) $\kappa^2 = 0.2$, the dashed line represents the reduction of the ring Q-factor to 10%. (c) Maximum allowed bus power as a function of the coupling coefficient and for different surface trap densities (to keep the quality factor degradation to 10%).

the midgap; a possible optimization process would then be based on increasing the density of traps through the implantation of defects [27].

5.2 Silicon hybrid tunable laser model

The previous analysis gives a good insight on how NL effects impact the hybrid tunable laser performances. We remark that in this case we only analysed one ring with our NL model, the next step consists in coupling our time domain model with the hybrid tunable laser theory that was developed in [66, 153]. The most important feature of this approach is to lump the passive mirror physics of the hybrid tunable laser in the so called effective reflectivity r_{eff} of the mirror which is associated to an effective length L_{eff}. In our case we neglect external spurious reflection [153]. For

Table 5.2 Parameters definition for the effective reflectivity in a Si_3N_4 passive mirror.

Parameter	Definition
t_{SSC}	Spot size converter transmission coefficient
$T_{c,out}$	Output power coupling coefficient
$\Delta\omega$	$\omega - \omega_0$
$\Delta\phi$	Phase control section detuning
τ_{in}	Time delay in the Si_3N_4 straight waveguide.
t_{RR}^2	$1 - k_{RR}^2(1-\eta^2)$
$a_{1,2}$	$e^{-\alpha_{eff,1,2}L/2}$
ω_0	Angular reference frequency

this purpose we set our reference plane after the reflective SOA (RSOA) at the AR coating. We first retrieve the effective reflectivity of the mirror and then define the set of differential equations needed to describe the laser dynamic.

Effective reflectivity

The work in [153] reports a compact expression for the effective reflectivity of a Si_3N_4 passive mirror centred at the reference pulsation ω_0, namely:

$$r_{eff}(\omega) = \frac{\gamma_{c1}\gamma_{c2}t_{SSC}^2(1-T_{c,out})}{(\gamma_{t1}+j\Delta\omega)(\gamma_{t2}+j\Delta\omega)} e^{-j\Delta\phi} e^{-j\Delta\omega\tau_{in}}. \tag{5.1}$$

With

$$\gamma_{c1,2} = \frac{v_{g1,2}\kappa_{RR}^2}{2\pi r_{1,2} t_{RR}^2 a_{1,2}^{1/4}} \tag{5.2}$$

$$\gamma_{t1,2} = \frac{v_{g1,2}(1-t_{RR}^2 a_{1,2}^{1/2})}{2\pi r_{1,2} t_{RR}^2 a_{1,2}^{1/2}}. \tag{5.3}$$

All the parameters definitions are summarised in table 5.2.

When silicon is considered inside the two rings, $a_{1,2}$ becomes a function of the circulating power through TPA and FCA. But most importantly, the spectral response of the ring can diverge from the Lorentzian approximation due to FCD and self-heating. This also results in a misalignment of the ring resonances from ω_0, thus eq. (5.1) cannot be used.
We did a first attempt at incorporating NL effects in silicon in [77] where we

considered only NL losses and assumed the NL shift of the resonant wavelenght of the rings to be counteracted by thermal tuning without any bistability. In that work we showed how the implementation of silicon leads to smaller effective length L_{eff} of the passive mirror cavity (and therefore a lower footprint of the hybrid tunable laser) when compared to Si_3N_4, however a small L_{eff} and the presence of NL effects result in a lower maximum external feedback level, i.e., the maximum amount of power received by external sources $R_{ext,max}[dB]$, which the laser can withstand in order to remain stable. In fact at $\kappa_{RR} = 0.04$, the passive mirror made of silicon without considering NL effects has $R_{ext,max,Si} = -25\,dB$, whereas with NL effects it decreases to $R_{ext,max,Si} = -45\,dB$. Which are both much lower than in the case of Si_3N_4 where $R_{ext,max} = -15\,dBm$.
A possible approach to modelling the effective reflectivity in silicon waveguides and MRR should be divided in two stages. First, it is necessary to compute the total circulating power in both rings to evaluate the NL losses and refractive index variation in the ring by FCD and self-heating. Then the complex input field by the SOA can be propagated in the passive mirror and the total backwards component retrieved as influenced by NL effects in both rings and straight waveguides.

The main approach we followed in modelling the nonlinear propagation of the power in the silicon waveguides in [77] is shown in figure 5.3. A waveguide of

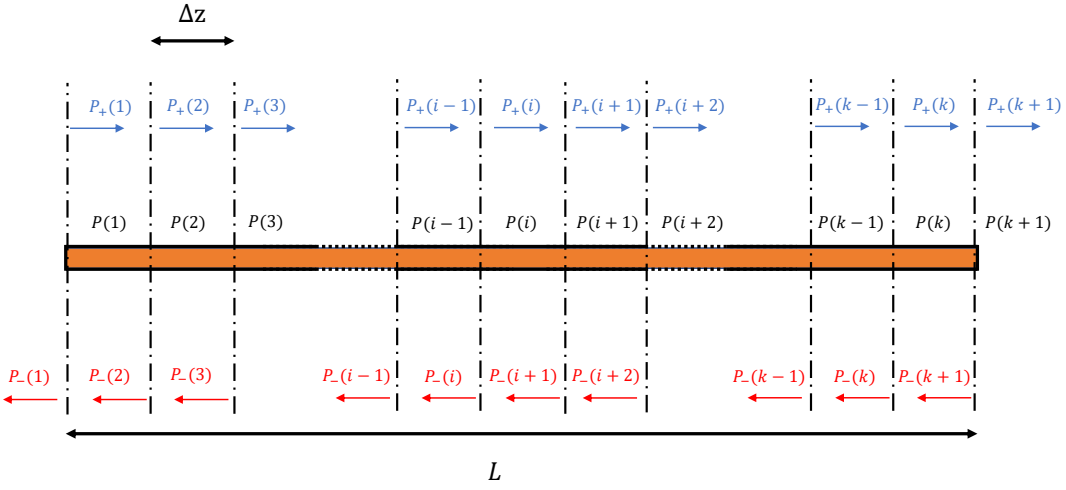

Fig. 5.3 Scheme of the sliced silicon waveguide with length L implemented for the computation of the propagating power as a function of the distance.

length L is divided into k slices with small thickness Δz. Due to the fact that we can have power flowing in both directions due to the splitter configuration, see fig. 1.6,

the total power in each section will be the sum of a forward power $P_+(z)$ entering in that specific slice and a backward outgoing power $P_-(z)$, these are defined as:

$$P_+(i) = P_+(i-1) \cdot e^{-\alpha_{eff}(i-1)\Delta z}, \quad i = 2 : k+1 \tag{5.4}$$

$$P_-(i) = P_-(i+1) \cdot e^{-\alpha_{eff}(i)\Delta z}, \quad i = 1 : k \tag{5.5}$$

since $P_+(1)$ and $P_-(k+1)$ are known, it is possible to solve the system of eq. (5.4) and (5.5) self consistenly and find the power as a function of the position in the waveguide.

The previous method cannot be followed in the case of ring resonator since the refractive index caused by FCD and self-heating impact the ring resonance . Generally the structure we have to analyse is a series of two coupled ring resonators as shown in figure 5.4. We threat the MRRs as lumped object, given the input power in the upper

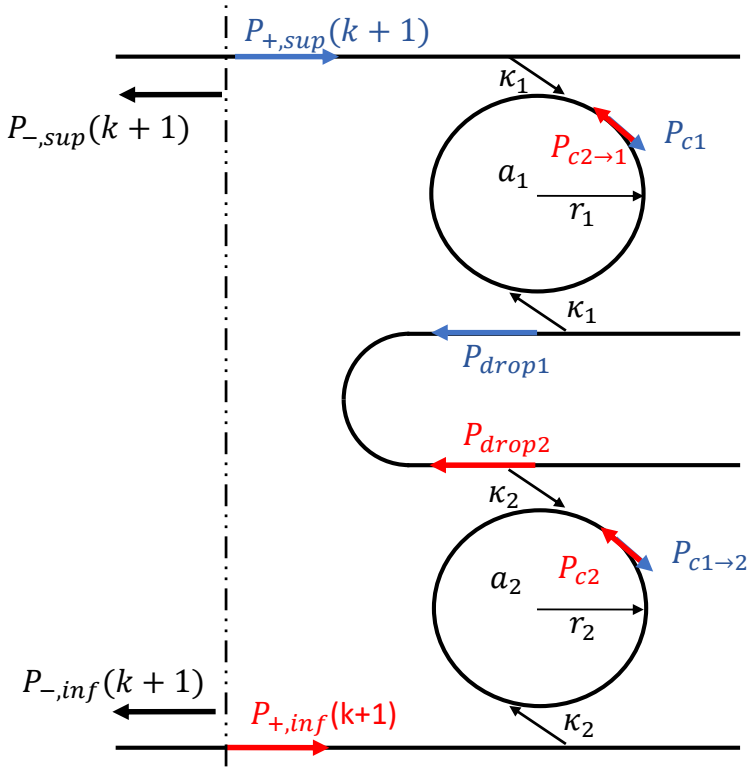

Fig. 5.4 Scheme of the double ring resonator configuration employed in the hybrid tunable laser.

and lower arms as $P_{+,sup}(k+1)$ and $P_{-,sup}(k+1)$ respectively, the total circulating power in both rings is :

$$P_{c1,tot} = (P_{+,sup}(k+1) + a_1 P_{drop2}) \frac{\kappa_1^2(1-\eta^2)}{|1-t_1^2 a_1 e^{j\theta_1}|^2} \tag{5.6}$$

$$P_{c2,tot} = (P_{+,inf}(k+1) a_2 + P_{drop1}) \frac{\kappa_2^2(1-\eta^2)}{|1-t_2^2 a_2 e^{j\theta_2}|^2} \tag{5.7}$$

Where we assume negligible losses in the waveguide between the two rings. We highlight that, $a_1, a_2, \theta_1, \theta_2$ are all expressed in terms of the total circulating power in the respective rings as extensively discussed in this thesis. The power at the drop ports can be computed as $P_{drop1,2} = T_{drop1,2} \cdot P_{+,sup,inf}(k+1)$ with $T_{drop1,2}$ defined in eq. (2.4). Solving equations (5.6) and (5.7) at steady state provides us the amount of refractive index variation and losses impacting the circulating field in both rings as a function of the input power in the upper nd lower arms, i.e., $\alpha_{FC}(P_{+,sup}(k+1), P_{+,inf}(k+1))$, $\Delta n_{eff,FCD}(P_{+,sup}(k+1), P_{+,inf}(k+1))$ and $\Delta n_{eff,T}(P_{+,sup}(k+1), P_{+,inf}(k+1))$. Therefore we can propagate the input field from the SOA, i.e., $E_{+,SOA}(\omega)$, in the passive mirror and compute the backwards reflected field $E_{-,SOA}(\omega, P_{c1,tot}, P_{c2,tot})$ at the SOA facet. The total effective reflectivity is generally written as:

$$r_{eff}(\omega, E_{+,SOA}) = \frac{E_{-,SOA}(\omega, P_{c1,tot}, P_{c2,tot})}{E_{+,SOA}(\omega)}, \tag{5.8}$$

we emphasise that r_{eff} depends on $E_{+,SOA}$ which is related to the circulating powers in the two rings. ω_0 is the reference angular frequency corresponding to the effective reflectivity peak which is the result of the Vernier effect. Since we might have NL effects occurring in the ring, we expect an additional detuning due to NL effects by both MRRs. The new reflectivity peak is then placed at ω_R.
The lasing frequency of the laser is then determined by the round-trip condition inside the RSOA which is [154]:

$$r_{eff}(\omega, E_{+,SOA}) r_1 e^{-2jk_{SOA}(\omega, N_{SOA})L_{SOA}} = 1, \tag{5.9}$$

where r_1 is the reflectivity at the high reflectivity facet of the RSOA, L_{SOA} the SOA length, and $k_{SOA}(\omega, N_{SOA})$ the wave vector of the field inside the SOA which is equal to:

$$k_{SOA}(\omega, N_{SOA}) = \left(\frac{\omega}{c} n_{eff,SOA}(\omega, N) + \frac{j}{2}(\Gamma g_N(\omega, N) - \alpha_i) \right), \tag{5.10}$$

N_{SOA} is the carrier density inside the SOA, $n_{eff,SOA}$ the refractive index in the SOA, g_N the modal gain coefficient, and α_i the intrinsic losses in the SOA. Finally the rate equation for the carrier density in the SOA at steady state is:

$$\frac{\eta_{i,SOA} I_{bias}}{qV_{SOA}} = \frac{N_{SOA}}{\tau_{SOA}} + v_{g,SOA} g_N ln(\frac{N_{SOA}}{N_0}) \sigma_{SOA} \frac{|E_{+,SOA}|^2}{V_{SOA}}, \tag{5.11}$$

where all parameters are defined in table C.1 in Appendix C. By solving the set of coupled equations given by (5.8), (5.9), and (5.11) we can determine the lasing frequency ω_s and associated carrier density N_{SOA}.

Model of the hybrid laser dynamics

The calculation of the effective reflectivity introduced in the previous section is fully general in terms of complexity associated with the number of silicon sections. This is a crucial part, since in a time domain analysis we would need to perform 2D simulation due to the spatial and time dependence on the field propagating in the passive mirror. In this preliminary analysis we remove the spatial dependence by considering that the straight waveguides, SSC,splitter and coupler are made of Si_3N_4, with silicon used only in the MRRs. This scenario is also enforced by the fact that the hybrid tunable laser we plan to test in the laboratory presents this same type of passive mirror composition.
Therefore the laser dynamic can be modelled as done in [153] by defining a set of differential equations at the reference plane at the AR SOA facet just before the passive mirror. The general equations relating the carrier density in the SOA to the output field $E_{+,SOA}(t)$ is:

$$E_{+,SOA}(t) = \frac{e^{j(\omega_s - \omega_R)\tau_{SOA}} exp(f(\omega_s, N_{SOA}))}{r_{eff}(\omega_s)} A^-(t - \tau_{dl}) + F(t). \tag{5.12}$$

$$\frac{\partial N_{SOA}(t)}{\partial t} = \frac{\eta_{i,SOA} I_{bias}}{qV_{SOA}} - \frac{N_{SOA}(t)}{\tau_{SOA}} - v_{g,SOA} g_N ln(\frac{N_{SOA}(t)}{N_0}) \sigma_{SOA} \frac{|E_{+,SOA}(t)|^2}{V_{SOA}}, \tag{5.13}$$

where

$$f(\omega_s, N_{SOA}) = \frac{1}{\tau_{SOA}} \int_{t-\tau_{SOA}}^{t} L_{SOA}(1 + j\alpha_{H,SOA}) \frac{\omega_s}{\omega_R} g_N ln(\frac{N_{SOA}(\hat{t})}{N_s}) d\hat{t}, \tag{5.14}$$

and $F(t)$ accounts for the fraction fo spontaneous emission coupled into the lasing mode s at frequency ω_s. All parameters are defined in table C.1 in Appendix C. $A^-(t-\tau_{dl})$ is the sum of the propaagting fields coming back from the passive mirror with τ_{dl} the total delay in the Si_3N_4 components. In our case it is that:

$$A^-(t-\tau_{dl}) = t_{SSC}(1-T_{c,out})(-E_{-,sup}(1)(t-\tau_{dl}) + E_{-,inf}(1)(t-\tau_{dl})). \quad (5.15)$$

where we used the property $E_{-,sup,inf}(1)(t-\tau_{dl}) = E_{-,sup,inf}(k+1)(t-2\tau_{dl}/2)$. Equations (5.12) and (5.13) must be coupled with the system of equations governing the NL effects dynamics in a double ring resonator structure. In particular we have a total of 4 circulating fields: two clockwise $E_{c,1}$ and $E_{c,2->1}$, with the latter being the circulating field component induced in the bottom ring (ring 2) by top one (ring 1), and two counter-clockwise field components $E_{c,2}$ and $E_{c,1->2}$. In these two cases, we reverse the sign of the input field in the ring so that all 4 circulating field ultimately result to be clockwise. Therefore we will have a total of 4 differential equations for the circulating field. Neglecting again the time delays in the two ring and in the middle waveguide, the clockwise component in the top ring is:

$$\begin{aligned}\frac{\partial E_{c,1}}{\partial t} = -\Big(&\frac{\kappa_1 \cdot \sqrt{1-\eta^2}}{t_1^2 a_1} E_{+,sup}(k+1)(t-\tau_{dl}/2) + \dots \\ &E_{c,1}(t)(\frac{1}{t_1^2 a_1} - 1) + j \cdot (\frac{L}{c}\Delta\omega_{r,1} + \tau_{g1}\delta\omega_{s,1}) \cdot E_{c,1}(t)\Big)/\tau_{g,1},\end{aligned} \quad (5.16)$$

and the counter-clockwise field induced by the bottom ring:

$$\begin{aligned}\frac{\partial E_{c,2->1}}{\partial t} = -\Big(&\frac{\kappa_1 \cdot \sqrt{1-\eta^2}}{t_1^2 a_1} E_{c,2}(a_1^{\frac{1}{2}}\sqrt{1-\eta^2}) \cdot (-\kappa_2)(1 + j \cdot (\frac{L}{c}\Delta\omega_{r,1}/2 + \tau_{g1}\delta\omega_{s,1}/2)) \dots \\ &E_{c,2->1}(t)(\frac{1}{t_1^2 a_1} - 1) + j \cdot (\frac{L}{c}\Delta\omega_{r,1} + \tau_{g1}\delta\omega_{s,1}) \cdot E_{c,2->1}(t)\Big)/\tau_{g,1}.\end{aligned} \quad (5.17)$$

Similarly in ring 2 we have for the clockwise and counter-clockwise components respectively:

$$\frac{\partial E_{c,1->2}}{\partial t} = -\Big(\frac{\kappa_2 \cdot \sqrt{1-\eta^2}}{t_2^2 a_2} E_{c,1}(a_1^{\frac{1}{2}}\kappa_1\sqrt{1-\eta^2})(1+j\cdot(\frac{L}{c}\Delta\omega_{r,1}/2+\tau_{g1}\delta\omega_{s,1}/2))+\dots$$
$$E_{c,1->2}(t)(\frac{1}{t_2^2 a_2}-1)+j\cdot(\frac{L}{c}\Delta\omega_{r,2}+\tau_{g,2}\delta\omega_{s,2})\cdot E_{c,1->2}(t)\Big)/\tau_{g,2}. \tag{5.18}$$

$$\begin{aligned}\frac{\partial E_{c,2}}{\partial t} &= -\Big(\frac{\kappa_2 \cdot \sqrt{1-\eta^2}}{t_2^2 a_2} E_{+,inf}(k+1)(t-\tau_{dl}/2)(a_1^{\frac{1}{2}}\kappa_1\sqrt{1-\eta^2})\cdot\dots \\ &(-1)(1+j\cdot(\frac{L}{c}\Delta\omega_{r,2}/2+\tau_{g1}\delta\omega_{s,2}/2))+\dots \\ &E_{c,2}(t)(\frac{1}{t_2^2 a_2}-1)+j\cdot(\frac{L}{c}\Delta\omega_{r,2}+\tau_{g,2}\delta\omega_{s,2})\cdot E_{c,2->1}(t)\Big)/\tau_{g,2}.\end{aligned} \tag{5.19}$$

with the detuning of the lasing frequency with respect to the cold resonant frequencies of the two ring being $\omega_{s,1,2} = \omega_s - \omega_{0,1,2}$.
Thanks to this formulation, the total circulating power in both ring is simply $P_{c1,tot} = |E_{c,1}|^2 + |E_{c,2->1}|^2$ and $P_{c2,tot} = |E_{c2}|^2 + |E_{c,1->2}|^2$. Which is associated to the generation rate of FC and absorbed power in the ring that follow the same equations introduced in the pump-probe experiment in chapter 3, i.e., equations (3.9), (3.47), (3.13), and (3.20). Finally the backwards fields from the two rings, $E_{-,sup,inf}(k+1)$, are:

$$E_{-,sup}(k+1) = -E_{c,2->1}\kappa_1\sqrt{1-\eta^2}. \tag{5.20}$$

$$E_{-,inf}(k+1) = E_{c,1->2}\kappa_2\sqrt{1-\eta^2}. \tag{5.21}$$

Therefore we can get information on the laser dynamics by solving the system of differential equations: (5.12), (5.13), (5.16), (5.17), (5.18), and (5.19) coupled with eq. (3.13), and (3.47).

Chapter 6

Conclusion

The aim of this dissertation was to present some fundamentals tools, techniques and methods to characterise silicon-based MRRs with the final goal of modelling hybrid tunable laser with NL rings. The growing demand in SiPh based interconnections and compact hybrid tunable laser, where silicon ring resonators represent one of the main components, have been the driving force behind the work of this PhD thesis. To optimise MRRs and reduce the impact of power dependent NL effects in silicon a compact and reliable model is therefore mandatory.

First, electromagnetic and thermal simulations of the device under tests were carried out, which made it possible to retrieve the optical confinement factor of the field inside the ring and the device thermal impedance. These parameters are of great importance when modelling nonlinear effects and when comparing different rings since they directly impact on the strength of FCA,FCD and self-heating.

We then developed the NL model which resulted to be robust in predicting not only the steady state response of MRRs but also the pump-probe experiments and self-oscillations. One of the most important feature of our model is that, thanks to the inclusion of the Shockley–Read–Hall theory, we demonstrate the free carrier lifetime to be strongly dependent on the power circulating in the ring due to trap-assisted recombination. As a result we avoid any empirical expressions for the carrier lifetime as it is common in other works to explain the NL distortion of the ring response. This is an important concept because it allows to design MRRs by changing physically sound parameters such as the trap density or the doping in the rings, which is impossible with empirical lifetimes.

To validate the model we developed an experimental bench that can be used for

steady state and pump-probe characterisation of racetrack and ring resonators in edge and vertical coupling configurations. With the knowledge gained in the study of MRRs, we can summarize the overall process for the full characterization of MRRs in three main steps:

- Linear regime steady state
- NL regime steady state
- Pump-probe experiment

Thanks to the progress we made in the pump-probe setup, we were also able to retrieve the time resolved transmission spectra in nonlinear regime in Si microring resonators excited by strong pump pulses. The analysis of the measured spectra allows the extraction of the absorption and refractive index variation in time. From these two quantities, we have shown that it is possible to study the dynamics of free electrons and holes and their equivalent initial lifetimes. We believe that this tool is of great use since it can quantifies the FC lifetime of MRRs even in structures where other materials with unknown composition are used as we proved in the case of the Si/poly-Si ring resonator. From the analysis of this peculiar ring we have also calculated for the first time the electro-refractive relationship in polysilicon, showing the influence grains have on the latter. To show our model capabilities we also designed a MRR to be employed in the hybrid tunable laser considered in this work using the trap density as a controllable physical parameter, for example through ion implantation.
To conclude, our model proved to be a compact and versatile tool that might be used for the development of silicon based hybrid tunable laser with the aim of overcoming current footprint limitations given by high radius Si_3N_4 ring resonators.

6.1 Future work

One of the natural continuation of this work involves the implementation of the model described in Chapter 5.2 to simulate a tunable hybrid laser with silicon based MRRs. The first step consists in introducing NL effects in the general model, then we will also test the laser stability to an external feedback. At the same time we plan to extend our experimental bench to be able to align a RSOA to a passive mirror and

so manually build the hybrid tunable laser and test it. To this scope we currently have the possibility of implementing passive mirror composed by Si_3N_4 MRRs, silicon MRRs, polysilicon MRRs and hybrid ring such as ring R3 analysed in this thesis. Once we will be able to build the laser and validate the model, we will finally reach the goal of optimising the laser by reducing the FOMs introduced in chapter 6.1.
Another important aspect in the optimization of the MRR is the waveguide geometry, in fact in Chapter 3.3 we presented the theoretical framework behind the modelisation of non-rectangular waveguide where the FC lifetimes are influenced by electrons and holes diffusion in the waveguide. Our goal in this direction is to simulate several waveguides geometries and composition (for example a double rib structure with polysilicon in the upper rib) by solving the drift-diffusion equations on COMSOL and retrieve the NL FOMs as a function of P_c so that we can directly use our lumped model to easily design MRRs.

References

[1] Near Margalit, Chao Xiang, Steven M. Bowers, Alexis Bjorlin, Robert Blum, and John E. Bowers. Perspective on the future of silicon photonics and electronics. *Applied Physics Letters*, 118(22):220501, 2021.

[2] Yaocheng Shi, Yong Zhang, Yating Wan, Yu Yu, Yuguang Zhang, Xiao Hu, Xi Xiao, Hongnan Xu, Long Zhang, and Bingcheng Pan. Silicon photonics for high-capacity data communications. *Photon. Res.*, 10(9):A106–A134, Sep 2022.

[3] S. Y. Siew, B. Li, F. Gao, H. Y. Zheng, W. Zhang, P. Guo, S. W. Xie, A. Song, B. Dong, L. W. Luo, C. Li, X. Luo, and G.-Q. Lo. Review of silicon photonics technology and platform development. *Journal of Lightwave Technology*, 39(13):4374–4389, 2021.

[4] Yichen Shen, Nicholas C. Harris, Scott Skirlo, Mihika Prabhu, Tom Baehr-Jones, Michael Hochberg, Xin Sun, Shijie Zhao, Hugo Larochelle, Dirk Englund, and Marin Soljačić. Deep learning with coherent nanophotonic circuits. *Nature Photonics*, 11(7):441–446, jun 2017.

[5] Christos A. Thraskias, Eythimios N. Lallas, Niels Neumann, Laurent Schares, Bert J. Offrein, Ronny Henker, Dirk Plettemeier, Frank Ellinger, Juerg Leuthold, and Ioannis Tomkos. Survey of photonic and plasmonic interconnect technologies for intra-datacenter and high-performance computing communications. *IEEE Communications Surveys and Tutorials*, 20(4):2758–2783, 2018.

[6] Chao Xiang, Warren Jin, Joel Guo, Coleman Williams, Andrew M. Netherton, Lin Chang, Paul A. Morton, and John E. Bowers. Effects of nonlinear loss in high-q si ring resonators for narrow-linewidth iii-v/si heterogeneously integrated tunable lasers. *Opt. Express*, 28(14):19926–19936, Jul 2020.

[7] Qixiang Cheng, Meisam Bahadori, Madeleine Glick, Sebastien Rumley, and Keren Bergman. Recent advances in optical technologies for data centers: a review. *Optica*, 5(11):1354–1370, Nov 2018.

[8] Mohsen Hayati Shiva Khani. Optical biosensors using plasmonic and photonic crystal band-gap structures for the detection of basal cell cancer. *scientific reports*, 12:5246, 2022.

[9] Michael L. Davenport, Sandra Skendžić, Nicolas Volet, Jared C. Hulme, Martijn J. R. Heck, and John E. Bowers. Heterogeneous silicon/iii–v semiconductor optical amplifiers. *IEEE Journal of Selected Topics in Quantum Electronics*, 22(6):78–88, 2016.

[10] P. Kennedy. Nvidia gtc china 2020 co-packaged photonics and inference. *https://www.servethehome.com/nvidia-gtc-china-2020-co-packaged-photonics-and-inference/*, 13(2):17–26, 2019.

[11] Saeed Fathololoumi, David Hui, Susheel Jadhav, Jian Chen, Kimchau Nguyen, M.N. Sakib, Z. Li, Hari Mahalingam, Siamak Amiralizadeh, Nelson N. Tang, Harinadh Potluri, Mohammad Montazeri, Harel Frish, Reece A. Defrees, Christopher Seibert, Alexander Krichevsky, Jonathan K. Doylend, John Heck, R. Venables, A. Dahal, A. Awujoola, A. Vardapetyan, Guneet Kaur, Min Cen, Vishnu Kulkarni, Syed S. Islam, R. L. Spreitzer, S. Garag, A. C. Alduino, RK Chiou, L. Kamyab, S. Gupta, B. Xie, R. S. Appleton, S. Hollingsworth, S. McCargar, Y. Akulova, K. M. Brown, R. Jones, Daniel Zhu, Thomas Liljeberg, and Ling Liao. 1.6 tbps silicon photonics integrated circuit and 800 gbps photonic engine for switch co-packaging demonstration. *Journal of Lightwave Technology*, 39(4):1155–1161, 2021.

[12] Di Liang, Sudharsanan Srinivasan, Geza Kurczveil, Bassem Tossoun, Stanley Cheung, Yuan Yuan, Antoine Descos, Yingtao Hu, Zhihong Huang, Peng Sun, Thomas Van Vaerenbergh, Chong Zhang, Xiaoge Zeng, Songtao Liu, John E. Bowers, Marco Fiorentino, and Raymond G. Beausoleil. An energy-efficient and bandwidth-scalable dwdm heterogeneous silicon photonics integration platform. *IEEE Journal of Selected Topics in Quantum Electronics*, 28(6: High Density Integr. Multipurpose Photon. Circ.):1–19, 2022.

[13] Chin-Hui Chen, Cheng Li, Rui Bai, Kunzhi Yu, Jean-Marc Fedeli, Sonia Meassoudene, Maryse Fournier, Sylvie Menezo, Patrick Chiang, Samuel Palermo, Marco Fiorentino, and Ray Beausoleil. Dwdm silicon photonic transceivers for optical interconnect. In *2015 IEEE Optical Interconnects Conference (OI)*, pages 52–53, 2015.

[14] Po Dong, Young-Kai Chen, Guang-Hua Duan, and David T. Neilson. Silicon photonic devices and integrated circuits. *Nanophotonics*, 3(4-5):215–228, 2014.

[15] Chen Sun, Mark Wade, Yunsup Lee, Jason Orcutt, Luca Alloatti, Michael Georgas, Andrew Waterman, Jeffrey Shainline, Rimas Avizienis, Sen Lin, Benjamin Moss, R. Kumar, Fabio Pavanello, Amir Atabaki, Henry Cook, Albert Ou, Jonathan Leu, Yu-Hsin Chen, Krste Asanović, and Vladimir Stojanovic. Single-chip microprocessor that communicates directly using light. *Nature*, 528:534–538, 12 2015.

[16] R. Soref. The past, present, and future of silicon photonics. *IEEE J. Sel. Top. Quantum Electron.*, 12(6):1678–1687, 2006.

[17] H. Mekawey, M. Elsayed, Y. Ismail, and M. A. Swillam. Optical interconnects finally seeing the light in silicon photonics: Past the hype. *Nanomaterials*, 12(3), jan 2022.

[18] L. Peh, W. J. Dally, J. D. Owens, S. W. Keckler, D. Jayasimha, and R. Ho. Research challenges for on-chip interconnection networks. *IEEE Micro*, 27(05):96–108, sep 2007.

[19] David Thomson, Aaron Zilkie, John E Bowers, Tin Komljenovic, Graham T Reed, Laurent Vivien, Delphine Marris-Morini, Eric Cassan, Léopold Virot, Jean-Marc Fédéli, Jean-Michel Hartmann, Jens H Schmid, Dan-Xia Xu, Frédéric Boeuf, Peter O'Brien, Goran Z Mashanovich, and M Nedeljkovic. Roadmap on silicon photonics. *Journal of Optics*, 18(7):073003, jun 2016.

[20] Tin Komljenovic, Roger Helkey, Larry Coldren, and John E. Bowers. Sparse aperiodic arrays for optical beam forming and lidar. *Opt. Express*, 25(3):2511–2528, Feb 2017.

[21] Christopher V. Poulton, Ami Yaacobi, David B. Cole, Matthew J. Byrd, Manan Raval, Diedrik Vermeulen, and Michael R. Watts. Coherent solid-state lidar with silicon photonic optical phased arrays. *Opt. Lett.*, 42(20):4091–4094, Oct 2017.

[22] David N. Hutchison, Jie Sun, Jonathan K. Doylend, Ranjeet Kumar, John Heck, Woosung Kim, Christopher T. Phare, Avi Feshali, and Haisheng Rong. High-resolution aliasing-free optical beam steering. *Optica*, 3(8):887–890, Aug 2016.

[23] Yuyao Guo, Xinhang Li, Minhui Jin, Liangjun Lu, Jy Xie, JIANPING CHEN, and Linjie Zhou. Hybrid integrated external cavity laser with a 172-nm tuning range. *APL Photonics*, 7, 05 2022.

[24] Weiqiang Xie, Tin Komljenovic, Jinxi Huang, Minh Tran, Michael Davenport, Alfredo Torres, Paolo Pintus, and John Bowers. Heterogeneous silicon photonics sensing for autonomous cars invited. *Opt. Express*, 27(3):3642–3663, Feb 2019.

[25] Bhavin J. Shastri, Alexander N. Tait, T. Ferreira de Lima, Wolfram H.P. Pernice, Harish Bhaskaran, C. D. Wright, and Paul R. Prucnal. Photonics for artificial intelligence and neuromorphic computing. *Nature Photonics*, 15(2):102–114, February 2021. Funding Information: B.J.S. acknowledges support from the Natural Sciences and Engineering Research Council of Canada (NSERC). T.F.d.L. and P.R.P. acknowledge support from the Office of Naval Research (ONR), Defense Advanced Research Projects Agency (DARPA) and National Science Foundation (NSF). We thank J. Shainline, P. Kuo and N. Sanford for editorial contributions. Publisher Copyright: © 2021, Springer Nature Limited.

[26] Wim Bogaerts, Daniel Perez, José Capmany, David Miller, Joyce Poon, Dirk Englund, Francesco Morichetti, and Andrea Melloni. Programmable photonic circuits. *Nature*, 586:207–216, 10 2020.

[27] Sungbong Park, Koji Yamada, Tai Tsuchizawa, Toshifumi Watanabe, Hiroyuki Shinojima, Hidetaka Nishi, Rai Kou, and Sei ichi Itabashi. Influence of carrier lifetime on performance of silicon p-i-n variable optical attenuators fabricated on submicrometer rib waveguides. *Opt. Express*, 18(11):11282–11291, May 2010.

[28] Quentin Wilmart, Stéphane Brision, Jean-Michel Hartmann, André Myko, Karen Ribaud, Camille Petit-Etienne, Laurene Youssef, Daivid Fowler, Benoit Charbonnier, Corrado Sciancalepore, Erwine Pargon, Stéphane Bernabé, and Bertrand Szelag. A complete si photonics platform embedding ultra-low loss waveguides for o- and c-band. *Journal of Lightwave Technology*, 39(2):532–538, 2021.

[29] M. L. Dakss, L. Kuhn, P. F. Heidrich, and B. A. Scott. Grating Coupler for Efficient Excitation of Optical Guided Waves in Thin Films. *Applied Physics Letters*, 16(12):523–525, June 1970.

[30] T. Tamir and S. T. Peng. Analysis and design of grating couplers. *Applied Physics*, 14(3):235–254, November 1977.

[31] Xin Mu, Sailong Wu, Lirong Cheng, and H.Y. Fu. Edge couplers in silicon photonic integrated circuits: A review. *Applied Sciences*, 10(4), 2020.

[32] Riccardo Marchetti, Cosimo Lacava, Lee Carroll, Kamil Gradkowski, and Paolo Minzioni. Coupling strategies for silicon photonics integrated chips. *Photon. Res.*, 7(2):201–239, Feb 2019.

[33] T. Hiraki, T. Aihara, K.c Hasebe, K. Takeda, T. Fujii, T. Kakitsuka, T. Tsuchizawa, H. Fukuda, and S. Matsuo. Heterogeneously integrated iii–v/si mos capacitor mach–zehnder modulator. *Nature Photonics*, 11:482–485, 2017.

[34] J. Han, F. Boeuf, J. Fujikata, S. Takahashi, S. Takagi, and M. Takenaka. Efficient low-loss ingaasp/si hybrid mos optical modulator. *Nature Photonics*, 11:486–490, 2017.

[35] Alan Y. Liu and John Bowers. Photonic integration with epitaxial iii–v on silicon. *IEEE Journal of Selected Topics in Quantum Electronics*, 24(6):1–12, Nov 2018.

[36] Chun Zhao, G. Z. Li, E.K. Liu, Y. Gao, and Xiaolian Liu. Silicon on insulator mach–zehnder waveguide interferometers operating at 1.3 μm. *Applied Physics Letters*, 67:2448–2449, 1995.

[37] Graham T. Reed and C.E. Jason Png. Silicon optical modulators. *Materials Today*, 8(1):40–50, 2005.

[38] Milos Nedeljkovic, Richard Soref, and Goran Z. Mashanovich. Free-carrier electrorefraction and electroabsorption modulation predictions for silicon over the 1–14-μm infrared wavelength range. *IEEE Photonics Journal*, 3(6):1171–1180, 2011.

[39] Richard A. Soref and Brian R. Bennett. Kramers-kronig analysis of electro-optical switching in silicon. 0704:32 – 37, 1987.

[40] SungWon Chung, Makoto Nakai, and Hossein Hashemi. Low-power thermo-optic silicon modulator for large-scale photonic integrated systems. *Opt. Express*, 27(9):13430–13459, Apr 2019.

[41] Paul E. Barclay, Kartik Srinivasan, and Oskar Painter. Nonlinear response of silicon photonic crystal microresonators excited via an integrated waveguide and fiber taper. *Opt. Express*, 13(3):801–820, Feb 2005.

[42] Stewart A. Clark, Brian Culshaw, Emma J.C. Dawnay, and Ian E. Day. Thermo-optic phase modulators in SIMOX material. In Giancarlo C. Righini and Seppo Honkanen, editors, *Integrated Optics Devices IV*, volume 3936, pages 16 – 24. International Society for Optics and Photonics, SPIE, 2000.

[43] Hang Guan, Ari Novack, Tal Galfsky, Yangjin Ma, Saeed Fathololoumi, Alexandre Horth, Tam N. Huynh, Jose Roman, Ruizhi Shi, Michael Caverley, Yang Liu, Thomas Baehr-Jones, Keren Bergman, and Michael Hochberg. Widely-tunable, narrow-linewidth iii-v/silicon hybrid external-cavity laser for coherent communication. *Opt. Express*, 26(7):7920–7933, Apr 2018.

[44] J. L. Zhao, R. M. Oldenbeuving, J. P. Epping, M. Hoekman, R. G. Heideman, R. Dekker, Y. Fan, K.-J. Boller, R. Q. Ji, S. M. Fu, and L. Zeng. Narrow-linewidth widely tunable hybrid external cavity laser using si3n4/sio2 microring resonators. In *2016 IEEE 13th International Conference on Group IV Photonics (GFP)*, pages 24–25, 2016.

[45] B.E. Little, S.T. Chu, H.A. Haus, J. Foresi, and J.-P. Laine. Microring resonator channel dropping filters. *Journal of Lightwave Technology*, 15(6):998–1005, 1997.

[46] Yuan Yuan, Wayne V. Sorin, Zhihong Huang, Di Liang, Marco Fiorentino, and Raymond G. Beausoleil. A 100 gb/s pam4 two-segment silicon microring resonator modulator. In *2021 IEEE Photonics Conference (IPC)*, pages 1–2, 2021.

[47] Po Dong, Roshanak Shafiiha, Shirong Liao, Hong Liang, Ning-Ning Feng, Dazeng Feng, Guoliang Li, Xuezhe Zheng, Ashok V. Krishnamoorthy, and Mehdi Asghari. Wavelength-tunable silicon microring modulator. *Opt. Express*, 18(11):10941–10946, May 2010.

[48] Sudharsanan Srinivasan, Di Liang, and Raymond G Beausoleil. Heterogeneous siscap microring modulator for high-speed optical communication. In

2020 European Conference on Optical Communications (ECOC), pages 1–3, 2020.

[49] Jifeng Liu, Dong Pan, Samerkhae Jongthammanurak, Kazumi Wada, Lionel C. Kimerling, and Jurgen Michel. Design of monolithically integrated gesi electro-absorption modulators and photodetectors on an soi platform. *Opt. Express*, 15(2):623–628, Jan 2007.

[50] Laurent Vivien, Johann Osmond, Jean-Marc Fedeli, D. Marris-Morini, Paul Crozat, Jean-François Damlencourt, Eric Cassan, Y Lecunff, and Suzanne Laval. 42 ghz p.i.n germanium photodetector integrated in a silicon-on-insulator waveguide. *Optics express*, 17:6252–7, 05 2009.

[51] Daimo Li, Yan Yang, Bin Li, Bo Tang, Peng Zhang, Xiangpeng Ou, Sun Fujun, and Zhihua Li. High-speed and high-power ge-on-si photodetector with bilateral mode-evolution-based coupler. *Photonics*, 10:142, 01 2023.

[52] Hongtao Chen, Peter Verheyen, Peter Heyn, Guy Lepage, Jeroen Coster, P.P. Absil, Gunther Roelkens, and Joris Van Campenhout. High-responsivity low-voltage 28-gb/s ge p-i-n photodetector with silicon contacts. *Journal of Lightwave Technology*, 33:820–824, 02 2015.

[53] Wesley Sacher, Jared Mikkelsen, Ying Huang, Jason Mak, Zheng Yong, Xianshu Luo, Yu Li, Patrick Dumais, Jia Jiang, Dominic Goodwill, Eric Bernier, Patrick Lo, and Joyce Poon. Monolithically integrated multilayer silicon nitride-on-silicon waveguide platforms for 3-d photonic circuits and devices. *Proceedings of the IEEE*, PP:1–14, 08 2018.

[54] Kerstin Wörhoff, René G. Heideman, Arne Leinse, and Marcel Hoekman. Triplex: a versatile dielectric photonic platform. *Advanced Optical Technologies*, 4(2):189–207, 2015.

[55] Armin G. Aberle, Stefan Glunz, and Wilhelm Warta. Impact of illumination level and oxide parameters on shockley–read–hall recombination at the si-sio2 interface. *Journal of Applied Physics*, 71(9):4422–4431, 1992.

[56] G. Priem, P. Dumon, W. Bogaerts, D. Van Thourhout, G. Morthier, and R. Baets. Optical bistability and pulsating behaviour in silicon-on-insulator ring resonator structures. *Opt. Express*, 13(23):9623–9628, Nov 2005.

[57] Qianfan Xu and Michal Lipson. Carrier-induced optical bistability in silicon ring resonators. *Opt. Lett.*, 31(3):341–343, Feb 2006.

[58] Marco Novarese, Sebastian Romero Garcia, Stefania Cucco, Don Adams, Jock Bovington, and Mariangela Gioannini. Study of nonlinear effects and self-heating in a silicon microring resonator including a shockley-read-hall model for carrier recombination. *Opt. Express*, 30(9):14341–14357, Apr 2022.

[59] Q. Lin, Oskar J. Painter, and Govind P. Agrawal. Nonlinear optical phenomena in silicon waveguides: Modeling and applications. *Opt. Express*, 15(25):16604–16644, Dec 2007.

[60] Mihaela Dinu, Francesco Quochi, and Hernando Garcia. Third-order nonlinearities in silicon at telecom wavelengths. *Applied Physics Letters*, 82:2954 – 2956, 06 2003.

[61] Jörn P. Epping, Arne Leinse, Ruud M. Oldenbeuving, Ilka Visscher, Douwe Geuzebroek, Dimitri Geskus, Albert van Rees, Klaus J. Boller, Michael Theurer, Martin Möhrle, Martin Schell, Chris G. H. Roeloffzen, and René G. Heideman. Hybrid integrated silicon nitride lasers. In Bernd Witzigmann, Marek Osiński, and Yasuhiko Arakawa, editors, *Physics and Simulation of Optoelectronic Devices XXVIII*, volume 11274, page 112741L. International Society for Optics and Photonics, SPIE, 2020.

[62] Youwen Fan, Albert van Rees, Peter J. M. van der Slot, Jesse Mak, Ruud M. Oldenbeuving, Marcel Hoekman, Dimitri Geskus, Chris G. H. Roeloffzen, and Klaus-J. Boller. Hybrid integrated inp-si3n4 diode laser with a 40-hz intrinsic linewidth. *Opt. Express*, 28(15):21713–21728, Jul 2020.

[63] J. C. Hulme, J. K. Doylend, and J. E. Bowers. Widely tunable vernier ring laser on hybrid silicon. *Opt. Express*, 21(17):19718–19722, Aug 2013.

[64] Changjin Yang, Lei Liang, Li Qin, Hui Tang, Yuxin Lei, Peng Jia, Yongyi Chen, Yubing Wang, Yu Song, Cheng Qiu, Chuantao Zheng, Huan Zhao, Xin Li, Dabing Li, and Lijun Wang. Advances in silicon-based, integrated tunable semiconductor lasers. *Nanophotonics*, 12, 01 2023.

[65] Aditya Malik, Songtao Liu, Erman Timurdogan, Mark Harrington, Andrew Netherton, Mitra Saeidi, Daniel J. Blumenthal, Luke Theogarajan, Michael Watts, and John E. Bowers. Low power consumption silicon photonics datacenter interconnects enabled by a parallel architecture. In *2021 Optical Fiber Communications Conference and Exhibition (OFC)*, pages 1–3, 2021.

[66] Lorenzo Columbo, Jock Bovington, Sebastian Romero-Garcia, Dominic F. Siriani, and Mariangela Gioannini. Efficient and optical feedback tolerant hybrid laser design for silicon photonics applications. *IEEE Journal of Selected Topics in Quantum Electronics*, 26(2):1–10, 2020.

[67] Théo Verolet, Antonin Gallet, Xavier Pommarède, Jean Decobert, Dalila Make, Jean-Guy Provost, Maryse Fournier, Christophe Jany, Ségolène Olivier, Alexandre Shen, and Guanghua Duan. Hybrid iii-v on silicon fast and widely tunable laser based on rings resonators with pin junctions. In *2018 Asia Communications and Photonics Conference (ACP)*, pages 1–3, 2018.

[68] Chong Zhang, Di Liang, Cheng Li, Geza Kurczveil, John E. Bowers, and Raymond G. Beausoleil. High-speed hybrid silicon microring lasers. In *2015 IEEE 58th International Midwest Symposium on Circuits and Systems (MWSCAS)*, pages 1–4, 2015.

[69] Takuma Aihara, Tatsurou Hiraki, Takuro Fujii, Koji Takeda, Tai Tsuchizawa, Takaaki Kakitsuka, Hiroshi Fukuda, and Shinji Matsuo. Heterogeneously integrated widely tunable laser using lattice filter and ring resonator on si photonics platform. *Opt. Express*, 30(10):15820–15829, May 2022.

[70] Tin Komljenovic, Michael Davenport, Jared Hulme, Alan Y. Liu, Christos T. Santis, Alexander Spott, Sudharsanan Srinivasan, Eric J. Stanton, Chong Zhang, and John E. Bowers. Heterogeneous silicon photonic integrated circuits. *Journal of Lightwave Technology*, 34(1):20–35, 2016.

[71] Naoki Kobayashi, Kenji Sato, Masahiko Namiwaka, Keisuke Yamamoto, Shinya Watanabe, Tomohiro Kita, Hirohito Yamada, and Hiroyuki Yamazaki. Silicon photonic hybrid ring-filter external cavity wavelength tunable lasers. *Journal of Lightwave Technology*, 33:1241–1246, 03 2015.

[72] Yongkang Gao, Jiann-Chang Lo, Shing Lee, Ronak Patel, Likai Zhu, Jocelyn Nee, Diana Tsou, Rob Carney, and Jibin Sun. High-power, narrow-linewidth, miniaturized silicon photonic tunable laser with accurate frequency control. *Journal of Lightwave Technology*, 38(2):265–271, 2020.

[73] Tomohiro Kita, Rui Tang, and Hirohito Yamada. Compact silicon photonic wavelength-tunable laser diode with ultra-wide wavelength tuning range. *Applied Physics Letters*, 106(11):111104, 2015.

[74] Paul A. Morton, Chao Xiang, Jacob B. Khurgin, Christopher D. Morton, Minh Tran, Jon Peters, Joel Guo, Michael J. Morton, and John E. Bowers. Integrated coherent tunable laser (ictl) with ultra-wideband wavelength tuning and sub-100 hz lorentzian linewidth. *J. Lightwave Technol.*, 40(6):1802–1809, Mar 2022.

[75] Minh A. Tran, Duanni Huang, and John E. Bowers. Tutorial on narrow linewidth tunable semiconductor lasers using si/iii-v heterogeneous integration. *APL Photonics*, 4(11):111101, 2019.

[76] Yating Wan, Sen Zhang, Justin C. Norman, M. J. Kennedy, William He, Songtao Liu, Chao Xiang, Chen Shang, Jian-Jun He, Arthur C. Gossard, and John E. Bowers. Tunable quantum dot lasers grown directly on silicon. *Optica*, 6(11):1394–1400, Nov 2019.

[77] M. Gioannini, L. Columbo, A. Bologna, S. R.Garcia M. Novarese, and J. Bovington D. Siriani. Design of hybrid lasers for silicon photonics: efficiency, optical feedback tolerance and laser dynamics. *European Conference on Integrated Optics ECIO 2020*, 2020.

[78] Yingxuan Liu, Xuegang Li, Ya nan Zhang, and Yong Zhao. Fiber-optic sensors based on vernier effect. *Measurement*, 167:108451, 2021.

[79] Liwei Tang, Jiachen Li, Sigang Yang, Hongwei Chen, and Minghua Chen. A method for improving reflection tolerance of laser source in hybrid photonic

packaged micro-system. *IEEE Photonics Technology Letters*, 33(9):465–468, 2021.

[80] Dan Yi, Xinru Wu, and Hon Ki Tsang. Ultra-compact polarization analyzer based on micro-ring resonators. *IEEE Photonics Technology Letters*, 33(24):1371–1374, 2021.

[81] Matteo Petrini, Maziyar Milanizadeh, Francesco Zanetto, Giorgio Ferrari, Marco Sampietro, Francesco Morichetti, and Andrea Melloni. Reconfigurable fsr-free microring resonator filter with wide hitless tunability. In *2021 IEEE Photonics Society Summer Topicals Meeting Series (SUM)*, pages 1–2, 2021.

[82] Tymon Barwicz, Miloš A. Popovic, Peter T. Rakich, Michael R. Watts, Hermann A. Haus, Erich P. Ippen, and Henry I. Smith. Microring-resonator-based add-drop filters in sin: fabrication and analysis. *Opt. Express*, 12(7):1437–1442, Apr 2004.

[83] Desheng Zeng, Qiang Liu, Chenyang Mei, Hongwei Li, Qingzhong Huang, and Xinliang Zhang. Demonstration of ultra-high-q silicon microring resonators for nonlinear integrated photonics. *Micromachines*, 13(7), 2022.

[84] W. Bogaerts, P. De Heyn, T. Van Vaerenbergh, K. De Vos, S. Kumar Selvaraja, T. Claes, P. Dumon, P. Bienstman, D. Van Thourhout, and R. Baets. Silicon microring resonators. *Laser & Photonics Reviews*, 6(1):47–73, 2012.

[85] Bradley J. Frey, Douglas B. Leviton, and Timothy J. Madison. Temperature-dependent refractive index of silicon and germanium. In Eli Atad-Ettedgui, Joseph Antebi, and Dietrich Lemke, editors, *Optomechanical Technologies for Astronomy*, volume 6273, pages 790 – 799. International Society for Optics and Photonics, SPIE, 2006.

[86] Hani Nejadriahi, Alex Friedman, Rajat Sharma, Steve Pappert, Yeshaiahu Fainman, and Paul Yu. Thermo-optic properties of silicon-rich silicon nitride for on-chip applications. *Opt. Express*, 28(17):24951–24960, Aug 2020.

[87] Yongkang Gao, Jiann-Chang Lo, Shing Lee, Ronak Patel, Likai Zhu, Jocelyn Nee, Diana Tsou, Rob Carney, and Jibin Sun. High-power, narrow-linewidth, miniaturized silicon photonic tunable laser with accurate frequency control. *Journal of Lightwave Technology*, 38(2):265–271, 2020.

[88] Marco Novarese, Sebastian Romero Garcia, Don Adams, Jock Bovington, and Mariangela Gioannini. Study of nonlinear effects and self-heating in silicon microring resonator including SRH model for carrier recombination. In Graham T. Reed and Andrew P. Knights, editors, *Silicon Photonics XVII*, volume 12006, page 120060G. International Society for Optics and Photonics, SPIE, 2022.

[89] Amy C. Turner, Mark A. Foster, Alexander L. Gaeta, and Michal Lipson. Ultra-low power parametric frequency conversion in a silicon microring resonator. *Opt. Express*, 16(7):4881–4887, Mar 2008.

[90] Dan Yi, Xinru Wu, and Hon Ki Tsang. Ultra-compact polarization analyzer based on micro-ring resonators. *IEEE Photonics Technology Letters*, 33(24):1371–1374, 2021.

[91] Andrey A. Nikitin, Ilya A. Ryabcev, Aleksei A. Nikitin, Alexandr V. Kondrashov, Alexander A. Semenov, Dmitry A. Konkin, Andrey A. Kokolov, Feodor I. Sheyerman, Leonid I. Babak, and Alexey B. Ustinov. Optical bistable soi micro-ring resonators for memory applications. *Optics Communications*, 511:127929, 2022.

[92] Yuan Yuan, Wayne V. Sorin, Zhihong Huang, Xiaoge Zeng, Di Liang, Ankur Kumar, Samuel Palermo, Marco Fiorentino, and Raymond G. Beausoleil. A 100 gb/s pam4 two-segment silicon microring resonator modulator using a standard foundry process. *ACS Photonics*, 9(4):1165–1171, 2022.

[93] Michael Waldow, Tobias Plötzing, Martin Gottheil, Michael Först, Jens Bolten, Thorsten Wahlbrink, and Heinrich Kurz. 25ps all-optical switching in oxygen implanted silicon-on-insulator microring resonator. *Opt. Express*, 16(11):7693–7702, May 2008.

[94] Kyle Preston, Po Dong, Bradley Schmidt, and Michal Lipson. High-speed all-optical modulation using polycrystalline silicon microring resonators. *Applied Physics Letters*, 92(15):151104, 2008.

[95] John Y. W. Seto. The electrical properties of polycrystalline silicon films. *Journal of Applied Physics*, 46(12):5247–5254, 1975.

[96] J. Martinez and J. Piqueras. On the mobility of polycrystalline semiconductors. *Solid State Electronics*, 23(4):297–303, April 1980.

[97] D. P. Joshi and R. S. Srivastava. Mobility and carrier concentration in polycrystalline silicon. *Solar Cells*, 12:337–344, August 1984.

[98] Marco Novarese, Sebastian Romero-Garcia, Jock Bovington, and Mariangela Gioannini. Dynamics of free carrier absorption and refractive index dispersion in si and si/polysi microrings. *IEEE Photonics Technology Letters*, 35(8):450–453, 2023.

[99] Chih-Wei Tseng, Chih-Wei Tsai, Kaung-Cheng Lin, Ming-Chang Lee, and Yung-Jui Chen. Study of coupling loss on strongly-coupled, ultra compact microring resonators. *Opt. Express*, 21(6):7250–7257, Mar 2013.

[100] Andres Gil-Molina, Ivan Aldaya, Julián L. Pita, Lucas H. Gabrielli, Hugo L. Fragnito, and Paulo Dainese. Optical free-carrier generation in silicon nanowaveguides at 1550*nm*. *Applied Physics Letters*, 112(25):251104, 2018.

[101] Dominik G. Rabus. *Integrated Ring Resonators*. Dover Books on Physics Series. Springer-Verlag Berlin Heidelberg, 2007.

[102] Calvin D. Salzberg and John J. Villa. Infrared refractive indexes of silicon germanium and modified selenium glass∗. *J. Opt. Soc. Am.*, 47(3):244–246, Mar 1957.

[103] A Sv Sudbo. Film mode matching: a versatile numerical method for vector mode field calculations in dielectric waveguides. *Pure and Applied Optics: Journal of the European Optical Society Part A*, 2(3):211–233, may 1993.

[104] Daniel de zutter, P. Lagasse, J. Buus, T. Young, and Bernice Dillon. Comparison of different modelling techniques for longitudinally invariant integrated optical waveguides. *IEE Proceedings J: Optoelectronics*, pages 273–280, 10 1989.

[105] Henry Frankis, Khadijeh Miarabbas Kiani, Daniel Su, Richard Mateman, Arne Leinse, and Jonathan Bradley. High-q tellurium-oxide-coated silicon nitride microring resonators. *Optics Letters*, 44:118, 01 2019.

[106] Christopher J Kaalund. Critically coupled ring resonators for add-drop filtering. *Optics Communications*, 237(4):357–362, 2004.

[107] M. Webster, C. Appel, P. Gothoskar, S. Sunder, B. Dama, and K. Shastri. Silicon photonic modulator based on a mos-capacitor and a cmos driver. In *2014 IEEE Compound Semiconductor Integrated Circuit Symposium (CSICS)*, pages 1–4, 2014.

[108] Christina Manolatou and Michal Lipson. All-optical silicon modulators based on carrier injection by two-photon absorption. *J. Lightwave Technol.*, 24(3):1433, Mar 2006.

[109] Amal K. Ghosh, Charles Fishman, and Tom Feng. Theory of the electrical and photovoltaic properties of polycrystalline silicon. *Journal of Applied Physics*, 51(1):446–454, 1980.

[110] Y. Laghla and E. Scheid. Optical study of undoped, b or p-doped polysilicon. *Thin Solid Films*, 306(1):67–73, 1997.

[111] Navneet Gupta and B Tyagi. Effect of grain size on the mobility and transfer characteristics of polysilicon thin-film transistors. *Indian Journal of Pure and Applied Physics*, 42, 07 2004.

[112] A.D. McConnell, S. Uma, and K.E. Goodson. Thermal conductivity of doped polysilicon layers. *Journal of Microelectromechanical Systems*, 10(3):360–369, 2001.

[113] S. Pizzini. Polycrystalline silicon as against amorphous silicon for photovoltaic applications: A subject for speculation and a challenge for the late 1980s. *Solar Cells*, 12(1):163–165, 1984.

[114] Ted Kamins. *Polycrystalline Silicon for Integrated Circuits and Displays Second Edition*. Dover Books on Physics Series. Kluwer Academic Publishers, 1998.

[115] A.S. Sudbo. Numerically stable formulation of the transverse resonance method for vector mode-field calculations in dielectric waveguides. *IEEE Photonics Technology Letters*, 5(3):342–344, 1993.

[116] C. Vassallo and J.M. van der Keur. Comparison of a few transparent boundary conditions for finite-difference optical mode-solvers. *Journal of Lightwave Technology*, 15(2):397–402, 1997.

[117] C. Koos, L. Jacome, C. Poulton, J. Leuthold, and W. Freude. Nonlinear silicon-on-insulator waveguides for all-optical signal processing. *Opt. Express*, 15(10):5976–5990, May 2007.

[118] Jacob T. Robinson, Kyle Preston, Oskar Painter, and Michal Lipson. First-principle derivation of gain in high-index-contrast waveguides. *Opt. Express*, 16(21):16659–16669, Oct 2008.

[119] T.D. Visser, H. Blok, B. Demeulenaere, and D. Lenstra. Confinement factors and gain in optical amplifiers. *IEEE Journal of Quantum Electronics*, 33(10):1763–1766, 1997.

[120] Ivan D. Rukhlenko, Malin Premaratne, and Govind P. Agrawal. Effective mode area and its optimization in silicon-nanocrystal waveguides. *Opt. Lett.*, 37(12):2295–2297, Jun 2012.

[121] Tsutomu Satō. Spectral emissivity of silicon. *Japanese Journal of Applied Physics*, 6(3):339, mar 1967.

[122] Mohammad Soltani. *Novel Integrated Silicon Nanophotonic Structures using Ultra-high Q Resonators*. PhD thesis, School of Electrical and Computer Engineering Georgia Institute of Technology, 2009.

[123] Thomas Johnson. *Silicon Microdisk Resonators for Nonlinear Optics and Dynamics*. PhD thesis, California Institute of Technology, 2009.

[124] Jason S. Pelc, Kelley Rivoire, Sonny Vo, Charles Santori, David A. Fattal, and Raymond G. Beausoleil. Picosecond all-optical switching in hydrogenated amorphous silicon microring resonators. *Opt. Express*, 22(4):3797–3810, Feb 2014.

[125] Schütze. Thermal equivalent circuit models. application note. v1.0. *Infineon Technologies AG*, 2008.

[126] Mohammad Soltani, Qing Li, Siva Yegnanarayanan, and Ali Adibi. Improvement of thermal properties of ultra-high q silicon microdisk resonators. *Opt. Express*, 15(25):17305–17312, Dec 2007.

[127] T. K. Liang and H. K. Tsang. Role of free carriers from two-photon absorption in raman amplification in silicon-on-insulator waveguides. *Applied Physics Letters*, 84(15):2745–2747, 2004.

[128] Stefano Grillanda and Francesco Morichetti. Light-induced metal-like surface of silicon photonic waveguides. *Nature Communications*, 6(25), 2015.

[129] Nobuyuki Matsuda, Ryosuke Shimizu, Yasuyoshi Mitsumori, Hideo Kosaka, Aya Sato, Hiroyuki Yokoyama, Koji Yamada, Toshifumi Watanabe, Tai Tsuchizawa, Hiroshi Fukuda, Seiichi Itabashi, and Keiichi Edamatsu. All-optical phase modulations in a silicon wire waveguide at ultralow light levels. *Applied Physics Letters*, 95(17):171110, 2009.

[130] Yanbing Zhang, Chad Husko, Simon Lefrancois, Isabella H. Rey, Thomas F. Krauss, Jochen Schröder, and Benjamin J. Eggleton. Non-degenerate two-photon absorption in silicon waveguides: analytical and experimental study. *Opt. Express*, 23(13):17101–17110, Jun 2015.

[131] Alan D. Bristow, Nir Rotenberg, and Henry M. van Driel. Two-photon absorption and kerr coefficients of silicon for 850–2200nm. *Applied Physics Letters*, 90(19):191104, 2007.

[132] Massimo Borghi, Davide Bazzanella, Mattia Mancinelli, and Lorenzo Pavesi. On the modeling of thermal and free carrier nonlinearities in silicon-on-insulator microring resonators. *Opt. Express*, 29(3):4363–4377, Feb 2021.

[133] Mansoor Sheik-Bahae and Eric W. van Stryland. Chapter 4 - optical nonlinearities in the transparency region of bulk semiconductors. *Semiconductors and Semimetals*, 58, 1998.

[134] I. Aldaya, A. Gil-Molina, J. L. Pita, L. H. Gabrielli, H. L. Fragnito, and P. Dainese. Nonlinear carrier dynamics in silicon nano-waveguides. *Optica*, 4(10):1219–1227, Oct 2017.

[135] J.S. Blakemore. *Semiconductor Statistics*. Dover Books on Physics Series. Dover, 2002.

[136] ioffe.ru. Electrical properties of silicon(si).

[137] D. Dimitropoulos, R. Jhaveri, R. Claps, J. C. S. Woo, and B. Jalali. Lifetime of photogenerated carriers in silicon-on-insulator rib waveguides. *Applied Physics Letters*, 86(7):071115, 2005.

[138] G. Ghione. *dispositivi per la microelettronica*. McGraw-Hill Libri Italia srl, 1997.

[139] P.E. owers and J.W. Haus. *Fundamentals of Nonlinear Optics (2nd ed.)*. CRC Press, 2017.

[140] H. Kogelnik. *Theory of Optical Waveguides*, pages 7–88. Springer Berlin Heidelberg, Berlin, Heidelberg, 1988.

[141] L. A. Coldren and S. Corzine. *Semiconductor lasers and Photonic Integrated Circuits*. Wiley, NY, USA, 1995.

[142] Martin Adams, Simon Rauch, Carlo Holly, Martin Traub, and Hans-Dieter Hoffmann. Modeling of the impact of current crowding on catastrophic optical damage in 9xx-nm high power laser diodes. page 9, 03 2021.

[143] Martin Adams, Carlo Holly, Simon Rauch, and Martin Traub. Gpu-accelerated wave-optical model for external-cavity diode lasers. *Opt. Lett.*, 46(7):1780–1783, Apr 2021.

[144] Gregory Moille, Sylvain Combrié, and Alfredo De Rossi. Modeling of the carrier dynamics in nonlinear semiconductor nanoscale resonators. *Phys. Rev. A*, 94:023814, Aug 2016.

[145] Y. Mishima, M. Hirose, and Y. Osaka. Optical determination of mobility and carrier concentration in heavily doped polycrystalline silicon. *Journal of Applied Physics*, 51(2):1157–1159, 1980.

[146] Brent E. Little, Juha-Pekka Laine, and Sai T. Chu. Surface-roughness-induced contradirectional coupling in ring and disk resonators. *Opt. Lett.*, 22(1):4–6, Jan 1997.

[147] Karan K. Mehta, Jason S. Orcutt, Jeffrey M. Shainline, Ofer Tehar-Zahav, Zvi Sternberg, Roy Meade, Miloš A. Popović, and Rajeev J. Ram. Polycrystalline silicon ring resonator photodiodes in a bulk complementary metal-oxide-semiconductor process. *Opt. Lett.*, 39(4):1061–1064, Feb 2014.

[148] Philip J. Caplan, Edward H. Poindexter, Bruce E. Deal, and Reda R. Razouk. Esr centers, interface states, and oxide fixed charge in thermally oxidized silicon wafers. *Journal of Applied Physics*, 50(9):5847–5854, 1979.

[149] E. Hendry, M. Koeberg, J. Pijpers, and M. Bonn. Reduction of carrier mobility in semiconductors caused by charge-charge interactions. *Phys. Rev. B*, 75:233202, Jun 2007.

[150] Masatoshi Tokushima, Jun Ushida, and Takahiro Nakamura. Nonlinear loss characterization of continuous wave guiding in silicon wire waveguides. *Applied Physics Express*, 14(12):122008, dec 2021.

[151] Petrini Matteo. *Mixed signal generic testing in photonic integration*. PhD thesis, Politecnico di Milano, 2023.

[152] Dieter K. Schroder. Carrier lifetimes in silicon. *IEEE Transactions on Electron Devices*, 44:160–170, 1997.

[153] Cristina Rimoldi, Lorenzo L. Columbo, Jock Bovington, Sebastian Romero-García, and Mariangela Gioannini. Cw emission and self-pulsing in a iii-v/sin hybrid laser with narrow band mirror. *IEEE Photonics Journal*, 14(4):1–7, 2022.

[154] Cristina Rimoldi, Lorenzo Luigi Columbo, Jock Bovington, Sebastian Romero-García, and Mariangela Gioannini. Damping of relaxation oscillations, photon-photon resonance, and tolerance to external optical feedback of iii-v/sin hybrid lasers with a dispersive narrow band mirror. *Opt. Express*, 30(7):11090–11109, Mar 2022.

[155] Stefania Cucco, Marco Novarese, and Mariangela Gioannini. Design of si/poly-si microrings with complex waveguide cross-sections and minimal non-lineraties. *in preparation for IEEE J. Lightwave Tech.*, 2023.

[156] Ming Lyu and Claire Gmachl. Correction to the effective refractive index and the confinement factor in waveguide modeling for quantum cascade lasers. *OSA Continuum*, 4(8):2275–2283, Aug 2021.

Appendix A

Proof of equations

This chapter collects demonstrations of various equations introduced in the main text.

Circulating power in the ring

To obtain the power circulating in the ring, eq. (2.5), we consider that the total circulating field is the sum of all contributions associated to round trips in the ring, where the first term is related to the input field E_{in} in the add-drop MRR, $-\kappa \cdot (1-\eta^2)E_{in}$. Then all other terms are:

$$E_c(\omega) = -\kappa \cdot (1-\eta^2)E_{in}(1 + t^2 a e^{j\theta} + t^4 a^2 e^{2j\theta} + ...). \tag{A.1}$$

We note that $(1 + t^2 a e^{j\theta} + t^4 a^2 e^{2j\theta} + ...)$ is the geometric series of the fraction $\frac{1}{1-t^2 a e^{j\theta}} = \sum_{n=0}^{\infty} \left(t^2 a e^{j\theta}\right)^n$, therefore the circulating power is $P_c(\omega) = |E_c(\omega)|^2 = \frac{\kappa^2(1-\eta^2)}{|1-t^2 a|^2}$.

Optical confinement factor

We give here a proof of the optical confinement factor as defined in eq. (2.18) which follows what done in [118, 156].
The confinement factor is generally defined as:

$$\Gamma \equiv \frac{\alpha_m}{\alpha_b} \tag{A.2}$$

where α_m and α_b are the modal and material loss respectively.
Considering the electromagnetic field propagating in the waveguide, eq. (2.15), the propagation constant $\beta_\mu(\omega)$ is generally complex:

$$\beta_\mu = \beta_{\mu 0} + \Delta\beta \tag{A.3}$$

$\Delta\beta = k_0(\hat{n}_{eff,r} + j\hat{n}_{eff,i})$ is a perturbation of the propagation constant ($\hat{\beta}_{\mu 0}$). $\beta_{\mu 0}$ is the propagation constant of the waveguide with no loss and effective refractive index $n_{eff,0}$. k_0 is the field wavevector at angular frequency ω, and $\hat{n}_{eff,r}$ and $\hat{n}_{eff,i}$ the modal variation of the real and imaginary part of the effective index each. The loss of the guided mode is associated to the imaginary part as:

$$\alpha_m = -2Im(\Delta\beta) = -2k_0\hat{n}_{eff,i} \tag{A.4}$$

while the bulk material losses are

$$\alpha_b = -2k_0 n_{A,i} \tag{A.5}$$

with $n_{A,i}$ the imaginary part of the bulk refractive index variation which is assumed to be uniform over the waveguide cross section A. We can link equations A.4 and A.5 by writing the variation to the complex dielectric constant in the silicon material as:

$$\Delta\varepsilon_i = \varepsilon_0 \left[n_{si}^2 - (n_{Si} + j\alpha_b\lambda/4\pi)^2 \right] \tag{A.6}$$

which can be simplified since $n_{A,i}$ is considered to be small with respect to the refractive index:

$$\Delta\varepsilon_i \approx -2\varepsilon_0 n_{si}\alpha_b\lambda/4\pi \tag{A.7}$$

The variation of the imaginary part of the propagation constant of the guided mode is then obtained from coupled mode theory [140, 141]:

$$\Delta\beta_i = \frac{\omega \int\int_\infty \Delta\varepsilon_i \cdot E_\mu(x,y,\omega)^* E_\mu(x,y,\omega) dxdy}{2P_{n,\mu}} \tag{A.8}$$

By substituting eq. (A.7) in (A.8) and using (A.4) we get:

$$\alpha_m = 2\varepsilon_0 n_{si} \frac{\lambda}{4\pi} \frac{\omega \int\int_A \alpha_b \cdot E_\mu(x,y,\omega)^* E_\mu(x,y,\omega) dxdy}{2P_{n,\mu}} \tag{A.9}$$

where the integral has been limited over the waveguide area A since the material loss α_b is not defined outside of it. By using the equality $c = \frac{\lambda\omega}{2\pi}$ and eq. (2.17) we finally get:

$$\alpha_m = \alpha_b \frac{n_{Si} c \varepsilon_0 \int\int_A \left|E_\mu(x,y)\right|^2 dxdy}{\int\int_{A_{tot}} \Re e\left\{E_\mu(x,y) \times H_\mu(x,y)\right\} \cdot e_z dxdy}. \tag{A.10}$$

By comparing the previous equation with eq. (A.2), we obtain the expression for the optical confinement factor defined in eq. (2.18).

Optical losses due to TPA

The expression for TPA losses , eq. (3.4) is based on the work by Koos et al. in [117].

We consider the nonlinear Schrödinger equation for the field propagation $A_\mu(z,t)$ in the waveguide, where $P(z,t) = |A_\mu(z,t)|^2$ is the average power of the mode μ. In steady state ($\frac{\partial A_\mu(z,t)}{\partial t} = 0$), we have:

$$\frac{dA_\mu(z)}{dz} = -\gamma_i |A_\mu|^2 A_\mu \tag{A.11}$$

with γ_i the imaginary part of the nonlinear waveguide parameter in the waveguide defined as [117]:

$$\gamma_i = \frac{3\omega_0 \varepsilon_0 Z_0^2}{4 A_{eff} n_{si}^2} Im(\chi^3) \tag{A.12}$$

Z_0 is the free space impedance and χ^3 the complex scalar third-order nonlinear susceptibility. In order to compute the TPA coefficient, we multiply eq. (A.11) by A_μ^* and use the property $\frac{(\partial A_\mu \cdot A_\mu^*)}{\partial z} = A_\mu \cdot \frac{\partial A_\mu^*}{\partial z} + A_\mu^* \cdot \frac{\partial A_\mu}{\partial z}$ leading to:

$$\frac{dP(z)}{dz} = -2\gamma_i P \cdot P \tag{A.13}$$

which has a solution of the type $P(z) = e^{-\beta_{TPA} z}$ where the term $\beta_{TPA} = 2\gamma_i P$ is by definition the TPA coefficient. The latter is related to the imaginary part of χ^3 as [117]:

$$Im(\chi^3) = \frac{2n_{si}^2}{3k_0 Z_0}\beta_{TPA} \tag{A.14}$$

By substituting eq. (A.14) in (A.12) we finally get:

$$\alpha_{TPA} = 2\gamma_i P = \frac{\beta_{TPA}}{A_{eff}}P \tag{A.15}$$

where we used the identity $\frac{\omega_0 \varepsilon_0 Z_0}{k_0} = 1$.

Power absorbed and radiated in a MRR

In this section we give a demonstration of the power absorbed and radiated in a MRR, since these are fundamental in determining the self-heating due to linear and nonlinear losses. We first start with the power dissipated in the ring ($P_{d,MRR}$) and then separate the absorption contribution P_{abs} from the power radiated away from the ring due to bend loss $P_{rad,BL}$. Then we also include the power radiated by coupling losses $P_{rad,\eta}$, such that $P_{rad} = P_{rad,BL} + P_{rad,\eta}$.
The power dissipated in an add-drop MRR without considering coupling loss is:

$$P_{d,MRR} = -\int_0^{L/2} \alpha_{eff} P_c e^{-\alpha_{eff} z} dz + t^2 \int_{L/2}^{L} \alpha_{eff} P_c e^{-\alpha_{eff} z} dz \tag{A.16}$$

The first term takes into account the circulating power lost during propagation in the first half length of the ring before coupling with the drop port, while the second term consider the power not coupled outside the resonator (which is taken into account by the transmission coefficient t) lost in the second half of the ring. The minus sign indicates that this type of power is considered lost. Solving eq. (A.16) leads to

$$P_{d,MRR} = P_c(1-a) + P_c t^2 a(1-a) \tag{A.17}$$

Which is equal to $P_{d,MRR} = P_c(1-a)(1+t^2 a)$. To decouple the power lost due to absorption and bend losses we make use of the approximation:

$$(1-a) \approx (1-a_{abs}) + (1-a_{rad}) \tag{A.18}$$

where we remind $a_{abs} = e^{-(\alpha_0 + \Delta\alpha(P_c))\cdot L/2}$ and $a_{rad} = e^{-\alpha_{rad}\cdot L/2}$. This approximation holds when $1-a \approx 0$ which holds even for circulating power higher than those

achieved in this thesis as shown in figure A.1. Here we consider $R2$ since it has the

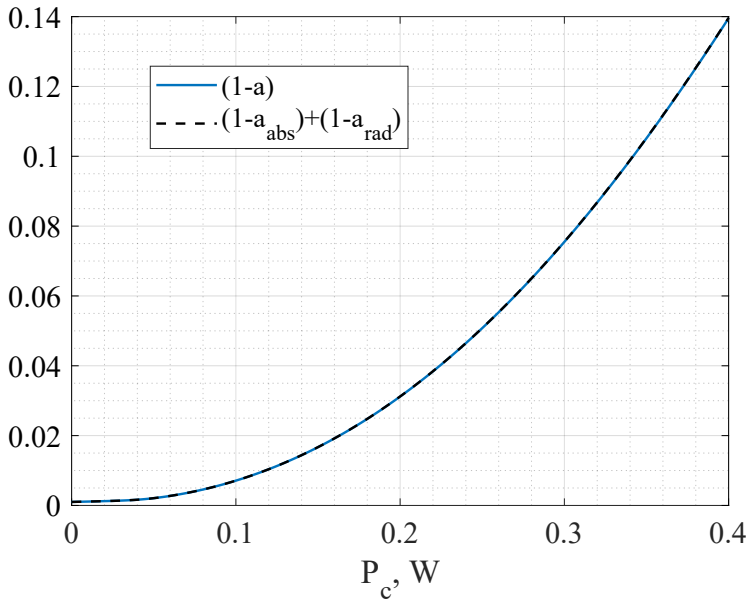

Fig. A.1 Proof of the approximation performed to separate the absorbed power causing self-heating from the one radiated due to bend losses as a function of the circulating power in the case of ring R2.

highest Q between all the analysed ring and therefore represent the worst case since $P_c \uparrow -> \alpha_{eff} \uparrow -> a \downarrow$.
The power absorbed in the ring is then

$$P_{abs} = P_c(1-a_{abs})(1+t^2a) \tag{A.19}$$

while the radiated due to bend losses:

$$P_{rad,BL} = P_c(1-a_{rad})(1+t^2a) \tag{A.20}$$

Lastly the power radiated due to coupling losses is composed of three contributions: first the power lost before coupling with the ring $\eta^2 P_{bus}$, then the power circulating in the ring lost at the drop port $\eta^2 P_c a$, and finally the power lost after one complete round trip $\eta^2 P_c a^2 t^2$. The total radiated power due to coupling loss is :

$$P_{rad,\eta} = \eta^2\left(\eta^2 \cdot (P_{in} + P_c \cdot (a + a^2 \cdot t^2))\right) \tag{A.21}$$

Summing equations (A.20) and (A.20) gives eq. (3.8).

Relation between $\Delta n_{eff,FCD}$ and $\Delta\lambda_{PP}$

In order to demonstrate eq. (4.1) we first write the round-trip condition of the propagating field inside the ring considering FCD caused by free carriers at resonance:

$$\frac{L}{c}\left(\omega_0(n_{eff,0}+\Delta n_{eff,FCD})+n_g(\omega_r-\omega_0)\right)=2\pi m \tag{A.22}$$

where ω_r is the new resonant frequency associated of the shifted NL spectrum and ω_0 the cold resonance of the ring.
Since the index m must be the same index of the cold resonance case, we can simplify the terms related to the cold resonance round trip condition, i.e., $\frac{L}{c}\left(\omega_0(n_{eff,0})\right)=2\pi m$, leading to

$$\omega_0(\Delta n_{eff,FCD})=-n_g(\omega_r-\omega_0) \tag{A.23}$$

which is written in terms of wavelengths as:

$$\Delta n_{eff,FCD}=-n_g(\frac{\lambda_0-\lambda_r}{\lambda_r}) \tag{A.24}$$

By defining $\Delta\lambda_r=\lambda_r-\lambda_0$ we have

$$\Delta n_{eff,FCD}=n_g(\frac{\Delta\lambda_r}{\lambda_r}) \tag{A.25}$$

We note that the quantity $(\frac{\Delta\lambda_r}{\lambda_r})$ is always much smaller than 1 since the maximum variation of resonant wavelength are on the order of $1-2\,ns$ (Si/poly-Si ring case). As a result we can write $\Delta n_{eff,FCD}=n_g(\frac{\Delta\lambda_r}{\lambda_0})$ which is exactly equal to eq. (4.1) introduced in the main text. We perform this approximation since λ_0 is well known during the experiment whereas a precise value for λ_r is difficult to retrieve due to the noise involved in the pump-probe experiment.

Appendix B

Propagation losses measurements on straight waveguides

Measurements of non-linear losses in silicon waveguides based on the same technology used for ring resonator $R2$ were provided by the foundry. These data were useful for our model as an additional validation tool and also to fix some important parameters such as β_{TPA}.
We considered two different waveguides widths W_{Si} equal to $450\,nm$ and $580\,nm$ with height $h_{Si} = 107\,nm$ and different total lengths L_{wg} as reported in table B.1.

Table B.1 Lengths of the straight waveguides analysed for NL power loss measurements.

W_{Si}, nm	$L_{wg}, \mu m$					
450 and 580	2895	3400	5240	7160	37700	52700

The propagation loss of the field in the waveguide was estimated as the ratio between the measured output P_{out} and input power P_{in}. Following the approach discussed in section 5.2 in the case of only one forward propagating field and a number of k slices, the power at each slice i is:

$$P(i) = P(i-1) \cdot e^{-\alpha_{eff}(i-1)dz}, \tag{B.1}$$

with $i = 2 : k+1$, $P(1) = P_{in}$, and $P(k+1) = P_{out}$. α_{eff} is dependent on z through the circulating power and carrier density, here we use eq. (3.2) with $\alpha_{rad} = 0$ since the waveguides are not bent. We can reproduce the experimental results with the

SRH model by using as fitting parameters η_{SCA}, β_{TPA} and the trap density in the waveguides $N_{450,f}$ and $N_{580,f}$. More precisely at each slice dz the power will generate an amount of free carriers es expressed in eq. (3.20). We assume the same trap density for waveguides with the same cross section, while the values for η_{SCA}, and β_{TPA} have been kept constant in both cases. Measurements and model results are displayed in figure B.1.

In both cases we have that $\beta_{TPA} = 1.5\,cm/GW$ and $\eta_{SCA} = 0.04$, whereas $N_{450,f} =$

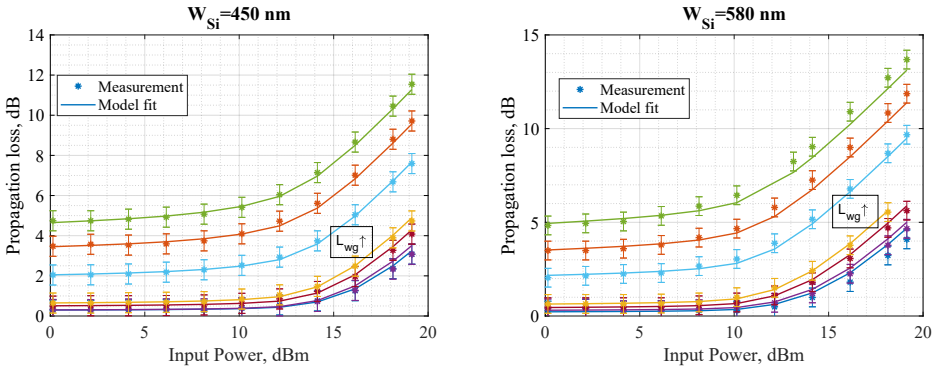

Fig. B.1 Propagation loss α_{eff} as a function of the input power in the waveguide for different waveguides lengths from blue ($L_{wg} = 2895\,\mu m$) to green ($L_{wg} = 52700\,\mu m$) when (a) $W_{Si} = 450\,nm$ and (b) $W_{Si} = 580\,nm$.

$3.4 \cdot 10^{16} cm^{-3}$ and $N_{580,f} = 1.9 \cdot 10^{16} cm^{-3}$. Lower values of the TPA coefficient would not make it possible to have such large losses in our waveguides for any physical sound values of trap densities. Comparing the two waveguides, it is interesting to see that, for the same input powers and L_{wg}, the larger waveguide, $W_{Si} = 580\,nm$, presents higher propagation losses. This is well explained by the fact that we have $N_{f,450} > N_{f,580}$, which results in higher free carrier lifetime for $W_{Si} = 580\,nm$ as shown in figure B.2. Here the SRH free carrier lifetime for different set of powers is plotted as a function of the waveguide length, i.e, calculated at each slice k of length dz. By looking at fig. B.2 (b) and (d) we note how the hole lifetimes are very similar, however τ_n is much larger in the smaller waveguide, see fig. B.2 (a), which is the cause for the higher propagation losses in the waveguide with $W_{Si} = 580\,nm$.

The values of β_{TPA} and η_{SCA} were fixed and used to characterise ring $R2$ in chapter 4. We also remark that the trap densities estimated in this section are of the same order of magnitude as those calculated for ring $R2$, which further validates our theory.

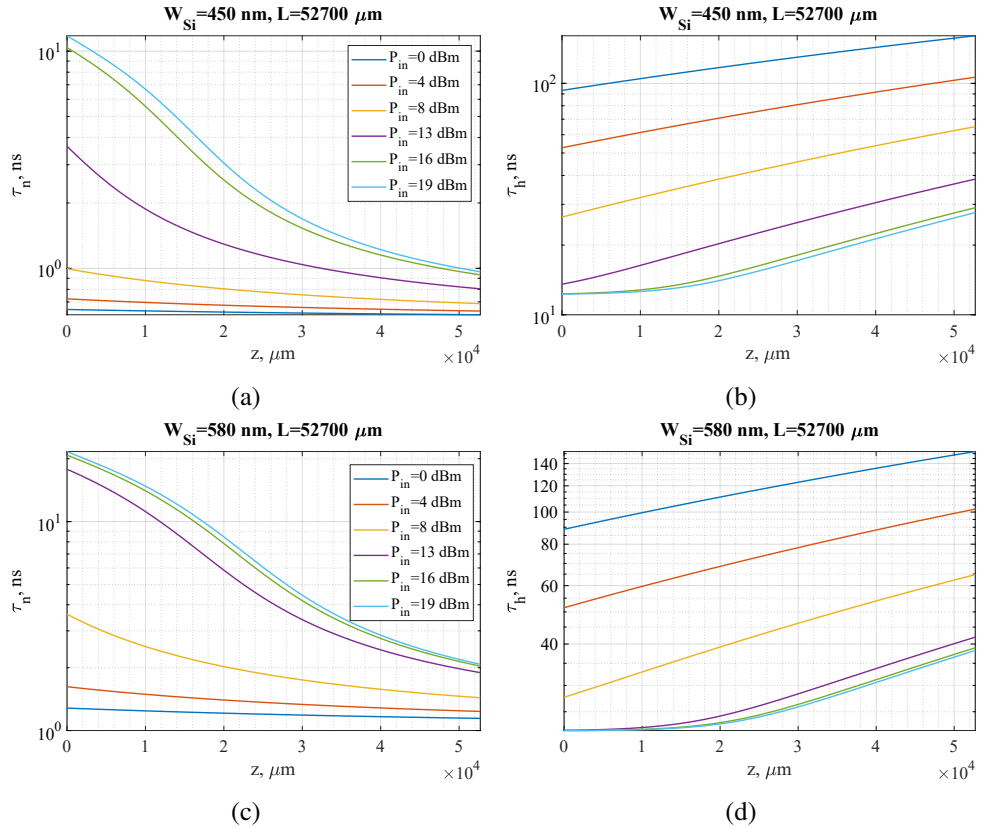

Fig. B.2 Free carriers lifetime in the waveguide with length $L_g = 52700\,\mu m$ as a function of the propagation distance in the waveguide for several input power for electrons (a) and holes (b) in the case of $W_{si} = 450\,nm$, (c) and (d) for $W_{si} = 580\,nm$. Legend colours of figures (b) and (d) are the same of (a) and (c).

Appendix C

FOMs for ring design of III-V/Si hybrid tunable laser

In this appendix we define the figure of Merits of the hybrid tunable laser mentioned in section 4.1 whose schematic is shown in figure 1.6. The laser consists in an active part (RSOA) that provides light into a passive mirror composed of waveguides and ring resonators that allow the laser output wavelength to be finely tuned by the Vernier effect through thermal control of the rings. The model for the design of this laser has been developed in [66]: the parameters of the RSOA are the same as in [66] whereas here we employ silicon instead of silicon nitride for the realization of the rings as summarised in table 5.1.

Ring radii

The determination of the two ring radii is the first step in the design. By fixing the radius of one ring to r_1 and the coupling coefficient of both rings to κ^2, the radius of the second ring r_2 must be selected in order to maximise the tuning range and minimize the overlap between the two non-aligned nearest adjacent resonances [66]. Assuming the resonant frequencies of the two rings to be aligned at the frequency f_0, we denote with f_1 and f_2 the distance, from f_0, of the nearest non-aligned resonances of ring1 and ring2 respectively, i.e., the FSR of ring1 and ring2. r_2 is then computed by imposing that the quantity $\Delta f_{1,2} = f_1 - f_2$ is C_f times larger then the full width

half maximum ($FWHM_{f1}$) of ring1 resonance:

$$\Delta f_{1,2} = C_f \cdot FWHM_{f1}. \tag{C.1}$$

Where $C_f = 2.5$ is in general enough to ensure a laser SMSR higher than $40dB$. r_2 is therefore a function of r_1, κ^2 and ring loss because it depends on the ring1 FWHM.

Tuning range

The maximum tuning range, which represents the maximum frequency range where we have again the maximum overlap of resonance frequencies of the two rings, Δf_{tune} originates in the Vernier effect and is equal to:

$$\Delta f_{tune} = \frac{f_2^2}{\Delta f_{1,2}} - f_2. \tag{C.2}$$

As a result the maximum thermal tuning (i.e., maximum temperature increase of the silicon waveguide core) requires to cover the ring free-spectral range f_2.

SMSR

For the calculation of the side mode suppression ratio, we must consider two possible competing longitudinal modes: the laser cavity longitudinal mode with frequency f_m closest to the lasing frequency f_0 (i.e., $f_m = f_0 + \Delta f_{FSR}$, with Δf_{FSR} the laser cavity free spectra range) and a laser cavity longitudinal mode with frequency f_{worst} corresponding to the peak of the overlap between the two resonances at $f1$ and $f2$. We calculate the SMSR for both cases and to be conservative we consider the worst scenario between the two. The SMSR is calculated as [141]:

$$SMSR = 1 + \Delta\alpha_m / \Delta g \tag{C.3}$$

where $\Delta\alpha_m$ is loss margin between the lasing mode and the competing longitudinal mode [141] and Δg is:

$$\Delta g = \beta_{sp}\eta_r \cdot \frac{\alpha_{SOA,i} + \alpha_{SOA,m}}{I_{bias}/I_{th} - 1}. \tag{C.4}$$

Table C.1 Parameters definition in the RSOA for the tunable laser design.

Parameter	Definition
β_{sp}	Spontaneous emission factor
η_r	Radiative efficiency
I_{bias}	bias current
I_{th}	threshold current
$v_{g,SOA}$	group velocity
$n_{g,SOA}$	group index
L_{SOA}	cavity length
τ_{SOA}	cavity round trip
V_{SOA}	active region volume
N_0	transparency carrier density
$\sigma_{SOA}\frac{\lvert E_{+,SOA}(t)\rvert^2}{V_{SOA}}$	Photon density
$\alpha_{H,SOA}$	linewidth enhancement factor
$\eta_{i,SOA}$	internal quantum efficiency
g_N	modal gain coefficient

here $\alpha_{SOA,i}$ is the internal loss in the SOA section and $\alpha_{SOA,m}$ the mirror effective loss provided by the foundry. The rest of the parameters are defined in Table C.1 and are the same as in [66].

Optical linewidth

Finally the optical laser linewidth is [66]:

$$\Delta\nu = \Delta g \frac{(1+\alpha_H)^2}{4\pi}\left(\frac{n_{g,SOA}\cdot L_{SOA}}{n_{g,SOA}\cdot L_{SOA}+n_{g,Si}\cdot L_{eff}}\right)^2. \tag{C.5}$$

α_H is the linewidth enhancement factor, L_{eff} the effective length of the entire passive mirror, and$n_{g,Si}$ the group index of silicon in the SiPh waveguides.

List of Figures

List of Tables

Acronyms

AR anti-reflection coating

ASE Amplified Spontaneous Emission

BCs boundary conditions

CWDM Coarse Wavelength Division Multiplexing

DFB distributed feedback laser

DWDM Dense Wavelength Division Multiplexing

EDFA Erbium Doped Fiber Amplifier

FCA Free Carrier Absorption

FDM finite difference method

FEM finite element method

FMCW frequency-modulated continuous-wave

FMM film mode matching method

LIDAR Light detection and ranging

LPCVD Low Pressure Chemical Vapour Deposition

MPW multi-project wafer

MRR microring resonator

MZI Mach-Zehnder Interferometer

NL non-linear

OPA optical phased arrays

PD photodetectors

PECVD Plasma Enhanced Chemical Vapour Deposition

PICs photonic integrated circuits

PML perfectly matched layers

PS phase control section

RSOA Reflective Semiconductor Optical Amplifier

SCA surface-charge-absorption

SFP Form-factor Pluggable

SGC surface grating coupler

SGCs Surface grating couplers

SiPh Silicon photonics

SISCAP silicon-insulator-silicon capacitor platform

SM single mode

SMSR side-mode-suppression-ratio

SOA semiconductor optical amplifier

SOI Silicon-on insulator

SPA single photon absorption

SPM self phase modulation

SRH Shockley-Read-Hall recombination

SSC spot size converter

TBC transparent boundary condition

TEC Thermo Electric Cooler

ToF time of flight

TPA Two Photon Absorption

WPE wall-plug efficiency

XPM cross-phase-modulation

XTPA cross two photon absorption